

MASTER OF SCIENCE THESIS

Comparison of Inflow Generation Methods for Large-Eddy Simulation

F.T. Pronk

June 25, 2012

FACULTY OF AEROSPACE ENGINEERING - DELFT UNIVERSITY OF TECHNOLOGY



Comparison of Inflow Generation Methods for Large-Eddy Simulation

MASTER OF SCIENCE THESIS

For obtaining the degree of Master of Science in Aerospace Engineering at Delft University of
Technology

FRANÇOIS THOMAS PRONK

June 25, 2012

Faculty of Aerospace Engineering · Delft University of Technology



Delft University of Technology

Copyright © François Thomas Pronk, TU Delft
All rights reserved.

DELFT UNIVERSITY OF TECHNOLOGY
DEPARTMENT OF AERODYNAMICS

The undersigned hereby certify that they have read and recommend to the Faculty of Aerospace Engineering for acceptance the thesis entitled **Comparison of Inflow Generation Methods for Large-Eddy Simulation** by **François Thomas Pronk** in fulfillment of the requirements for the degree of **Master of Science**.

Dated: June 25, 2012

Department Head:

prof. dr. ir. drs. H. Bijl

Supervisor:

dr. S.J. Hulshoff

Reader:

dr. A.H. van Zuijlen

Reader:

I. Popov, MSc

Bonne Lecture Maman !

Acknowledgments

As my thesis comes to an end, I would like to acknowledge all the people that have helped me reach my goal of finishing my aerodynamics master to become an engineer.

First of all, I would like to thank my family, my friends and my colleagues for their support, for the good times they gave me during my study, and for everything I learnt from them.

Secondly, I would like to thank my supervisor Steven Hulshoff for his enthusiasm, his dedication, his patience, and for everything he has brought me, taught me and helped me with since I first met him, during my Bachelor end project.

And last but not least, I would really like to thank Sylvia Wortmann and Coen Koning for their care, their advice and their unconditional support in difficult and in good times.

To all, thank you for helping me discover what I am today.

Summary

There is an ever growing industrial demand for the numerical simulation of complex industrial flow problems. Although historically Reynolds-Averaged Navier-Stokes (RANS) methods have been widely used for such applications, there are many flow cases for which RANS simulations are unsuitable. These include studies of the effects of flow control devices on turbulent boundary layers, as researchers are interested in how such devices interfere with the structure of the turbulence. To solve such flow problems, Large-Eddy Simulations (LES) can be used. In the current study, the focus was put on providing an objective comparison of inflow modeling techniques applicable to the simulation of flow control devices in a coarse LES framework, with a special interest in general techniques applicable to a large range of flows.

Five different type of inflow conditions were implemented in OpenFOAM and applied to the computation of a zero pressure-gradient turbulent boundary layer. The recycling and rescaling method by Lund, Wu, and Squires (1998) was shown in previous publications to work well in LES computations, and was therefore chosen as baseline solution to which the other models could be compared. Similarly, the simplified recycling method by Spalart, Strelets, and Travin (2006) was previously shown to work well in the context of Direct Numerical Simulations (DNS), and was evaluated together with the method by Lund et al. Both inflows were compared to the highest quality low Reynolds-number DNS data available.

However, as the recycling type inflows are known to be limited in application, inflows which can be used in the simulation of more general flows were also investigated. The first of these was a precursor-like method, implemented by recycling and rescaling channel-flow data using the method by Lund et al. A random inflow was also implemented, and was tuned to match required Reynolds stresses. As random inflows are known to suffer from long adaptation lengths, an extra random inflow with a forcing method by Spille-Kohoff and Kaltenbach (2001) was tested, to assess whether it could palliate to the deficiencies of the random type inflows.

After verifying the quality of the baseline recycling inflow, all the inflows were compared through an evaluation of their shape-factor and skin-friction evolution as a function of Re_θ .

The recycling type of inflow by Lund et al. (1998) and by Spalart et al. (2006) demonstrated

adaptation lengths of $x/\delta_0 = 18$ and $x/\delta_0 = 22$ respectively.

The more general precursor-like method also showed very promising results, with an adaptation length of $x/\delta_0 = 18$, although it slightly underpredicted the shape factor evolution, and overpredicted the skin friction evolution.

The random inflow without forcing planes was found to be uncompetitive. Its shape factor and skin friction evolution could not adapt to that of DNS within the current domain size tested.

Finally, the random inflow method with forcing planes was also shown to give good results, with a slightly longer adaptation length of $x/\delta_0 = 30$. After adaptation, it showed a skin friction evolution similar to the baseline results, albeit slightly underpredicted. The low cost and flexibility of this method make it an interesting candidate for future developments.

Contents

Preface	vii
Summary	ix
1 Introduction	1
1.1 Reference Data for the Flat Plate Turbulent Boundary Layer	2
1.2 A Short History of Artificial Boundary Conditions	2
1.3 Thesis Outline	3
2 Turbulence Theory and Numerical Simulation Technique	5
2.1 A Short Introduction to Turbulent Flow Theory	5
2.1.1 Different Scales in Turbulent Flows	5
2.1.2 Wall-Bounded Flows	8
2.2 The Navier-Stokes Equations	10
2.2.1 General Set of Equations	11
2.2.2 The Incompressible Flow Simplification	11
2.3 General Overview Of Modeling Techniques	12
2.3.1 RANS	12
2.3.2 DNS	14
2.3.3 LES	15
2.4 Large Eddy Simulation	16
2.4.1 Governing Equations	16
2.4.2 Subgrid-Scale Models	18
3 Evaluation of Flat Plate Reference Results	23
3.1 General Turbulent Flat Plate Discrepancies	23
3.2 Comparing DNS Data From Schlatter and Örlü (2010) and Simens et al. (2009) .	24

4	Inflow Boundary Condition Treatment and Flow Control	29
4.1	Generation of Turbulent Inflow Data for Spatially Developing Boundary Layers	29
4.2	Recycling and Rescaling Methods	31
4.2.1	The Recycling and Rescaling Method by Lund, Wu, and Squires (1998)	31
4.2.2	The Recycling and Rescaling Method by Spalart, Strelets, and Travin (2006)	33
4.2.3	A Small Note on Applying Recycling Methods to LES	33
4.3	Precursor Method	34
4.4	Random Inflow	35
4.5	Controlled Forcing Method by Spille-Kohoff and Kaltenbach (2001)	36
5	Baseline Results and Their Sensitivity	37
5.1	Comparison Procedure and Numerical Setup	37
5.1.1	Comparison Procedure and Parameters	37
5.1.2	Computational Procedure	38
5.2	A Detailed Analysis of the Results Obtained Using the Inflow by Lund et al. (1998)	39
5.3	Pressure Gradient and Outer Mean-Velocities	42
5.4	Revisiting Means and Reynolds Stresses	44
5.5	Adaptation Lengths	47
5.6	A Summary of the Sensitivity of the Results to the Domain and Grid	48
5.7	Placement of the Recycling Plane	53
5.8	On The Need Of Determining The Correlation Length	54
6	Inflow Generation Comparison	55
6.1	Inflow Comparison and Numerical Setup	55
6.2	Results	56
6.2.1	Turbulence Evolution	58
6.2.2	Practical Remarks on the Forcing Method by Spille-Kohoff and Kaltenbach (2001)	61
6.2.3	Comparison Conclusions	62
7	Conclusions and Recommendations	63
7.1	Conclusions	63
7.2	Recommendations	64
	Bibliography	65
8	OpenFOAM Settings	69
8.1	Domain Used	69
8.2	Numerical Setup	69
8.3	Validation	70

CHAPTER 1

Introduction

Stimulated by an insatiable demand from the industry to solve complex industrial problems, there is a large interest for the application of Computational Fluid Dynamics (CFD) to high Reynolds number external flows. Although Reynolds-Averaged Navier-Stokes (RANS) methods are widely used for this purpose, these require models for the effects of turbulence on the mean flow. There exists several important flow classes for which it is difficult to develop adequate RANS models, including those with separation from a smooth surface, or those with boundary-layer control devices. The alternative is to compute rather than model the turbulence dynamics. One approach, known as Direct Numerical Simulation (DNS), is to resolve turbulence dynamics at all length scales. Due to the vast range of scales in high-Reynolds-number flows, however, the cost of such simulations prohibitive. A more feasible alternative is Large-Eddy Simulation (LES), where only the largest scales of turbulence are resolved. However, even with current computational capacities, LES can only be applied to restricted parts of a typical problem domain, in which the range of relevant length scales is sufficiently limited.

The reduction of domain size to the snugest fit possible around the solution of interest imposes stringent requirements on the artificial boundary conditions applied to the outer-limits of numerical domains, to ensure the flow within the domain behaves as its physical, unbounded, counterpart. Properly assessing the performance of artificial boundary conditions is therefore of great importance, and calls for rigorous testing using a representative flow case. Ideally, such a reference test case should also be analogous to the problems which will be simulated with the artificial boundary conditions in question. In the context of external flows with boundary layer development, the canonical zero pressure-gradient turbulent flat plate flow is a suitable case for this purpose, due to its sensitivity to the quality of the turbulent information within the boundary layer.

1.1 Reference Data for the Flat Plate Turbulent Boundary Layer

Although there exists several sets of experimental results for low Reynolds-number flat plate boundary flows, researchers have found these to be difficult to use as reference solutions. For example, Schlatter and Örlü (2010) found that most experimental low Reynolds number flat plate measurements were not supplemented by direct and independent skin-friction measurements, as well as often not complying to zero pressure-gradient equilibrium conditions. This has a direct effect on the usability of the experimental results, as the scaling relations derived from such data are not accurate.

The lack of fully established reference data for low Reynolds-number flat plate experiments led Schlatter and Örlü to investigate whether similar disparities could be found in recent Direct Numerical Simulation (DNS) data. By comparing six DNS computations made after 2002, the authors discovered that the simulation of the same canonical flat plate flow also gave surprisingly inconsistent results, even for such basic quantities as shape factor, friction coefficient and fluctuation maximum. As all the simulations compared in the study were obtained using reliable computational methods at high enough resolutions, Schlatter and Örlü concluded that the discrepancies could not solely be attributed to poor numerics. Instead, they postulated that such differences came from different choices in numerical domain, such as domain dimension, settling length, and artificial boundary conditions.

1.2 A Short History of Artificial Boundary Conditions

Practical numerical simulation of realistic flows often requires that artificial computational boundaries be imposed between the flow region of interest and the part of the flow which one would like to avoid computing. This application of artificial boundary conditions should ideally be done without influencing the solution within the computational domain. Within the field of turbulent numerical simulations, both the inflow and outflow boundary conditions are of high importance. The current study focuses on the modeling of artificial turbulent inflow conditions for numerical simulations. Discussing artificial outflow boundary conditions is beyond the scope of this work. The interested reader can refer to an extensive review by Colonius (2004) for more information.

Early approaches to turbulent inflow modeling used random velocity fluctuations imposed on a mean flow. As original attempts supplying white noise as velocity fluctuation were unsuccessful, researchers tried to improve on the random inflow method by developing stochastic models using correlation information provided by experimental results. For instance, Lee et al. (1992) used velocity perturbations with prescribed power spectrum and random phase, and claimed an adaptation length of $12 \delta_0$ before the flow could be considered realistic. While attempting to include isotropy information using Fourier-modes based on random phase and amplitude, Batten et al. (2004) reported needing at least $20 \delta_0$ before obtaining a physically realistic flow. More successfully, Pamiès et al. (2009) showed that channel flow mean and Reynolds-stress profiles could be matched accurately by superimposing analytical hairpin-like vortical structures on a mean profile, resulting in adaptations lengths of $6 \delta_0$.

Another approach to the generation of inflow condition for turbulent numerical simulations makes use of secondary simulations or precursor databases to provide turbulent information to a primary computation, circumventing the problem of inflow condition by using an equilibrium flow computed using periodic boundary conditions. Such an approach was applied by Schlüter et al. (2004) for hybrid RANS/LES computations, and showed good agreement with experimental results.

A third type of inflow modeling strategy is characterized by the recycling type of inflows pioneered by Spalart and Leonard (1985). These rely on turbulent information obtained from the outflow of the computational domain to provide the inflow condition, using a coordinate transform to account for boundary layer growth. The quality of the results by Spalart and Leonard later inspired Lund et al. (1998) to develop a similar recycling method, while circumventing the need for an unwieldy coordinate transformation by extracting and rescaling a velocity field from within the computational domain. They achieved an adaptation length of $8\delta_0$. Further simplifying the approach by Lund et al., Spalart et al. (2006) managed to decrease the adaptation length to $4\delta_0$.

The recycling type of inflow by Lund et al. (1998) is currently accepted as being the most accurate turbulent inflow condition for developing boundary layer simulations. However, the scope of application of such inflows is limited by the equilibrium turbulent flow conditions assumed when choosing the scaling laws for the rescaling procedures. Moreover, they also implicitly require that the flow state and boundary conditions does not change between the inflow condition and the recycling plane, to ensure the turbulence evolution at both location is similar. And finally, they impose that the position of the recycling plane should be chosen carefully to avoid coherence problems.

Such limitations are not present when using precursor or random inflow conditions as their definition does not rely nor depend on downstream information, making them attractive when considering inflow conditions for more general types of flows.

1.3 Thesis Outline

The goal of the current master thesis is to make an objective comparison of recent inflow modeling techniques applicable to the simulation of flow control devices in turbulent wall-bounded flows. Due to the ubiquitous nature of computational resources restrictions, the inflows will be evaluated in the context of coarse, Large-Eddy Simulations.

The recycling and rescaling method of Lund et al. (1998) will be chosen as reference inflow model, as it was shown in previous publications to work well in LES computations, and will be tested together with the similar recycling and rescaling method by Spalart et al. which was developed for DNS computations.

It will also be investigated whether more general type of inflow conditions could deliver performance comparable to that of recycling methods. To this end, a precursor method will be tested, and a flow correction method developed by Spille-Kohoff and Kaltenbach (2001) will be applied to a random inflow method, to assess whether it is accurate enough to remedy to the long adaptation lengths normally associated with random inflow conditions.

In the interest of compactness, the baseline results obtained with the two recycling procedures will be considered first. Then, the comparison will be made with the more general precursor and random inflow methods, to see how they compare to recycling methods.

The canonical zero pressure-gradient turbulent flat plate flow was chosen as a test case and the highest quality existing low Reynolds-number DNS data is used as a reference solution.

To allow a more straightforward comparison between the different inflow methods, two specific parameters will be considered. First of all, the evolution of the shape factor H as a function of Reynolds number Re_θ will be used. The shape factor, defined as the displacement thickness δ^* divided by the momentum thickness θ , allows comparison of two integral properties of a turbulent flow which do not depend on estimates of skin friction, which can be subject to significant numerical errors in the contexts of LES. The shape factor was furthermore shown to be a sensitive indicator of the quality of the boundary layer. Then the evolution of the skin friction coefficient

will be considered independently, as it allows the indirect monitoring of the local level of turbulent activity within the boundary layer.

Using the shape factor and skin friction coefficient evolution, the adaptation length of the various inflows will be estimated. In this study, the adaptation length will be defined as the domain length needed before the shape factor and skin friction coefficient follow a streamwise evolution similar to that of the DNS results. The longest of the two lengths will then be defined as the adaptation length.

As a word of caution, it should be mentioned that a close comparison of the DNS data by Schlatter and Örlü and that by Simens et al. (2009) revealed intriguing differences between the two sets of data, which both groups of authors recognize as being caused by the different strategies chosen when applying numerical boundary conditions. This will be described in more detail in chapter 3.

Turbulence Theory and Numerical Simulation Technique

The following chapter will give a succinct introduction to turbulent flow theory, in an attempt to make this master thesis more self-contained. As it is only meant as an introduction to the theory relevant to the current study, readers familiar with the theory of turbulent wall-bounded flows and with the implementation of LES can skip this chapter and proceed to the next.

In the following, the notion of turbulent scales will be presented first, a concept useful to understand the rationale behind Large-Eddy Simulation, followed by a subsection describing the specificity of wall-bounded turbulent flows. The focus will then shift towards the application of the Navier-Stokes equations to the numerical simulation of turbulent flows, including a short review of the most common computational techniques used at the time of writing, together with a more in-depth description of the simulation strategy which will be used for the current study.

2.1 A Short Introduction to Turbulent Flow Theory

2.1.1 Different Scales in Turbulent Flows

Well over 100 years after the first true statistical analysis of turbulence by Osborne Reynolds, turbulence is still an outstanding problem of fluid dynamics, with no analytical solutions of turbulent flows available in geometries of interest to engineering applications. Due to the complexity of turbulent flows, much of the knowledge on the flow characteristics have been derived experimentally, to be completed only recently by more detailed numerical solutions thanks to advances in computational hardware. Nonetheless, both experimental and numerical approaches generally use the Navier-Stokes equations (NSE) as starting point to study the characteristics of turbulent flows. The Newtonian fluid assumption and the continuum assumption used when deriving the Navier-Stokes equations might be violated locally due to very high velocity gradients

but comparison between numerical and experimental data showed the variations observed when omitting these effects to be negligible, making the NSE a proper analytical tool for turbulent flow analysis.

A key word often encountered in the description of turbulent flows is the term “eddy”. As defined by Davidson (2004), an eddy can be seen as a “blob” of vorticity and its associated velocity field, or put more simply, a patch of air moving in a circular manner.

The first modern view on turbulence scales was officially formulated by the meteorologist and mathematician Lewis Fry Richardson. Through observation Richardson noticed that velocity fields displayed a broad spectrum of eddy sizes, and that the dissipation of the flow energy was mainly associated with the smallest eddies. These observations led Richardson to introduce the concept of *energy cascade*, describing a plausible energy transfer mechanism from the largest eddies to the smallest structures. His theory was that the largest eddies in the flow were created by instabilities in the mean flow, which were themselves also subjected to instabilities, leading to a rapid break-down of the large eddies into smaller vortices. The smaller eddies would themselves also be sensitive to instabilities and would break-down into smaller structures, and the process would continue until the smallest structure size would be reached, at which point the smallest vortices would dissipate their energy. Using the eddy size Reynolds number defined by

$$\text{Re}_l = \frac{ul}{\nu}, \quad (2.1)$$

with l the eddy diameter, u the value of the fluctuation velocity and ν the kinematic viscosity, Richardson explained that viscosity played no part in the energy cascade. Indeed, for large Re the viscous stresses acting on the eddies are negligible and the whole cascade process is therefore driven mainly by inertia forces. On the other hand, when the Reynolds number based on the eddy size is of order unity, the cascade process comes to a halt as the viscous forces are no longer negligible and dissipation becomes dominant.

Based on Richardson’s concept, the Russian scientist Kolmogorov published two papers (Kolmogorov, 1941a,b) which had a profound impact on the way the energy spectrum in turbulence is understood and modelled. He postulated that at sufficiently high Reynolds number the directional biases of the larger eddies was lost in the chaotic scale-reduction process linked to the energy cascade and that the small-scale turbulent motions were therefore statistically isotropic. Kolmogorov further argued that in the same way the directional information of the largest structures was lost through the energy cascade, so was the information about the geometry of the large eddies, implying that all the information and influence stemming from the boundary conditions and the mean flow field was similarly lost in the process. An important consequence of this hypothesis is that the statistical and structural properties of the small dissipation scales have in a sense a universal form, and will be similar in all high Reynolds number flows. The behaviour of the smallest scales can therefore be considered as only being determined by the energy fed to them via the energy cascade, and by the effects of viscosity. From there, Kolmogorov formulated his first similarity hypothesis stating that the statistics of the small-scale motions were uniquely determined by a combination of the kinematic viscosity ν and the dissipation rate ϵ . He proposed the following relationship for the smallest relevant length scales η present in a turbulent flow

$$\eta = \left(\frac{\nu^3}{\epsilon} \right)^{\frac{1}{4}}. \quad (2.2)$$

Similarly, Kolmogorov proposed a velocity and a time scale for the smallest structures of the flow, defined respectively as

$$v = (\nu\epsilon)^{\frac{1}{4}}, \quad (2.3)$$

and

$$\tau = \left(\frac{\nu}{\epsilon}\right)^{\frac{1}{2}}. \tag{2.4}$$

A detailed description of the method used to find these results can be found in Kolmogorov (1941b). For a more tractable approach based on dimensional analysis, references as Bernard and Wallace (2002) or Davidson (2004) can be consulted.

Using the first similarity hypothesis as basis, Kolmogorov went on to formulate a second similarity hypothesis by suggesting the existence of an intermediate range of scales with dynamics independent of both the large-scale turbulence-producing eddies and the small dissipation scales. These intermediate scales transferring the energy received from the large scales down the cascade to the smallest scales, would, according to Kolmogorov, only depend on the dissipation rate ϵ of the flow and the wave number κ of the eddies, and not on viscosity. He therefore names this intermediate range the “inertial range”. Kolmogorov further argued that this range had an important influence on the energy spectrum function $E(\kappa)$, and proposed the following relationship for the energy spectrum in the inertial range

$$E(\kappa) = C_k \kappa^{-\frac{5}{3}} \epsilon^{\frac{2}{3}}, \tag{2.5}$$

where C_k is the Kolmogorov constant and is found to have a value of approximately 1.4. A qualitative plot of the three scale regions and their corresponding energy spectrum can be found in figure 2.1.

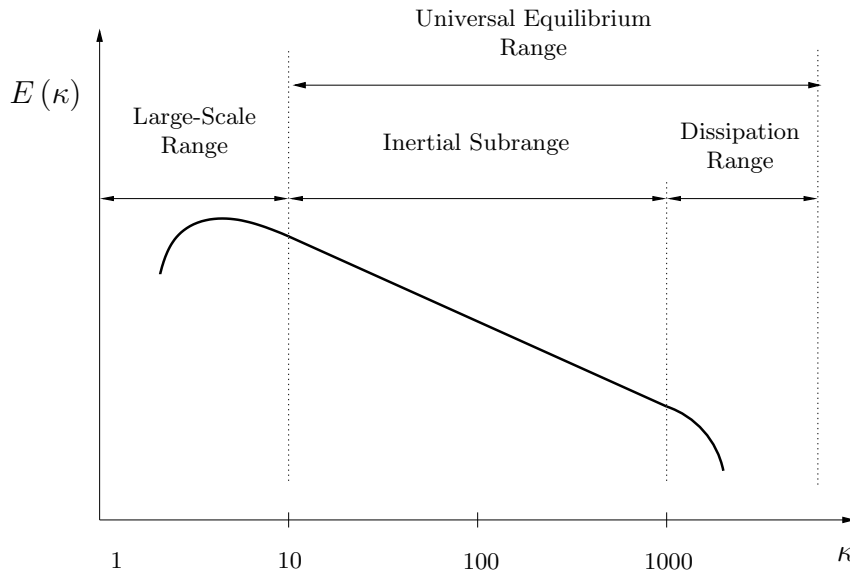


Figure 2.1: Qualitative Energy Spectrum of a Turbulent Flow

Despite the fact that some of the underlying assumptions made by Richardson and Kolmogorov have been proved to be at least partially incorrect, their conclusions are still very useful conceptually. However, due to these flawed assumptions it should be kept in mind that the concepts presented here-above remain an idealisation of the true behaviour of turbulent flows. As an example, it has been proved in recent years that the energy transfer between scales happens genuinely in two directions, instead of in the unidirectional fashion proposed by the cascade theory. It has

also been shown that the energy isn't necessarily transmitted homogeneously to all the length scales through the energy cascade, but that large eddies could for instance transmit their energy directly to much smaller structures in the flow. Nonetheless, Kolmogorov's description still predicts the correct order of turbulent scales present in turbulent flows, as well as the correct energy associated with these wavelengths. Similarly, the concept of Reynolds number independence, although known to be partially incorrect, allows researchers to analyse low Reynolds number flows and make behaviour predictions for higher Reynolds number situations.

For a more in-depth description of Kolmogorov's hypotheses, their applications and limitations, the interested reader is referred to the accessible description by Pope (2000, Chapter 6).

2.1.2 Wall-Bounded Flows

After this introduction to general turbulent flows, the focus will be shifted to wall-bounded flows. Although the isotropy condition no longer hold for true wall-bounded turbulence, even in the smaller scales, the concepts developed in the previous section are still very relevant to make the analysis of these flows possible.

Boundary Layer Subdivision

When comparing boundary-layer velocity profiles in y/δ coordinates, the differences between various types of flows are striking, with each flow displaying distinctive and highly non-linear profiles, making a comparison between them improbable at first sight. However, the physical insight from Ludwig Prandtl (1933) and Theodore von Kármán (1930) permitted the subdivision of boundary layers in general regions, making a universal non-dimensional analysis possible. Through their analysis they deduced that general turbulent boundary layer profiles could be subdivided in an inner and an outer layer, with an intermediate overlap region between the two.

The inner layer is a region where the flow dynamics are dominated by viscous shear and where the rate of turbulent energy production exceeds dissipation. This leads to part of this energy being exported towards the higher layers of the flow. The part of the inner layer outside the overlap layer, commonly called the viscous wall region, can be further subdivided into two parts: the viscous sublayer, closest to the surface, and the buffer layer.

In the outer layer the turbulent shear or eddy shear dominates. This is a region where dissipation exceeds production and turbulence is partly maintained by the energy transported from the inner layer.

The overlap region, a region of overlap between the inner and the outer layer, can be seen as a region of constant stress where dissipation equals production, and where both viscous and inertial effects co-exist.

The relation between these different regions is illustrated in figure 2.2.

Wall Coordinates

The universal region subdivision by Prandtl and von Kármán allowed researchers to pinpoint the parameters describing localized flow conditions, paving the way for a non-dimensional analysis of boundary layer flows and permitting comparison between very different types of flows. The key to obtaining dimensionless velocity profiles was to express flow properties in terms of wall coordinates. When looking at boundary-layer velocity profiles it is common to use the y coordinate normalized with the local boundary-layer thickness δ as spatial reference. However, this does not show explicitly the similarity between various flows. By defining new non-dimensional

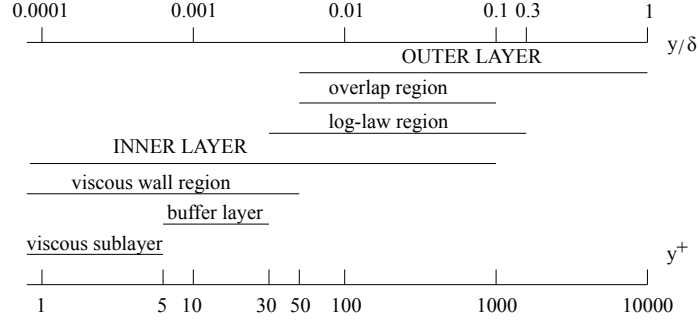


Figure 2.2: Sketch Showing the Various Wall Regions and Layers Defined in Terms of the Wall Coordinate y^+ and in Terms of y/δ . (From Pope, 2000)

parameters based on local flow properties a switch can be made to a so-called wall coordinate system.

First a local viscous time scale is defined as

$$t_\nu = \left(\frac{\partial \bar{u}}{\partial y} \Big|_{y=0} \right)^{-1}, \quad (2.6)$$

where \bar{u} is the mean streamwise velocity, and y is the coordinate measured perpendicular to the wall. Very close to the wall, where the Reynolds stresses are negligible, the wall shear stress is dominated by viscous contributions. From Pope (2000, p 269) the wall shear stress can then be written as

$$\tau_w \equiv \mu \left(\frac{d\bar{u}}{dy} \right)_{y=0}, \quad (2.7)$$

which, after substitution in equation (2.6), yields the following expression

$$t_\nu = \frac{\mu}{\tau_w}. \quad (2.8)$$

In a similar fashion a viscous length scale can be defined as

$$l_\nu = \sqrt{\nu t_\nu}, \quad (2.9)$$

allowing the computation of the wall-friction velocity as

$$\begin{aligned} u_\tau &= \frac{l_\nu}{t_\nu} = \sqrt{\frac{\tau_w}{\rho}} \\ \Leftrightarrow u_\tau &= \sqrt{\nu \frac{d\bar{u}}{dy} \Big|_{y=0}}. \end{aligned} \quad (2.10)$$

From there, the reference quantities can easily be expressed in terms of wall units, also referred to in literature as viscous lengths. The new distance from the wall measured in wall units is defined by

$$y^+ = \frac{y}{l_\nu} = \frac{y u_\tau}{\nu}, \quad (2.11)$$

and the u - velocity can be expressed as

$$u^+ = \frac{u}{u_\tau}. \quad (2.12)$$

Boundary Layer Description in Wall Coordinates

Using the newly defined coefficients, a better analysis of the dynamics of the boundary layer can be made. Through measurements, scientists have found that in the viscous sublayer and for $y^+ \leq 5$, the velocity profile is linear, that is to say

$$u^+ = y^+. \quad (2.13)$$

Experimental results have also shown that for high enough Reynolds numbers, there is a region of flow in the boundary layer where it can be supposed that viscosity has little effect, and boundary layers tend to follow a universal law. This law was first postulated by von Kármán in 1930, and is referred to as the logarithmic law of the wall, or simply, the log-law. It is defined as

$$u^+ = \frac{1}{\kappa} \ln y^+ + B, \quad (2.14)$$

where κ and B are constants. Common values for the von Kármán constant are $\kappa \approx 0.41$ whereas the range for B varies from 5 to 5.5. Patel and Head (1969) determined that a necessary condition to obtain a region where the coefficients of the log-law were universal constants, was to have $Re_l > 3000$. Extra information on the derivation of the logarithmic law can be found in Pope (2000, chap 7).

Finding a simple description for the smooth transition from the viscous sublayer to the log-law is a little less straightforward. White (2006) mentions the formula deduced by Spalding (1961) covering the entire wall-related region, and given by

$$y^+ = u^+ + e^{-\kappa B} \left[e^{\kappa u^+} - 1 - \kappa u^+ - \frac{(\kappa u^+)^2}{2} - \frac{(\kappa u^+)^3}{6} \right]. \quad (2.15)$$

For the region of the outer layer outside of the log-law range, White (2006) suggests using Coles' law given by

$$u^+ \approx \frac{1}{\kappa} \ln(y^+) + B + \frac{2\Pi}{\kappa} f\left(\frac{y}{\delta}\right), \quad (2.16)$$

where Π is Coles' wake parameter, and f is the wake function normalized to be zero at the wall, and unity at $y = \delta$. For more information, the reader is referred to White (2006, chap 6).

As a closing remark, it should be mentioned that the validity of describing the overlap region using the logarithmic law of the wall presented here above is still subject to debate. And, while the main argument of the log law antagonists is the non-universality of the "constants" κ and B used in equation (2.14), they propose to describe the overlap region using a power law instead. Nonetheless, although the debate might of importance for the proper quantification of fundamental turbulent relations, both the power-law and the log-law are of sufficient accuracy for engineering purposes.

2.2 The Navier-Stokes Equations

The following section will briefly describe the Navier-Stokes equations which will be used to compute the turbulent flow under consideration, as well as the incompressible flow simplification brought to the original set of equations.

2.2.1 General Set of Equations

The governing equations describing the motion of a fluid in space and time are a coupled set of non-linear partial differential equations referred to as the Navier-Stokes Equations (NSE). These equations are often derived by considering a given quantity of matter and its properties, such as mass, momentum or energy, inside a given control volume. From there, a set of integral equations can be derived, describing the general properties of the system under consideration, such as conservation of mass, momentum and energy. Applying Gauss' theorem to the set of equations obtained and assuming the control volume to be infinitesimally small then leads to the following set of coordinate-free differential equations, where the energy equation has been neglected

$$\frac{\partial \rho}{\partial t} + \operatorname{div}(\rho \mathbf{u}) = 0, \quad (2.17)$$

$$\frac{\partial(\rho \mathbf{u})}{\partial t} + \operatorname{div}(\rho \mathbf{u} \mathbf{u}) = \sum \mathbf{f}. \quad (2.18)$$

These equations are referred to as the continuity and momentum equation, respectively. For Newtonian fluids, where a linear relation exists between velocity gradient and shear stress, and neglecting gravity forces, the momentum equation can be written as

$$\frac{\partial(\rho \mathbf{u})}{\partial t} + \operatorname{div}(\rho \mathbf{u} \mathbf{u}) = \operatorname{div} \mathbf{T}, \quad (2.19)$$

where the stress tensor \mathbf{T} is defined as

$$\mathbf{T} = - \left(p + \frac{2}{3} \mu \operatorname{div} \mathbf{u} \right) \mathbf{I} + 2\mu \mathbf{D}, \quad (2.20)$$

with

$$\mathbf{D} = \frac{1}{2} \left[\operatorname{grad} \mathbf{u} + (\operatorname{grad} \mathbf{u})^T \right]. \quad (2.21)$$

Introducing the Del operator these equations can be re-written as

$$\frac{\partial \rho}{\partial t} + \nabla \cdot (\rho \mathbf{u}) = 0, \quad (2.22)$$

$$\frac{\partial(\rho \mathbf{u})}{\partial t} + \nabla \cdot (\rho \mathbf{u} \mathbf{u}) = \nabla \cdot \mathbf{T}, \quad (2.23)$$

with the stress tensor written as

$$\mathbf{T} = - \left(p + \frac{2}{3} \mu \nabla \cdot \mathbf{u} \right) \mathbf{I} + \mu (\nabla \mathbf{u} + \nabla \mathbf{u}^T). \quad (2.24)$$

For more information on the derivation of the Navier-Stokes equations, one can refer to standard literature such as Bernard and Wallace (2002), Ferziger and Perić (2002), or Pope (2000).

2.2.2 The Incompressible Flow Simplification

The conservative equations (2.22) and (2.23) are the most general form of the Navier-Stokes equation and assume that all fluid and flow properties change in space and time. For flow velocities under 0.3 times the speed of sound, these equations can be simplified by considering

the flow to be incompressible, leading to a constant density. By further assuming isothermal conditions, the viscosity can also be considered constant. This yields the following simplified continuity equation

$$\nabla \cdot \mathbf{u} = 0. \quad (2.25)$$

Similarly, using the incompressibility assumption combined with the new continuity equation, the momentum equation can be simplified to

$$\frac{\partial \mathbf{u}}{\partial t} + \nabla \cdot (\mathbf{u}\mathbf{u}) = -\frac{\nabla p}{\rho} + \nu \nabla^2 \mathbf{u}, \quad (2.26)$$

where $\nu = \mu/\rho$.

2.3 General Overview Of Modeling Techniques

Historically three parallel movements can be recognized in the analysis of turbulent flows. The first analysis of turbulence was done from a purely *statistical* viewpoint, considering that it was of no utility to precisely determine the exact structure of the turbulent flow, and concentrating instead on trying to characterise its statistical behaviour. Half a century later, experimental wall-bounded turbulent flow data started to show high correlation between velocities at different temporal and spatial positions. It was then recognized that coherent structures must exist within turbulent flows, implying that such flows could therefore not be totally random as was first assumed. This led to a *structural* movement, yielding rich phenomenological descriptions of certain classes of turbulent flows, still of use today when attempting to model and control turbulent flow behaviour. A decade later, with the help of the National Center for Atmospheric Research, the first numerical solutions for models of the Navier-Stokes equations representing critical properties of turbulent flows started to emerge. These early numerical simulations were the first to show that turbulent flows were extremely sensitive to initial conditions, with very slight perturbations developing in highly non-linear responses complex enough to appear as being random. This was the start of the *deterministic* approach, viewing turbulence as a complex and chaotic solution of the Navier-Stokes equations, depending on the variations in time of initial perturbations, and void of randomness. The RANS simulation technique which will be described shortly is primarily *statistical* in nature, whereas the DNS and LES approaches belong to the *deterministic* approach.

2.3.1 RANS

Using equation (2.25), and switching to Einstein notation, the motion of an incompressible fluid is governed by the continuity equation

$$\frac{\partial u_i}{\partial x_i} = 0, \quad (2.27)$$

and the momentum equation

$$\frac{\partial u_i}{\partial t} + \frac{\partial u_i u_j}{\partial x_j} = -\frac{1}{\rho} \frac{\partial p}{\partial x_i} + \nu \frac{\partial^2 u_i}{\partial x_k \partial x_k}. \quad (2.28)$$

The impossibility of solving equations (2.28) and (2.27) under turbulent flow conditions analytically, except for very simple cases, led researchers to try to solve the Navier-Stokes equations

numerically. Unfortunately, computational requirements have long limited such solutions to low Reynolds number flows. Alternative approaches were sought, and led to a method separating the flow properties into a mean and a fluctuating part, in the hope of obtaining a simpler set of equations, albeit at the price of modelling accuracy. This was in fact the approach used originally by Osborne Reynolds at the end of the 19th century in an attempt to define a statistical model for the study of turbulence. The decomposition of the velocity can be written as

$$u_i = \bar{u}_i + u'_i, \quad (2.29)$$

where the averaging \bar{u}_i of u_i can be done in space or in time. A time average of u_i could be written as

$$\bar{u}_i(x_i, t) = \frac{1}{T} \int_{t-T/2}^{t+T/2} u_i(x_i, s) ds. \quad (2.30)$$

The same can be done for the pressure. Substituting these decompositions into equations (2.28) and (2.27) yield the Reynolds Averaged Navier-Stokes equations given by

$$\frac{\partial \bar{u}_i}{\partial x_i} = 0, \quad (2.31)$$

and

$$\frac{\partial \bar{u}_i}{\partial t} + \frac{\partial \overline{u_i u_j}}{\partial x_j} = -\frac{1}{\rho} \frac{\partial \bar{p}}{\partial x_i} + \nu \frac{\partial^2 \bar{u}_i}{\partial x_k \partial x_k}, \quad (2.32)$$

which can be simplified according to the Reynolds averaging rules (see for instance Moran, 1984, p 212) as

$$\frac{\partial \bar{u}_i}{\partial t} + \frac{\partial \bar{u}_i \bar{u}_j}{\partial x_j} = -\frac{1}{\rho} \frac{\partial \bar{p}}{\partial x_i} + \nu \frac{\partial^2 \bar{u}_i}{\partial x_k \partial x_k} - \frac{\partial \overline{u'_i u'_j}}{\partial x_j}. \quad (2.33)$$

These two equations are in the same form as the Navier-Stokes equations, except for the $\overline{u'_i u'_j}$ term. This term, often referred to as the Reynolds stress because of its form, is in fact the representation of the flux of momentum caused by the turbulent fluctuations flowing in or out of the volume under consideration. Equations (2.31) and (2.33) can now be used to simulate a fluctuation-less fluid, travelling with averaged velocity. One should notice that the new set of equations being dealt with is unclosed, as there is no direct means of relating \bar{u} and \bar{p} to the Reynolds stress, and a proper closure model has to be found before the RANS equations can be solved numerically.

Going further into details on the different closure models and limitations of the RANS equations is beyond the scope and interest of this study, and interested readers are informed that more formal and detailed derivations of the RANS equations can be found in various textbooks such as White (2006), Davidson (2004) or Sagaut and Ménéveau (2006).

Analysing equation (2.32) one can understand that the Reynolds Averaged Navier-Stokes equations do not resolve the small eddies present in turbulent flows, but merely try to model the effect of turbulent fluctuations on a mean flow. Such an approach has the advantage of relieving the user of the need to use a fine mesh to capture the viscous turbulent scales present in a flow. Indeed, only a relatively coarse mesh is needed to capture the mean flow variations, while the influence of the turbulent fluctuations on the mean flow are accounted for by the turbulence model.

This intrinsic property of RANS computations therefore limits the scope of simulations to cases where the macroscale flow dynamics are of interest, and can therefore not be used as a tool to investigate small-scale turbulence. This renders RANS simulations inappropriate for the current study.

2.3.2 DNS

The non-linear and complex behaviour of turbulent flows is the consequence of a fairly simple set of equations, the Navier-Stokes equations (NSE), described in equation (2.28). However, as most of the analytical solutions available for the NSE are only of very limited use for engineering applications, alternative solutions of obtaining a complete description of flow variables as a function of space and time have to be sought. This can be done by solving the NSE numerically, through an approach called Direct Numerical Simulations or DNS. When compared to statistical solutions, or even semi-deterministic solutions like LES, DNS computations have the advantage of not requiring *ad hoc* models to obtain a closed set of equations or to model the effects of a range of scales not captured by the computational grid. From this point of view, DNS solutions can be considered exact, as they truly capture all the wavelengths present in the flow.

However, DNS accuracy comes with a heavy computational price, as capturing all length scales present in a flow requires a large amount of grid points due to two constraints. First of all, the domain size has to be large enough to capture the largest scales of turbulent eddies, which is not specific to DNS as it is also a constraint imposed on LES. And secondly, the grid must be sufficiently fine to capture the dissipation length scales of the flow, that is to say the smallest length scales present in the flow. It was shown in section 2.1.1 that the dissipation scales are on the order of the Kolmogorov length scale, which is defined by

$$\eta \sim \left(\frac{\nu^3}{\epsilon} \right)^{\frac{1}{4}}. \quad (2.34)$$

The energy passed down the energy cascade by the larger eddies is of order

$$\Pi \sim \frac{u^2}{l/u} = \frac{u^3}{l}, \quad (2.35)$$

and should be equal to energy dissipation, yielding

$$\epsilon \sim \frac{u^3}{l}. \quad (2.36)$$

The Reynolds number of the large eddies defined as

$$\text{Re}_l = \frac{ul}{\nu}, \quad (2.37)$$

and substitution in equation (2.34) yields

$$\begin{aligned} \eta &\sim \left(\frac{l\nu^3}{u^3} \right)^{\frac{1}{4}} = \left(l^4 \frac{\nu^3}{l^3 u^3} \right)^{\frac{1}{4}} = l \text{Re}_l^{-\frac{3}{4}} \\ \Leftrightarrow \quad \eta &\sim l \text{Re}_l^{-\frac{3}{4}}. \end{aligned} \quad (2.38)$$

From there, an estimate of the minimum number of points required can be made. The mesh interval should be able to capture the smallest eddy size, meaning that the spatial separation of the sampling points cannot be larger than η , that is

$$\Delta x \sim \eta \sim l \text{Re}_l^{-\frac{3}{4}}. \quad (2.39)$$

The number of data points required for a three-dimensional simulation can therefore be approximated by

$$\begin{aligned} N_x &\sim \left(\frac{L_{box}}{\Delta x}\right)^3 \\ \Leftrightarrow N_x &\sim \left(\frac{L_{box}}{l}\right)^3 \text{Re}_l^{\frac{9}{4}}, \end{aligned} \quad (2.40)$$

with L_{box} the length of the domain.

Furthermore, in order to compute the unsteady dynamics of the Kolmogorov scales, the computational time step should be chosen such that $\Delta t \sim (\eta/u_l)$ with u_l the large-scale velocity. The simulation should further be run for several eddy turnover times, each having a value proportional to l/u_l . The number of time steps required for the computations is therefore equal to

$$\begin{aligned} N_t &\sim \frac{T}{\Delta t} \sim \frac{T}{\eta/u_l} \\ \Leftrightarrow N_t &\sim \frac{T}{l/u_l} \text{Re}_l^{\frac{3}{4}}, \end{aligned} \quad (2.41)$$

leading to a total cost of DNS which scales as

$$N_{tot} \propto N_x N_t \sim \left(\frac{T}{l/u_l}\right) \left(\frac{L_{box}}{l}\right)^3 \text{Re}_l^3, \quad (2.42)$$

or $O(\text{Re}_l)^3$. Several studies do however specify that the smallest length scales that must be accurately resolved for an “exact” solution depend on the energy spectrum present in the flow, and can sometimes be larger than the Kolmogorov scales, allowing for larger grid spacings. For instance, Kim et al. (1987) report using a grid spacing of $\Delta x^+ = 12$, $\Delta y^+ = 0.05 - 4.4$ and $\Delta z^+ = 7$ for a Kolmogorov length scale of $\eta \approx 2$, and affirm their resolution is sufficient to capture all essential turbulent scales present in the flow. Similarly Moser and Moin (1987) note that most of the dissipation in the curved channel they studied occurred at scales greater than 15η . Spectral DNS methods in particular tend to show very good agreement with experimental results although the Kolmogorov scales aren’t resolved, whereas on the contrary, finite-difference schemes may require a mesh size of half the Kolmogorov length scale in all directions to obtain the same level of accuracy.

It can in any case be concluded that the costs of DNS are still prohibitive, and that DNS simulations in the near future will be limited to low Reynolds number flows.

2.3.3 LES

Trying to improve on the accuracy and applicability of RANS while decreasing the prohibitive cost associated with the use of DNS, researchers have developed a simulation technique intermediate between the two, called Large-Eddy Simulation (LES).

Through observation, scientists discovered that the isotropic inertial ranges were more or less universal for all turbulent flows and that they could be parametrized by using only the energy transfer rate, through the energy cascade principle. From there, they theorized that if this energy transfer rate could be properly estimated and modelled, they should be able to avoid computing not only the effect of the dissipation scales, but also the scales which could be considered as approximately isotropic and in equilibrium. As estimated in Pope (2000), more than 99% of the computational effort of DNS is devoted to resolving scales in the dissipation range, making LES an attractive computational method. It will be described in more detail in the following section.

2.4 Large Eddy Simulation

As described in the previous subsection, LES is based on the principle that the large scales present in the flow are computed directly, while the dissipation scales and part of the inertial cascade are substituted by specific models.

Its origin can be traced back to the meteorological community in the early 1960's when computational resources were severely limited and alternatives to resolving all the computational scales were sought. Based on the theory of Kolmogorov, the smallest scales present in a flow could be considered as the energy drains from the larger scales, dissipating the turbulent energy into heat, and were assumed to behave isotropically. Thus, the larger eddy scales could be considered as being responsible for most of the kinetic energy transport and are therefore also the most affected by boundary conditions. This requires the direct computation of the large scales, whereas the uniform nature of the small scales make them prime contenders for substitution by simplified computational models. This has led to the LES computational technique, where the large flow scales are computed directly, and where the scales close to the dissipation scales are represented by SubGrid Scale (SGS) models.

2.4.1 Governing Equations

In order to separate the computation of the resolved scales from that of the modelled scales, a filtering operation can be applied to the equations governing the flow motion. Formally, for any flow variable f , LES elements are composed of a large scale and a small scale contribution which can be written as

$$\bar{f} = f - f', \quad (2.43)$$

with the overbar component representing the larger scales, and the prime denoting the contribution of the small scales. From there, one can define a filter to extract the large scale components. This can be done by using a convolution integral over the computational domain defined as

$$\bar{f}(x) = \oint G(x, x'; \Delta) f(x') dx', \quad (2.44)$$

where Δ is the filter width, and is proportional to the wavelength of the smallest scale retained by the filtering operation, and where the convolution integral G , or filter kernel, should satisfy the following relation

$$\oint G(x, x'; \Delta) dx' = 1. \quad (2.45)$$

The most commonly applied filters in LES include the Gaussian filter, defined as

$$G(x, \Delta) = \sqrt{\frac{6}{\pi\Delta^2}} \exp\left(-\frac{6x^2}{\Delta^2}\right), \quad (2.46)$$

and has the advantage of being smooth and differentiable, and the top-hat filter, which is a simple average over a rectangular region.

The top-hat filter is a common choice for finite-volume methods primarily because the average taken is over a grid volume of the finite volume mesh where the variables are a piecewise linear function of x . This implies that when the filter width Δ is chosen to be equal to the grid spacing, the averaged and the local value of \bar{f} will be equal ($\bar{f} = \bar{\bar{f}}$). The top-hat filter is defined as

$$G(x) = \begin{cases} \frac{1}{\Delta} & \text{if } |x'| \leq \Delta/2 \\ 0 & \text{otherwise.} \end{cases} \quad (2.47)$$

Switching to Fourier space allows the use of a filter called the sharp Fourier cutoff filter, eliminating all the wave numbers above a chosen frequency, and is most naturally used in conjunction with spectral methods. However, it tends to be difficult to apply to inhomogeneous flows, and due its nature, it creates a sharp transition between resolved and unresolved scales, which in practice, might hamper the energy transfer from the larger to the smallest scales, resulting in an energy build-up in the larger scales. The sharp Fourier cutoff filter is defined in Fourier space as

$$\hat{G}(k) = \begin{cases} 1 & \text{if } k \leq \pi/\Delta \\ 0 & \text{otherwise.} \end{cases} \quad (2.48)$$

For extra information on the different type of filters and their effect the reader can refer to LES literature as Sagaut and Ménéveau (2006) and Bernard and Wallace (2002).

It should be noted that many researchers have recently moved away from the filtering concept, to use the variational multiscale approach. In the variational multiscale method, modeling is confined to the effect of small-scale Reynolds stress, as opposed to classical LES methods in which the entire subgrid-scale stresses are modeled. Due to classical approach implemented in the CFD packaged used for this simulations of the current study, variational multiscale methods are beyond the scope of this master thesis. For more information on the method, readers can consult the original paper by Hughes et al. (2000).

Applying the filtering operation given by (2.44), one obtains the filtered version of the incompressible Navier-Stokes equations. The continuity equation becomes

$$\frac{\partial \bar{u}_i}{\partial x_i} = 0, \quad (2.49)$$

and similarly, the following momentum equation is obtained

$$\frac{\partial \bar{u}_i}{\partial t} + \frac{\partial \bar{u}_i \bar{u}_j}{\partial x_j} = -\frac{1}{\rho} \frac{\partial \bar{p}}{\partial x_i} + \nu \frac{\partial^2 \bar{u}_i}{\partial x_k \partial x_k}, \quad (2.50)$$

which is identical to (2.32). However, from here, it is important to notice that because

$$\overline{u_i u_j} \neq \bar{u}_i \bar{u}_j, \quad (2.51)$$

and because the quantity $\overline{u_i u_j}$ is not easily computed, a modeling approximation has to be found for this term. By introducing the difference between both sides of the inequality as

$$\tau_{ij} = \overline{u_i u_j} - \bar{u}_i \bar{u}_j, \quad (2.52)$$

Equation (2.50) can be re-written as

$$\frac{\partial \bar{u}_i}{\partial t} + \frac{\partial \bar{u}_i \bar{u}_j}{\partial x_j} = -\frac{1}{\rho} \frac{\partial \bar{p}}{\partial x_i} - \frac{\partial \tau_{ij}}{\partial x_j} + \nu \frac{\partial^2 \bar{u}_i}{\partial x_k \partial x_k}. \quad (2.53)$$

The term τ_{ij} is referred to in LES as the subgrid-scale (SGS) stress tensor, and can be considered as the term accounting for the effect of the small, unresolved scales which have to be modelled. By decomposing the velocity vector as $u = \bar{u} + u'$, the SGS stress can be decomposed into different terms as follows

$$\begin{aligned} \tau &= \overline{(\bar{u}_i + u'_i)(\bar{u}_j + u'_j)} - \bar{u}_i \bar{u}_j \\ &= (\overline{\bar{u}_i \bar{u}_j} - \bar{u}_i \bar{u}_j) + \left(\overline{\bar{u}_i u'_j} + \overline{u'_i \bar{u}_j} \right) + \overline{u'_i u'_j} \\ &= L_{ij} + C_{ij} + R_{ij}, \end{aligned} \quad (2.54)$$

where

$$\begin{aligned}
 L_{ij} &= \overline{\overline{u_i u_j}} - \overline{u_i} \overline{u_j} \\
 C_{ij} &= \overline{\overline{u_i u'_j}} + \overline{u'_j \overline{u_i}} \\
 R_{ij} &= \overline{u'_i u'_j}.
 \end{aligned}
 \tag{2.55}$$

The first term L_{ij} is generally known as the Leonard stress, and represents the interaction of the large eddies which produces subgrid turbulence. As this quantity is resolved, it can be computed directly from the velocity field. The second term, C_{ij} , often referred to as the ‘‘cross-term’’ stress, is a measure of the energy transfer between the resolved and the unresolved scales of the flow, and can transfer energy in either direction as a function of the sign of the fluctuations u' . However, following the energy cascade assumption, the average energy transfer is from the larger to the smaller scales. The last term represents the interaction of the small, unresolved eddies, and is known as the subgrid Reynolds stress.

Although (2.54) seems an attractive description of the SGS stresses, it is quite challenging to model due to the dependence of the Leonard and cross stresses on the type of reference frame used. As it stands, the total SGS stress and the SGS Reynolds stress term are independent of the reference frame used, while the Leonard and cross stresses are not. To make matters worse, the correlation terms used to model the different elements of this SGS decomposition tend to be approximations containing substantial errors that largely offset the targeted gain of accuracy which motivated the decomposing of the subgrid stress term in the first place. Therefore, although Germano (1986) came with a Galilean invariant redefinition of the turbulent stresses used here-above, modern applications of filtered LES have largely abandoned the decomposition of subgrid stresses in favour of a modelling of the SGS term τ_{ij} as a whole.

2.4.2 Subgrid-Scale Models

The main role of subgrid-scale models is to remove the energy from the resolved scales in a manner mimicking the drain associated with energy cascade theory. This subsection will present the most commonly used subgrid-scale modelling approaches.

Smagorinsky Models

The simplest and oldest approach to subgrid-scale modeling was introduced by Smagorinsky in the early 1960’s and models the subgrid-stress tensor by using an extension of the eddy-viscosity assumption developed by Boussinesq in the 1870’s. The general idea behind the Boussinesq approximation is that the turbulent mixing momentum has a contribution similar to the molecular transport of momentum, described by

$$\nu \frac{\partial^2 u_i}{\partial x_k \partial x_k}
 \tag{2.56}$$

term in equation (2.53). From there, Boussinesq postulated that the effect of turbulent mixing of momentum was to increase the effective viscosity locally. He therefore proposed to model the SGS stress similarly to the laminar stress, by introducing an eddy viscosity ν_τ . Following the eddy-viscosity model, the subgrid-stress tensor can be written as

$$\tau_{ij} = -2\nu_\tau \overline{S_{ij}} + \frac{\delta_{ij}}{3} \tau_{kk},
 \tag{2.57}$$

where the term \overline{S}_{ij} is referred to in literature as the strain-rate tensor, and can be computed from the filtered velocity \overline{u} using the relation

$$\overline{S}_{ij} = \frac{1}{2} \left[\frac{\partial \overline{u}_i}{\partial x_j} + \frac{\partial \overline{u}_j}{\partial x_i} \right]. \quad (2.58)$$

As closure model, Smagorinsky chose to approximate the viscosity term ν_τ as a function of the strain-rate tensor, leading to

$$\nu_\tau = C_S^2 \Delta^2 (2\overline{S}_{ij}\overline{S}_{ij})^{\frac{1}{2}}, \quad (2.59)$$

with C_S a dimensional constant referred to as the Smagorinsky constant, and with Δ a measure of the filter width. The Smagorinsky model further assumes that the small unresolved scales are in equilibrium and instantly dissipate all the energy they received from the resolved scales.

When using the SGS tensor defined in (2.57), the LES momentum (2.53) will be slightly re-written as

$$\frac{\partial \overline{u}_i}{\partial t} + \frac{\partial}{\partial x_j} (\overline{u}_i \overline{u}_j) = -\frac{1}{\rho} \frac{\partial p^*}{\partial x_i} - \frac{\partial \tau_{ij}}{\partial x_j} + \nu \frac{\partial^2 \overline{u}_i}{\partial x_k \partial x_k}, \quad (2.60)$$

where p^* is a modified pressure term accommodating the isotropic part of the stress tensor τ_{kk} to avoid its computation, and is written as

$$p^* = \overline{p} - \frac{1}{3} \rho \delta_{ij} \tau_{kk}. \quad (2.61)$$

For open turbulent flows the Smagorinsky constant takes values between 0.18 and 0.23. A detailed description of one of the methods allowing the evaluation of the Smagorinsky constant can be found in Lilly (1967). However, Bernard and Wallace (2002) warn that the values for C_S given here above were found to be overly diffusive in flows containing mean shear, such as wall-bounded flows, and that a lower value of C_S should be chosen for those types of flows. They found that a value of $C_S = 0.065$ gave better predictions for wall bounded flows.

As can be seen, the major disadvantage of the Smagorinsky model is that it requires different values for the constant C_S for different flow conditions, which is a serious drawback when simulating complex and varying flow conditions. Another weakness of the Smagorinsky model stems from the assumption of isotropy of the unresolved scales made when choosing for an eddy-viscosity based model. While the isotropy conditions holds for a large subset of flows and filters, it is far from being universal. For instance, choosing for a large mesh spacing may induce anisotropic motions in the unresolved scales. Similarly, near a solid boundary even the smallest scales do not conform to the isotropy assumptions, with the added problem that anisotropic grids will often resolve even isotropic eddies differently depending on their orientation. Although these problems can be reduced by increasing the mesh refinement, the problem as whole is better addressed by trying to avoid the isotropy assumption.

Adding to the deficiencies named here above, the accuracy of the Smagorinsky model is further degraded the more the flow conditions deviates from the assumption of equilibrium of the unresolved scales made when trying to find a relation for the subgrid eddy-viscosity. Quite unfortunately, non-equilibrium conditions are often encountered in turbulent flows, and are common in applications ranging from separating and reattaching flows, to boundary layer flows and wall dominated domains. This effect is therefore non-negligible.

One-Equation Models

In order to try to improve on the accuracy of the Smagorinsky model by dropping the assumption of equilibrium of the unresolved scales the one-equation family of models was developed. Most one-equation models are, as the Smagorinsky model, based on the eddy-viscosity concept. As an improvement, they try to add a history effect to the model by solving extra equations, such as transport equations, for one or more of the subgrid turbulence characteristics. One of the quantities often chosen for the extra transport equation is the subgrid-scale kinetic energy, defined as

$$K_{sgs} \equiv \frac{1}{2} \sum_i \tau_{ii}, \quad (2.62)$$

which provides an SGS velocity scale to the model. Other potential transport equation candidates include the transported SGS viscosity, or the transported SGS vorticity, as presented in de Villiers (2006, chap 3).

The eddy-viscosity model can then be cast in the form

$$\nu_\tau = C_K \Delta \sqrt{K_{sgs}}. \quad (2.63)$$

According to Horiuti (1985), the K_{sgs} transport equation then takes the form

$$\frac{\partial K_{sgs}}{\partial t} + \bar{u}_j \frac{\partial K_{sgs}}{\partial x_j} = \frac{1}{2} \tau_{ij} \bar{S}_{ij} + \frac{\partial}{\partial x_j} \left[\left(C_{kk} \Delta \sqrt{K_{sgs}} + \nu \right) \frac{\partial K_{sgs}}{\partial x_j} \right] - C_\epsilon \frac{K_{sgs}^{3/2}}{\Delta}, \quad (2.64)$$

where the different constants take the value $C_K = 0.05$, $C_\epsilon = 1.0$ and $C_{kk} = 0.1$ respectively.

As a whole, the one-equation models mostly suffer from the same deficiencies as the Smagorinsky type of models due to the common choice of eddy-viscosity approach and the consequent assumption of isotropy of the unresolved scales. The one-equation models do however have the advantage of providing a more accurate time scale to the unresolved scale-model through the independent definition of the velocity scale in the extra transport equation. As a result, a study of the performance of different SGS models in channel flows by Fureby et al. (1997) has shown the one-equation model to be quite effective and superior to algebraic models of the Smagorinsky type.

Dynamic Models

Unsatisfied with the inability of the previously mentioned subgrid-scale models to correctly represent different turbulent fields and flow regimes with a single universal constant, researchers oriented their studies towards dynamical methods allowing the computation of SGS coefficients using local flow conditions. The first of such methods was presented by Germano et al. (1991), and has the advantage of also being applicable to the previously described models. In dynamic models, the coefficients of the SGS models are determined as part of the flow calculations, and use the energy content of the smallest resolved scales to locally determine the value of the closure coefficients. This imposes, however, the assumption that the behaviour of the smallest resolved scales is analogous to that of the subgrid scales.

The new dynamic model by Germano et al. (1991) is based on the introduction of two filters. In addition to the original grid filter Δ -also referred to in literature as $\bar{\Delta}$ - defining the resolved and subgrid scales, a new test filter $\hat{\Delta}$ is introduced, which differs from the original grid filter by its smoothing over a larger flow region. The application of the grid filter to the Navier-Stokes equations yielded the subgrid-stress tensor found in (2.52) which was formally written as

$$\tau_{ij} = \overline{u_i u_j} - \bar{u}_i \bar{u}_j.$$

This equation was then re-written in the Smagorinsky model by casting the SGS tensor in the eddy-viscosity form, and led to (2.57). Piomelli and Liu (1995) re-wrote this expression slightly as

$$\begin{aligned}\tau_{ij} - \frac{\delta_{ij}}{3}\tau_{kk} &= -2C_{dyn}\Delta^2 |\overline{S}| \overline{S}_{ij} \\ &= -2C_{dyn}\beta_{ij},\end{aligned}\tag{2.65}$$

where the quantity C_{dyn} has replaced the square of the original Smagorinsky coefficient C_S .

Similarly, the introduction of a new test filter introduces a new set of stresses, or subtest-scale stresses, defined formally as

$$T_{ij} = \widehat{\overline{u_i u_j}} - \widehat{\overline{u_i}} \widehat{\overline{u_j}}.\tag{2.66}$$

In similar fashion to (2.65), this equation can be expressed in terms of a Smagorinsky type closure as

$$\begin{aligned}T_{ij} - \frac{\delta_{ij}}{3}T_{kk} &= -2C_{dyn}\widehat{\Delta}^2 |\widehat{S}| \widehat{S}_{ij} \\ &= -2C_{dyn}\alpha_{ij},\end{aligned}\tag{2.67}$$

where

$$\widehat{S}_{ij} = \frac{1}{2} \left(\frac{\partial \widehat{u_i}}{\partial x_j} + \frac{\partial \widehat{u_j}}{\partial x_i} \right),\tag{2.68}$$

and where typically

$$\widehat{\Delta} = 2\Delta.\tag{2.69}$$

From there, the major contribution to the subgrid-scale model brought in by Germano et al. (1991) was to identify that keeping consistency between (2.65) and (2.67) depended on a proper choice of C_{dyn} . Although cases where the two values of C_{dyn} could differ are not difficult to find, as in wall-bounded flows where the test filter can experience very different local phenomena than the grid filter, Germano et al. (1991) chose to make no distinction between the two coefficients. According to various literature references (e.g. Lilly, 1992, Piomelli and Liu, 1995 or Bernard and Wallace, 2002) a proper choice of C_{dyn} can be made by finding an identity relating the resolved turbulent stress

$$L_{ij} = \widehat{\overline{u_i u_j}} - \widehat{\overline{u_i}} \widehat{\overline{u_j}}\tag{2.70}$$

to the subgrid and subtest-scale stresses. From the definitions of equation (2.52) and (2.66), it follows that the resolved part of the SGS stress can be linked to the subgrid and subtest-scale stress by

$$L_{ij} = T_{ij} - \widehat{\tau_{ij}}.\tag{2.71}$$

Substitution of (2.65) and (2.67) into (2.71) yields

$$L_{ij} = -2C_{dyn}\alpha_{ij} + 2\widehat{C_{dyn}}\widehat{\beta_{ij}},\tag{2.72}$$

with

$$\beta_{ij} = \Delta^2 |\overline{S}| \overline{S}_{ij},\tag{2.73}$$

and

$$\alpha_{ij} = \widehat{\Delta}^2 |\widehat{\mathcal{S}}| \widehat{\mathcal{S}}_{ij}. \quad (2.74)$$

However, the set of equations (2.65), (2.67), (2.71), (2.73) and (2.74) are five independent equations which cannot be solved explicitly for C_{dyn} because it appears in a filtering operation through (2.72). The further assumption that the coefficient C_{dyn} is only a function of time and space, and not filter width allows to write the following

$$\widehat{C_{dyn}\beta_{ij}} = C_{dyn}\widehat{\beta_{ij}}, \quad (2.75)$$

circumventing this problem.

The next problem arising when trying to determine C_{dyn} is the fact that C_{dyn} is now overdetermined by the set of 5 equations referenced here-above. To avoid this problem, Lilly (1992) proposed to determine C_{dyn} using the least square approach by minimizing the error produced by (2.72). In least-square terms the error is defined as

$$Q = \left(L_{ij} + 2C_{dyn}\alpha_{ij} - 2C_{dyn}\widehat{\beta_{ij}} \right)^2. \quad (2.76)$$

Upon setting $\frac{\partial Q}{\partial C_{dyn}} = 0$, the coefficient C_{dyn} can be determined as

$$C_{dyn} = -\frac{1}{2} \frac{L_{ij} (\alpha_{ij} - \widehat{\beta_{ij}})}{(\alpha_{ij} - \widehat{\beta_{ij}}) (\alpha_{ij} - \widehat{\beta_{ij}})}. \quad (2.77)$$

A later study by Ghosal et al. (1995) found the method developed above to contain non-negligible mathematical inconsistencies coupled with numerical instabilities due to possible sharp fluctuations in the value of C_{dyn} . Although not thoroughly documented, a commonly applied workaround to this problem was to average the numerator and the denominator of (2.77) over a homogeneous flow direction. Despite the fact that this workaround showed in some cases very good agreement with DNS results, it still has the disadvantage of being an *ad hoc* procedure limiting generalization of these types of dynamic models, with the added limitation of requiring a least one homogeneous direction in the flow under consideration, seriously restricting the type of flows the dynamic model can simulate. An other common workaround only applicable to isotropic turbulent flows, is to take an average over the whole computational domain, leading to $C_{dyn} = C_{dyn}(t)$.

Evaluation of Flat Plate Reference Results

Historically, experimental turbulent flat plate boundary layers have been extensively and thoroughly studied by scientists trying to determine non-dimensional scalings for turbulent flow properties. The wealth of experimental data available made it a logical step to use experimental measurements as benchmark results to assess the accuracy of early numerical flat plate simulations. Over time, as available computational resources became more significant, low Reynolds number DNS computations started to surpass the accuracy experimental measurements could offer, due to probe size limitations. In parallel, numerical computations started showing very good agreement between different simulations of channel flow test cases, leading to a general agreement that low Reynolds number DNS simulations could be considered more accurate than their experimental counterparts.

In order to test the performance of different type of turbulent inflows, a representative test case was sought as a benchmark. As explained in the introduction, the canonical zero pressure-gradient turbulent flat plate was chosen due to its sensitivity to the quality of the turbulent information within the boundary layer. At the time of writing, the DNS data of Schlatter and Örlü (2010) and that by Simens et al. (2009) were considered the highest quality flat plate data available, and were both used as reference solution for the current study. However, a detailed comparison of both data sets revealed slight differences which are illustrative of the sensitivity of numerical computations to artificial boundary conditions. This short chapter will therefore try to highlight the most relevant differences noticed between both DNS results, but will also serve as a general warning to researchers by emphasising some of the mismatches which can be expect in low Reynolds-number experimental and numerical flat plate data.

3.1 General Turbulent Flat Plate Discrepancies

As mentioned in the introduction, the lack of independent skin friction measurements has a direct effect on the usability of the experimental data as reference solution, as the scaling relations

derived from such data will be inaccurate. As an example, the current author was unable to match the $\overline{u'^2}^+ \sqrt{c_f/2}$ scaling derived from experimental data in the reference work by DeGraaff and Eaton (2000) to DNS data from Schlatter and Örlü (2010) or Simens et al. (2009), in spite of the fact that the two data sets were in the same Reynolds number range. The scaling in question was applied as data non-dimensionalization to allow the partial collapse of the $\overline{u'^2}^+$ stress, when plotted on a logarithmic y^+ scale. Unfortunately, no such collapse could be obtained.

As explained in the introduction, . Comparing six DNS computations made after 2002, the authors discovered that the simulation of the same canonical flat plate flow also gave surprisingly inconsistent results, even for such basic quantities as shape factor, friction coefficient and fluctuation maximum.

The lack of fully established reference data for low Reynolds-number flat plate experiments led Schlatter and Örlü to investigate whether the similar disparities could be found in recent Direct Numerical Simulation data. After finding surprisingly inconsistent results for such basic quantities as shape factor and friction coefficient, Schlatter and Örlü further analysed the various DNS data to conclude that such differences came from different choices in numerical domain sizes and boundary conditions. They further concluded that the two computations with the largest domains, i.e. their own simulation and that by Simens et al. (2009), were also the ones that yielded the most similar results compared to established turbulent relations and compared to each other.

3.2 Comparing DNS Data From Schlatter and Örlü (2010) and Simens et al. (2009)

In this section, the relevant differences between DNS data from Schlatter and Örlü (2010) and Simens et al. (2009) will be highlighted. The simulation parameters of both DNS computations can be found in table 3.1, with the domain sizes normalized by δ_0 , the inflow boundary layer thickness used in the current study. As an indication, the domain size used for the computations in this master thesis also appear in the table.

Table 3.1: Domain parameters for the DNS computations by Schlatter and Örlü (2010), Simens et al. (2009), and for the current setup

	Re_θ	$(L_x, L_y, L_z)/\delta_0$	Inlet	Outlet	Top
Schlatter and Örlü (2010)	180 - 4300	$5228 \times 174 \times 210$	Laminar + Tripping	Fringe Region	Neumann
Simens et al. (2009)	620 - 2140	$143 \times 7.74 \times 23.52$	Recycled Type Inflow	Convective Outflow	Suction
Current Study	620 - 1330	$60 \times 4 \times 8$	Recycled Type Inflow	Zero Gradient	Neumann

For clarity it should be added that all simulations use cyclic-type boundary conditions in the spanwise direction. However, from table 3.1, one can directly notice that the simulation by Schlatter and Örlü and by Simens et al. use very dissimilar domain sizes and boundary conditions. Noticeably so for the top of the domain, to which Simens et al. needed to apply suction to obtain proper boundary layer growth. In contrast, Schlatter and Örlü have enough domain height to

simply apply a Neumann boundary condition to the velocity vector.

Further comparing the DNS results by Schlatter and Örlü to that by Simens et al., noticeable differences were observed in the streamwise evolution of non-dimensional wall-normal mean velocity V^+ , as illustrated in figures 3.1 and 3.2.

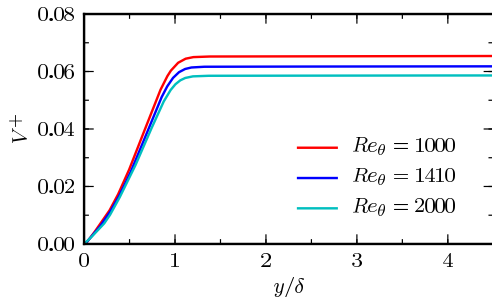


Figure 3.1: V^+ for increasing Reynolds number, from Schlatter and Örlü (2010)

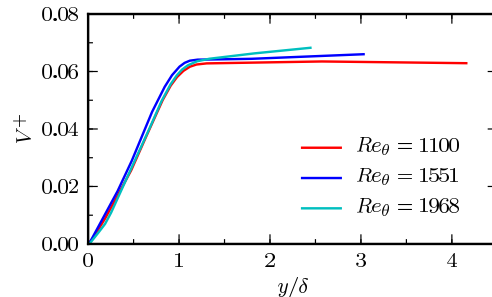


Figure 3.2: V^+ for increasing Reynolds number, from Simens et al. (2009)

It is clear that, although both simulations represent the same canonical test case, the non-dimensional wall-normal velocities display a very different evolution with increasing Reynolds number. The simulation by Schlatter and Örlü shows a decrease of non-dimensional mean with increasing Reynolds number, while the simulation by Simens et al. shows the exact opposite trend. It is also important to notice that all the non-dimensional velocities from the data by Schlatter and Örlü are constant beyond $y/\delta = 1.25$, a trend which can only be seen in the lowest Reynolds number mean by Simens et al.. Coincidentally, the top boundary condition of the domain from Schlatter and Örlü is clearly located much further away from the boundary layer than in the simulation by Simens et al..

One could argue that, because the mean velocity in wall-normal direction is three orders of magnitude smaller than that in streamwise direction, the changes shown here-above could be considered irrelevant. However, it was found during this thesis that the wall-normal mean velocity had a large influence on the quality of the boundary layer computed, probably due to its influence on boundary layer growth. There is, of course, no guarantee that DNS computations would be affected in the same way, but it is something worth investigating.

It should also be noted that the non-dimensional units chosen in figures 3.1 and 3.2 could mask a correct dimensional evolution of velocity, due to slight errors in derived quantities such as skin friction c_f and viscous velocity u_τ . No dimensional data was available for the DNS data from Schlatter and Örlü, preventing a dimensional comparison with the data of Simens et al. (2009). Nonetheless, the data by Simens et al. can be used for a one-sided qualitative analysis. The dimensional velocity from Simens et al. (2009) is shown in figure 3.3. Using Moran (1984, p 200), the mean wall-normal velocity at the boundary layer edge for incompressible flows can be defined as

$$V_n = \frac{d}{dx} (U_\infty \delta^*), \quad (3.1)$$

with δ^* the displacement thickness. Further assuming that the mean velocity U_∞ is constant

yields

$$V_n = U_\infty \frac{d\delta^*}{dx}. \quad (3.2)$$

From equation (3.2), one can infer that for zero pressure-gradient boundary layers the mean velocity in wall-normal direction will decrease going downstream, since the derivative of the displacement thickness is decreasing.

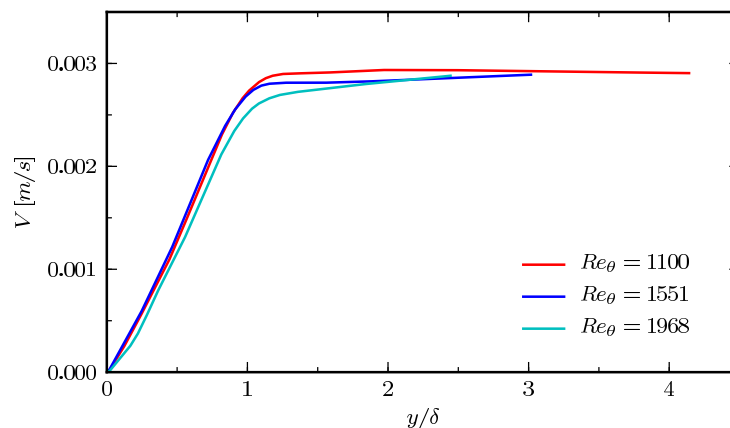


Figure 3.3: V for increasing Reynolds number, from Simens et al. (2009)

From figure 3.3, it is clear that the dimensional velocity change as a function of Reynolds number is not what was anticipated by equation (3.2), as the mean velocity beyond the boundary layer edge at $Re_\theta = 1968$ is similar to that at $Re_\theta = 1551$. This might be an indication of wall-normal mean velocity mismatch due to the influence of artificial boundary conditions. This conjecture is supported by the fact that the top of the domain is only located at $1.5 \delta_0$ from the boundary layer at $Re_\theta = 1968$. It is suspected that the DNS results by Schlatter and Örlü will be less influenced by the top boundary condition, due to the higher domain available.

Nonetheless, it is important to assess whether both DNS computations do have similar boundary layer growth rate. This can be estimated by comparing the evolution of the displacement thickness Reynolds number Re_{δ^*} as a function of the momentum thickness Reynolds number Re_θ , as show in figure 3.4. An indirect estimate of boundary layer growth could also be done, by comparing the evolution of the skin friction, c_f , as a function of Re_θ . This can be seen in figure 3.5.

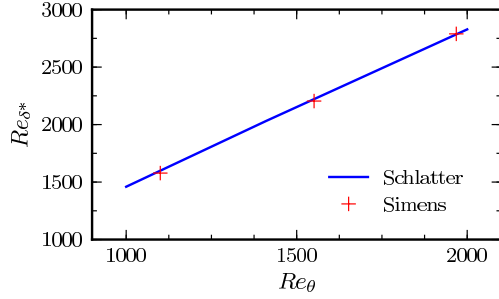


Figure 3.4: Comparison of displacement thickness growth as a function Re_θ

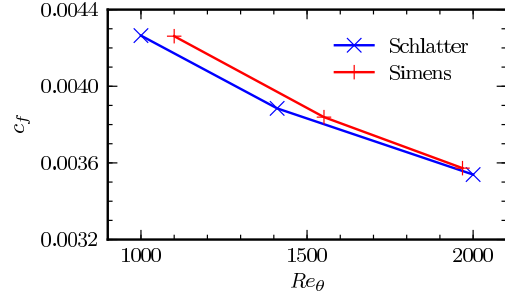


Figure 3.5: Comparison of friction coefficient evolution as a function Re_θ

From figure 3.4, one can observe that both boundary layers have a nearly identical displacement thickness evolution as a function of Re_θ , which seems to indicate that they are both growing at the same rate, a comforting thought. Analysing figure 3.5, it can be seen that the two DNS computations have a slightly different friction coefficient evolution when progressing downstream. Although this could partly explain the differences observed between figure 3.1 and 3.2 through the influence of a scaling by u_τ , it cannot explain the mismatch observed in figure 3.3, as the quantities observed are independent of any viscous scaling.

Inflow Boundary Condition Treatment and Flow Control

Spatially evolving turbulence poses an extra challenge to numerical simulation approaches, as in most cases the flow downstream is highly dependent on the conditions at the inlet. Ensuring the correct development of all turbulent properties therefore imposes stringent requirements on the inflow condition. Conversely, poorly-defined inflow conditions will result in undesirably long adaptation lengths, wasting useful computational resources. In this light, the following chapter will introduce various inflow modeling techniques applied to the Large-Eddy Simulation (LES) of incompressible flat-plate boundary layers.

This chapter will be subdivided into four parts. The first section will start with a brief overview of the different inflow strategies which can be used for turbulent inflow generation. The focus will then shift towards describing the different inflow modeling approaches used for this master thesis, first presenting an inflow model developed by Lund et al. (1998), then describing a simple outer-coordinate rescaling technique and a random-perturbation inflow developed by the present author, and finally introducing a flow forcing technique by Spille-Kohoff and Kaltenbach (2001) which can be used to improve inaccurate inflow conditions.

4.1 Generation of Turbulent Inflow Data for Spatially Developing Boundary Layers

The simulation of turbulent boundary layers requires detailed and precise inflow information to ensure all the flow properties in the computational domain evolve as their physical counterparts. In the case of LES, the largest of the unsteady and three-dimensional energy carrying eddies are resolved, requiring that the inflow should represent an as realistic as possible boundary condition for those eddies. Failing to deliver the proper structural information with the inflow

condition will result in the flow having to undergo adjustments until eddies are generated with the correct phase information. This puts stringent requirements on the inflow velocity vector. Several strategies have been developed to try to come up with consistent inflow condition for the computation of spatially developing boundary layer flows, and will be presented hereafter. This section is similar to the short historical review of artificial boundary conditions made in the introduction to this thesis, but describes the various inflow strategies in slightly more detail.

Early approaches to turbulent inflow modeling used random velocity fluctuations imposed on a mean flow. Although it is quite feasible to match the different moments and energy spectra per wavelength using random models, the phase information is somewhat more delicate to obtain, as it is strongly dependent on the type of flow and the location within the flow under consideration. Researchers soon found out that supplying white noise as random turbulence did not provide correct energy levels at the right wavelengths, which resulted in a rapid damping of the turbulence back to laminar conditions. From there, researchers tried to improve on the random fluctuation method by developing better random models with correlation information provided by experimental results, with varying degrees of success. For instance, simulations by Lee et al. (1992) using velocity perturbations with a prescribed power spectrum and random phase information resulted in adaptation lengths over $12 \delta_0$ before the flow could be considered physically realistic. Batten et al. (2004) concentrated on building a fluctuation field based on a superimposition of Fourier-modes with random-based phase and amplitude information also include anisotropy information, and reported that at least 20 boundary layer thicknesses were needed to obtain a physically realistic flow. More successfully, Pamiès et al. (2009) improved on an approach by Marusic (2001) which showed that channel flow mean and Reynolds-stress profiles could be matched accurately by superimposing analytical hairpin-like vortical structures on a mean profile. They achieved realistic friction coefficient and shape factor growth within $6 \delta_0$ of the inflow. For further information one can consult the excellent introduction of the paper by Pamiès et al. (2009), the paper by Keating et al. (2004), or for a detailed review, the book by Sagaut et al. (2006).

Another approach to the generation of inflow condition for turbulent numerical simulations makes use of secondary simulations or precursor databases to provide turbulent information to a primary computation. This is done using a separate calculation of an equilibrium flow with periodic boundary conditions, storing the velocity field of a plane normal to the streamwise direction at each time step, and then re-using the information obtained as inflow data for the simulation of a more complex turbulent flow. This method has the advantage of facilitating the control of different boundary layer parameters, such as the friction coefficient, and the displacement and momentum thicknesses, but at the considerable cost of having to run a precursor simulation. A variant of such an approach was developed by Schlüter et al. (2004) for hybrid RANS/LES computations, and showed good agreement with experimental results. The method had the advantage of not requiring the precursor simulation to be at the same Reynolds number as the real LES study, or in the same configuration. An alternative approach was implemented by Druault et al. (2005), who reconstructed data from experimental measurements to use as inflow conditions for LES simulations. They claimed obtaining good results, although they did not specify the adaptation length needed by their approach.

A third type of inflow modeling strategy includes the recycling methods pioneered by Spalart and Leonard (1985) and relies on providing inflow conditions using turbulent information obtained from within a computational domain. The original method by Spalart and Leonard (1985) was further improved in Spalart (1988), and applied to flat plate computations. It made use of an ingenious coordinate transformation allowing for the calculation of spatially evolving boundary layers while keeping a form of periodic boundary conditions. The results published by Spalart (1988) proved to be acceptable, although the computed friction coefficient was overestimated by

5% compared to experimental measurements, and the $\langle uu \rangle$ and $\langle ww \rangle$ spectra did not collapse to the Kolmogorov energy spectrum law of $\kappa^{-\frac{5}{3}}$ when normalized with ν and u_τ . Their work later inspired Lund et al. (1998) to develop a similar recycling method, while circumventing the need of an unwieldy coordinate transformation. They extracted a velocity field downstream of the inflow, and rescaled it to compensate for boundary layer growth, achieving an adaptation length of $8\delta_0$. Simplifying the approach of Lund et al. by only using an outer-coordinate rescaling, Spalart et al. (2006) managed to further decrease the adaptation length to $4\delta_0$, based on skin friction coefficient evolution.

Although the Lund et al. family of inflows show very promising results, the rescaling procedures used are based on the assumption of equilibrium turbulent flows, limiting their scope of applicability. They have also been shown, in some cases, to add unphysical forcing to the computed flow due to the introduction of a form of temporal periodicity (see for instance Simens et al., 2009). Simulating more general wall-bounded turbulent flows will therefore require more versatile inflow conditions.

4.2 Recycling and Rescaling Methods

Based on a personal study, Lund et al. (1998) concluded that Spalart-type inflows produced the most accurate inflow condition for the case of spatially developing boundary layers on a flat plate, with the added benefit of also providing the best control over skin friction and momentum thickness of the flow entering the domain. Their primary complaint about the Spalart method was that it was slightly difficult to understand and implement, with the added drawback that the coordinate transformation of the Navier-Stokes equation, based on boundary-layer growth, required a special-purpose flow solver. From there, Lund et al. decided to develop a recycling method keeping the skin friction and momentum thickness control offered by the method from Spalart, but not requiring a coordinate transformation of the Navier-Stokes equations. Capitalizing on the quality of the inflow method by Lund et al., Spalart et al. (2006) simplified it even further, and also managed to further decrease the adaptation length in the process.

The following subsections will present the recycling and rescaling methods by Lund et al. (1998) and by Spalart et al. (2006) which will be implemented for the current research.

4.2.1 The Recycling and Rescaling Method by Lund, Wu, and Squires (1998)

The main idea behind the recycling and rescaling type of inflows is to extract data at a station downstream from the inflow, and rescale it to account for boundary layer growth. In the approach by Lund et al., the flow at the extraction station is averaged in spanwise direction and in time, to allow the decomposition of the flow field in a mean and fluctuating part as

$$u'_i(x, y, z, t) = u_i(x, y, z, t) - U_i(x, y), \quad (4.1)$$

with x , y and z denoting the streamwise, wall-normal and spanwise directions respectively, and where the subscript i is part of the so-called Einstein notation, and implies an operation on every component of a variable.

The mean velocities and fluctuations are then rescaled according to the law of the wall in the inner region, and the defect law in the outer region, and then blended together using a weighted average of the inner and outer profiles. For a more detailed description of these laws, please refer to section (2.1.2).

The perturbations are rescaled according to

$$u'_{i, \text{infl}}{}^{\text{inner}} = \gamma u'_{i, \text{recy}}(y_{\text{infl}}^+, z, t) \quad (4.2)$$

and

$$u'_{i, \text{infl}}{}^{\text{outer}} = \gamma u'_{i, \text{recy}}(\eta_{\text{infl}}, z, t), \quad (4.3)$$

with the subscript recy referring to the data from the recycling plane, the subscript infl to that from the inflow, and where the parameter γ is defined as

$$\gamma = \frac{u_{\tau, \text{infl}}}{u_{\tau, \text{recy}}}. \quad (4.4)$$

These equations also contain inner coordinates y^+ defined as

$$y^+ = \frac{y u_{\tau}}{\nu}, \quad (4.5)$$

and outer coordinates η defined as

$$\eta = \frac{y}{\delta}, \quad (4.6)$$

with u_{τ} the local viscous velocity and δ the local boundary layer thickness.

The rescaling of the mean profiles differs per velocity component. The mean in x direction is rescaled as

$$U_{1, \text{infl}}^{\text{inner}} = \gamma U_{1, \text{recy}}(y_{\text{infl}}^+) \quad (4.7)$$

$$U_{1, \text{infl}}^{\text{outer}} = \gamma U_{1, \text{recy}}(\eta_{\text{infl}}) + (1 - \gamma)U_{\infty}, \quad (4.8)$$

with U_{∞} the freestream velocity. The mean in y direction is rescaled as

$$U_{2, \text{infl}}^{\text{inner}} = U_{2, \text{recy}}(y_{\text{infl}}^+) \quad (4.9)$$

and

$$U_{2, \text{infl}}^{\text{outer}} = U_{2, \text{recy}}(\eta_{\text{infl}}). \quad (4.10)$$

The mean velocity in z direction is set to zero, as flows without spanwise gradients are considered here.

The velocity profiles are then assembled as

$$u_{i, \text{infl}} = \left[U_{i, \text{infl}}^{\text{inner}} + u'_{i, \text{infl}}{}^{\text{inner}} \right] [1 - W(\eta_{\text{infl}})] + \left[U_{i, \text{infl}}^{\text{outer}} + u'_{i, \text{infl}}{}^{\text{outer}} \right] W(\eta_{\text{infl}}), \quad (4.11)$$

with the weighting function $W(\eta)$ defined as

$$W(\eta) = \frac{1}{2} \left\{ 1 + \frac{1}{\tanh(\alpha)} \tanh \left[\frac{\alpha(\eta - b)}{(1 - 2b)\eta + b} \right] \right\}, \quad (4.12)$$

and the coefficients chosen as $\alpha = 4$ and $b = 0.2$. This function was chosen so that $W(0) = 0$, $W(b) = 0.5$ and $W(\eta) = 1$.

Transposing the data from the recycling plane grid points to inlet grid points might require interpolation due to a mismatch in grid point location. Lund et al. found a linear interpolation to be sufficiently accurate for use with their second-order scheme.

Similarly, the rescaling operation requires the scaling parameters u_τ and δ to be known both at the recycling station and at the inlet. However, it turns out that the problem is overdetermined if both u_τ and δ are fixed independently at the inlet, therefore an additional compatibility relation is needed to connect one of these parameters at the inflow to the solution at the recycle plane. In the context of zero pressure-gradient turbulent boundary layers, Lund et al. (1998) remarked that although several relations could be used to achieve this goal, they obtained the best results by fixing δ at the inlet and by computing $u_{\tau, \text{infl}}$ using

$$u_{\tau, \text{infl}} = u_{\tau, \text{recy}} \left(\frac{\theta_{\text{recy}}}{\theta_{\text{infl}}} \right)^{\frac{1}{8}}, \quad (4.13)$$

with θ , the momentum thickness.

It should be specified that in the current implementation of the inflow method by Lund et al., the viscous velocity at the inlet was computed slightly differently, as equation (4.13) also requires an estimation of θ_{infl} using empirical formulas. Instead, the friction coefficient at the inlet was first determined using

$$c_{f, \text{infl}} = 0.02 \left(\frac{1}{\text{Re}_{\delta_{\text{infl}}}} \right)^{\frac{1}{6}}, \quad (4.14)$$

which is a power-law curve-fit approximation derived in White (2006, p 433). From there, the viscous velocity at the inlet follows by

$$u_{\tau, \text{infl}} = U_\infty \sqrt{\frac{c_{f, \text{infl}}}{2}}, \quad (4.15)$$

which proved as accurate as the method derived in equation (4.13).

4.2.2 The Recycling and Rescaling Method by Spalart, Strelets, and Travin (2006)

An outer-coordinate rescaling method inspired on that by Spalart et al. (2006) was also implemented, as a simplification to the method by Lund et al. (1998). In this method the inflow velocity field is simply obtained by rescaling the velocity vector at the recycling station such that

$$U_{\text{infl}} \left(0, \frac{y}{\delta_{\text{infl}}}, z, t \right) = U_{\text{recy}} \left(x_{\text{recy}}, \frac{y}{\delta_{\text{recy}}}, z, t \right), \quad (4.16)$$

where δ corresponds to the 99%-thickness of the boundary layer. To determine δ , a spanwise and time average of the recycling plane was computed on the fly.

Contrary to the original implementation by Spalart et al., no shift in z coordinate was used. This choice is justified by the fact that in the simulations under consideration, the recycling planes are located at $400\theta_0$ from the inflow, which is beyond the eddy coherence length determined by Simens et al. (2009) for this type of inflow.

4.2.3 A Small Note on Applying Recycling Methods to LES

In the context of Large-Eddy Simulations, it is important to make sure that the signal provided to the inlet of a computational domain does not contain information at a higher frequency than what the mesh can represent. Failing to do so might lead to an unphysical forcing of the computed solution.

In the case of recycling and rescaling inflow methods, aliasing might occur when rescaling from a thicker boundary layer downstream of the inflow to a thinner boundary layer at the inflow, due to a possible decrease in boundary layer resolution. Whether aliasing can occur would be dependent of the type of grid used, but if its effect appeared to be significant, a low-pass filtering of the inflow information would have to be implemented.

It should be specified that such effects were not investigated in the current study, and that no filtering was applied to the information provided as recycled inflow conditions. This was done because neither the original paper by Lund et al. (1998) nor the paper Simens et al. (2009) explicitly mentioned applying any type of filtering to the recycled flow field they used as inflow condition. Theoretically, as the resolution at the recycling station is twice as high as at the inflow, about 50% of the lower frequencies could be aliased through recycling. However, it could be argued that the high discretization error noticed when using OpenFOAM, combined with the SGS model viscosity, would diffuse the high frequency content out of the flow, decreasing or removing aliasing issues. Unfortunately, due to time constraints, the assumption that filtering was not required has not been verified *a posteriori*, and would have to be done in a follow-up study.

4.3 Precursor Method

The precursor method implemented for the current study used data obtained from a secondary channel flow simulation which was recycled and rescaled according to the method by Lund et al. to provide on inflow condition. The channel flow was driven by a constant pressure gradient $\frac{d\bar{p}}{dx} = 1$, which allowed a few simplifications to the method by Lund et al.

Considering a channel flow of half-width h and length L , and driven by an average pressure gradient $\frac{\partial \bar{p}}{\partial x}$, the mean shear stress will be defined as

$$\tau_w = \mu \left. \frac{\partial \bar{u}}{\partial y} \right|_{y=0},$$

leading to the average force balance in the x direction

$$2h\Delta\bar{p} - 2\tau_w L = 0.$$

This equation simply states that the mean pressure change between $x = 0$ and $x = L$ multiplied by the cross-sectional area counterbalances the mean shear stress on the upper and on the lower wall applied over the domain length. Having a constant pressure gradient, the change in pressure over the domain will be defined as

$$\Delta\bar{p} = -L \frac{\partial \bar{p}}{\partial x},$$

which will lead to

$$\tau_w = -h \frac{\partial \bar{p}}{\partial x}.$$

The friction velocity was defined in equation (2.10) as being

$$u_\tau = \frac{l_\nu}{t_\nu} = \sqrt{\frac{\tau_w}{\rho}}.$$

Then, by simply choosing

$$\begin{aligned} \rho &= 1, \\ h &= 1, \\ -\frac{\partial \bar{p}}{\partial x} &= 1, \end{aligned}$$

the friction term will become

$$\tau_w = 1,$$

leading to a friction velocity

$$u_\tau = 1.$$

Therefore, the viscous velocity is chosen as $u_{\tau, \text{recy}} = 1$. Similarly, the boundary layer thickness at the recycling plane is chosen as the half-channel width, leading to $\delta_{\text{recy}} = 1$.

No special rescaling was developed to account for the non-zero Reynold stresses in the middle of the channel flow, and it is anticipated that will affect the adaptation length and the development of the flat plate boundary layer.

4.4 Random Inflow

A random turbulent inflow was also implemented, to determine whether it could compete with recycled-inflow methods. Although quite elaborate random inflow models have been developed in recent years, a relatively simple method was developed for the current test case. Since in most practical problems, very little information is available *a priori* on the turbulent state of the flow entering the LES domain. This immediately disqualifies the more elaborate random inflow models available, as they are calibrated for very specific flow conditions. The current inflow model is a good example of what can be used in the context of mixed RANS/LES simulation, where the inflow has to be defined using the limited information available from a RANS solver.

The implementation of the current random inflow is inspired from that by Batten et al. (2004), and is based on the construction of a perturbation field using Fourier modes with random phases and amplitudes, and scaled with a tensor scaling based on a Cholesky decomposition of the Reynolds stress tensor. The fluctuation field is computed using

$$v_j(z, t) = \sqrt{\frac{2}{N}} \sum_{n=1}^N p_j^n \cos(2\pi\varphi_j^n z + 2\pi\omega_j^n t + \phi_j^n), \quad (4.17)$$

where φ is the spatial phase, ω the temporal phase, and ϕ a random phase shift.

As LES is considered, care was taken to avoid unwanted physical forcing by adding modes at the inflow beyond what the mesh could represent. A sharp cut-off filter was implemented by choosing the random spatial phases so that the shortest wavelength imposed at the inflow spanned at least 10 cells. The range of the random temporal phase was determined using a Fast Fourier Transform of flat plate data obtained using the method by Lund et al. All variables were

computed using random variables uniformly distributed between $[0, 1]$ and then multiplied by the prescribed range. The inflow velocity field was then assembled with

$$u_i(y, z, t) = U_i(y) + \sum_j a_{ij} v_j(z, t), \quad (4.18)$$

where the amplitude tensor a_{ij} is related to the Reynolds stress tensor through

$$\begin{aligned} a_{11} &= \sqrt{R_{11}}, \\ a_{21} &= R_{21}/a_{11}, \\ a_{22} &= \sqrt{R_{22} - a_{21}^2}, \\ a_{33} &= \sqrt{R_{33}}, \end{aligned} \quad (4.19)$$

and where all a_{ij} elements not listed above were set to zero, and where values for the Reynolds stress were obtained from DNS data. It can be noted that the a_{31} and a_{32} elements of the Cholesky decomposition are missing in the equation above. This is due to the lack of flat plate DNS Reynolds stress information needed for these terms, whereupon it was decided to set them equal to zero. Comparing channel flow DNS Reynolds stress data, for which all the cross-stresses were available, justified this choice, as the R_{31} and R_{32} stresses were found to be 3 orders of magnitude smaller than the other stresses.

4.5 Controlled Forcing Method by Spille-Kohoff and Kaltenbach (2001)

To decrease the adaptation length of the random inflow, the forcing method by Spille-Kohoff and Kaltenbach (2001) was used. Applying their method to the LES computation of turbulent boundary layer on a very short domain using a random inflow with fluctuations based of random Fourier modes with prescribed energy spectrum, the authors claimed an adaptation length of $6 \delta_0$.

The method by Spille-Kohoff and Kaltenbach compares a time-averaged Reynolds shear stress $\langle u'v' \rangle$ at a location x_0 to a target Reynolds shear stress, and applies a forcing term to the normal momentum equation to amplify or damp velocity fluctuations in the wall-normal direction. The force was determined using

$$f(x_0, y, z, t) = r(y, t) [u(x_0, y, z, t) - \langle U \rangle^{z,t}(x_0, y)], \quad (4.20)$$

with the amplitude defined as

$$r(y, t) = \alpha e(y, t) + \beta \int_0^t e(y, t') dt'. \quad (4.21)$$

The error function $e(y, t)$ was computed using

$$e(y, t) = -\rho \langle u'v' \rangle^{z,t}(x_0, y, t) - g(x_0, y), \quad (4.22)$$

where the $\langle \rangle^{z,t}$ exponents denote an average in spanwise direction and in time, and where $g(x_0, y)$ is the target stress.

In the current study, an averaging time window of $T_{avg} = 2\delta/U_\infty$ was used, together with $\alpha = 75$ and $\beta = 0$.

To avoid unrealistically large shear stress events, the forcing term f are only applied if the following conditions are satisfied

$$\begin{aligned} |u'| &< 0.6 U_\infty, \\ |v'| &< 0.4 U_\infty, \\ u'v' &< 0, \\ |u'v'| &> 0.0015 U_\infty^2. \end{aligned} \tag{4.23}$$

Baseline Results and Their Sensitivity

In the context of the current study determining the performance of different type of turbulent inflow conditions, a reference method was sought to give a baseline for comparison in the framework of coarse Large-Eddy Simulation. The recycled type inflows were known *a priori* to be the most accurate for the simulation of turbulent, zero pressure-gradient flat plate boundary-layers, and were therefore chosen as baseline solutions to which the more general precursor and random inflow methods could be compared. The following chapter will evaluate the performance of two recycled inflows developed by Lund et al. (1998) and by Spalart et al. (2006), through a comparison of averaged flow quantities to DNS data.

5.1 Comparison Procedure and Numerical Setup

The following section will introduce the parameters which will be used to compare the recycled-type of inflows by Lund et al. and Spalart et al., as well as the numerical domain and averaging used to sample the computed data.

5.1.1 Comparison Procedure and Parameters

The performance of the inflow method by Lund et al. (1998) and that by Spalart et al. (2006) will be evaluated using coarse incompressible Large-Eddy Simulation (LES) computations of a turbulent flat plate boundary layer, and compared to DNS data by Schlatter and Örlü (2010) and by Simens et al. (2009). To get a feel for how well each method performed, velocity means and Reynolds stress averages were sampled, and compared to the DNS data. From now on, to avoid ambiguity in the plots, the current implementation of the method by Lund et al. will be referred to as “Recycling-I” in plot legends, and the implementation of the method of Spalart et al. will be referred to as “Recycling-II”.

As discussed in the introduction, two specific parameters allowing a straightforward comparison between different inflow conditions will be considered. First of all, the evolution of the shape factor H as a function of Reynolds number Re_θ will be used, as it allows the comparison of two integral properties of a turbulent flow which do not depend on estimates of skin friction. The shape factor was furthermore shown by Chauhan et al. (2009) to be a sensitive indicator of the quality of the boundary layer. The evolution of the skin friction coefficient will be considered independently, as according to Schlatter and Örlü (2010), it allows the indirect monitoring of the local level of turbulent activity within the boundary layer.

For compactness, only the mean and Reynolds stress profiles of the inflow from the method by Lund et al. will be extensively presented, as they showed the best match with DNS. The mean and Reynolds stress plots of the method by Spalart et al. will not be included in this chapter, as it was observed that they did not contribute to more information than what the plots of the shape factor and skin friction coefficient already described.

Using the shape factor and skin friction coefficient evolution, the adaptation length of the inflows by Lund et al. and Spalart et al. will be estimated. As defined in the introduction to this thesis, in this study, the adaptation length will be defined as the domain length needed before the shape factor and skin friction coefficient follow a streamwise evolution similar to that of the DNS results. The longest of the two lengths will then be chosen as adaptation length. Formally, the adaptation length could be defined as the length after which

$$\left. \frac{dH}{dRe_\theta} \right|_{\text{sim}} \approx \left. \frac{dH}{dRe_\theta} \right|_{\text{DNS}},$$

and

$$\left. \frac{dc_f}{dRe_\theta} \right|_{\text{sim}} \approx \left. \frac{dc_f}{dRe_\theta} \right|_{\text{DNS}}.$$

5.1.2 Computational Procedure

LES computations were performed on a $60 \delta_0 \times 4 \delta_0 \times 8 \delta_0$ domain using a second-order finite-volume method. A mean freestream velocity $U_\infty = 20 \text{ m/s}$ and a viscosity $\nu = 0.001937 \text{ m}^2/\text{s}$ were chosen such that a Reynolds number $Re_\theta = 620$ was reached at the inlet, for the chosen initial boundary layer thickness $\delta_0 = 0.5 \text{ m}$. This combination of domain size and flow parameters also ensured that the domain height was at least twice that of the maximum boundary layer thickness in the domain, while capturing at least 5 to 6 low-speed streaks in spanwise direction. The domain was also long enough to ensure that the two lower Reynolds numbers stations from Schlatter and Örlü, $Re_\theta = 670$ and $Re_\theta = 1000$, could be reached, without being too close to the outflow boundary.

The grid used was uniform in all directions, with a resolution of $320 \times 64 \times 64$ cells. Periodic boundary conditions were used in spanwise direction. Neumann boundary conditions were imposed on the outlet and the top of the domain for the velocity, and on the inlet and the outlet for the pressure. A Dirichlet boundary condition was applied for the pressure on the top of the domain.

The extraction plane for the recycling methods was placed at $48 \delta_0$ from the inflow, or $400 \theta_0$, beyond the eddy coherence length determined by Simens et al. (2009).

During the simulations, velocity means and perturbations were sampled and time averaged at planes located at every $2 \delta_0$ in streamwise direction. The mean velocities were first sampled for 5 time units before starting the perturbation sampling, which were sampled for another 35 time units. This is equivalent to the 1400 inertial timescales δ/U_∞ used by Lund et al.

Due to under resolution in the viscous sublayer, the skin friction coefficients, computed using finite difference applied to equation (2.10), were underpredicted by about 10%. This was also observed by Sagaut et al. (2004) and Spyropoulos and Blaisdell (1998). To overcome this underprediction, new friction coefficients were determined using a Clauser chart technique, in which the mean velocity profile is fitted to the logarithmic law of the wall. This fit yields a viscous velocity u_τ , from which a new friction coefficient can be determined. This method is often used in experimental flat plate boundary layer measurements, although there is some debate on the exact values to be used for the law of the wall. Other methods based on velocity profile fitting have also been investigated, but proved cumbersome and less accurate. More details on the Clauser chart technique can be found in Wei et al. (2005).

Readers interested in reproducing the results presented in the current chapter can find the exact solver and domain settings used for the current inflow study in appendix 8.

5.2 A Detailed Analysis of the Results Obtained Using the Inflow by Lund et al. (1998)

In this section, more insight will be given into the quality of the results obtained using the recycling and rescaling method by Lund et al. (1998).

The following plots will show the mean flow averages in streamwise and wall-normal direction and the Reynolds stress averages corresponding to a sampling station were the local averaged Reynolds number is $Re_\theta = 670$. As the sampling planes are located every $2\delta_0$, it is highly probable that such a Reynolds number would be reached between two sampling planes, in which case a linear interpolation between two adjacent planes is applied. For the current inflow case, the Reynolds number $Re_\theta = 670$ was reached at $x/\delta_0 = 3.55$ from the inflow.

The mean velocity in streamwise and wall-normal direction is shown in figure 5.1 and 5.2 respectively, together with the mean profiles from Schlatter and Örlü (2010) at the same Reynolds number. From those figures, it can be seen that the streamwise mean velocity profile is well captured by the grid, even though the mesh resolution near the wall is relatively low. On the other hand, the wall-normal mean velocity profile appears to match the DNS data less accurately, especially close to the wall where numerical oscillations at the grid frequency are observed, and just above the boundary layer where the mean velocity is slight over-estimated.

The cause of the oscillations could not be determined with certainty, and similar oscillations were also observed in streamwise direction, as will be illustrated when comparing integral quantities in later figures. Several stabilizing discretization schemes were tested to try to remedy to this problem, but without success. However, it was observed that the numerical oscillations in wall normal direction decreased when increasing the grid resolution, as illustrated in figure 5.3.

The time and spanwise-averaged Reynolds stresses can be seen in figure 5.4. As can be seen, the $\overline{u'^2}^+$ and $\overline{w'^2}^+$ are slightly overpredicted, with a noticeable peak close to the wall. This peak is attributed to mesh under-resolution close to the wall, as the peaks were shown to decrease with increasing grid resolution. Further analysing figure 5.4 shows that the $\overline{uv'}^+$ stresses are well captured by the mesh, although being very slightly overpredicted in the upper half of the boundary layer. Similarly, the $\overline{v'^2}^+$ show a good match to DNS results, albeit with a small underprediction.

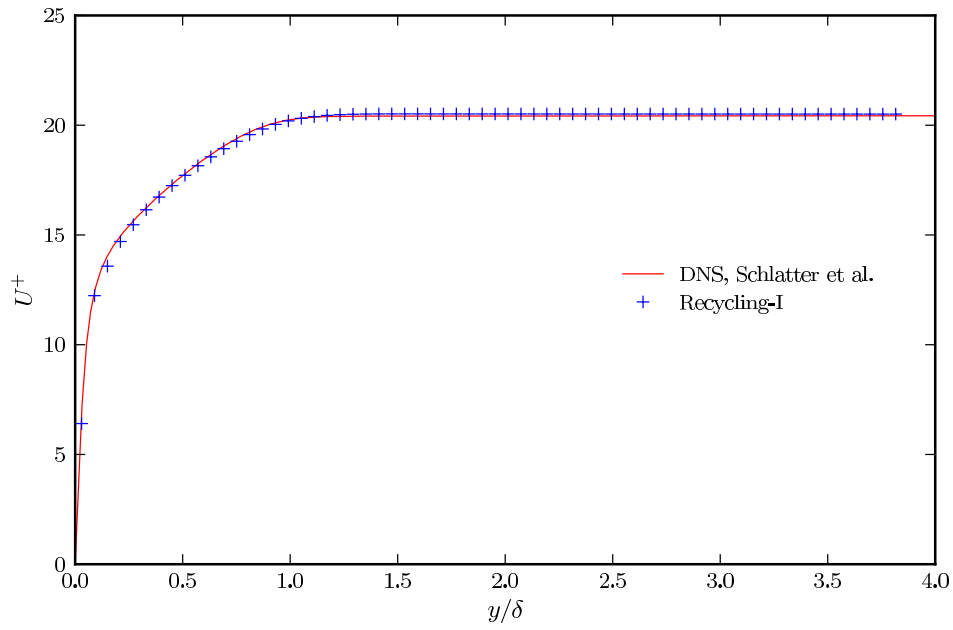


Figure 5.1: U^+ Mean velocity as a function of y/δ

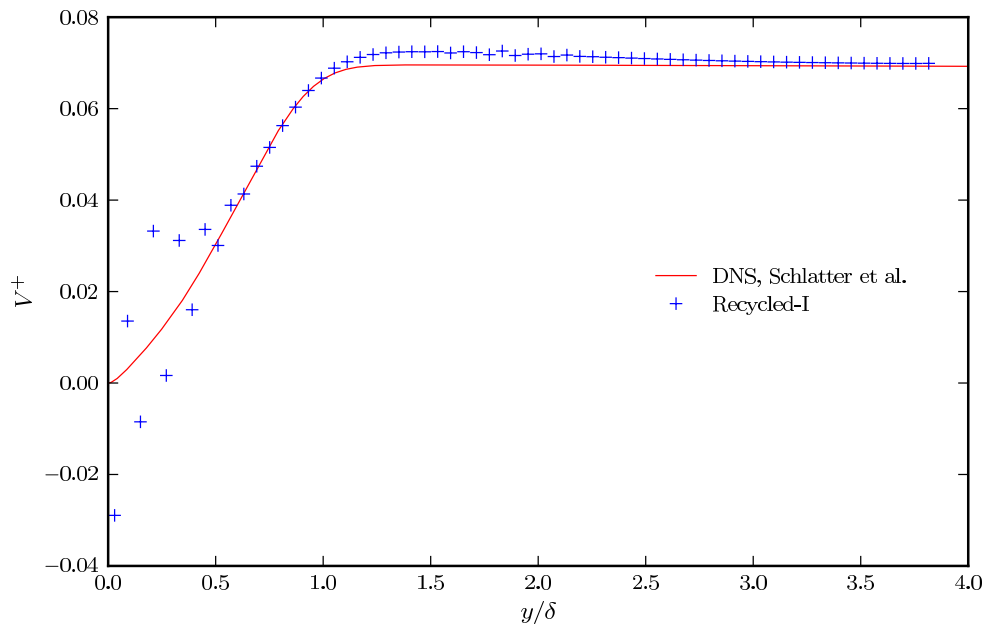


Figure 5.2: V^+ Mean velocity as a function of y/δ

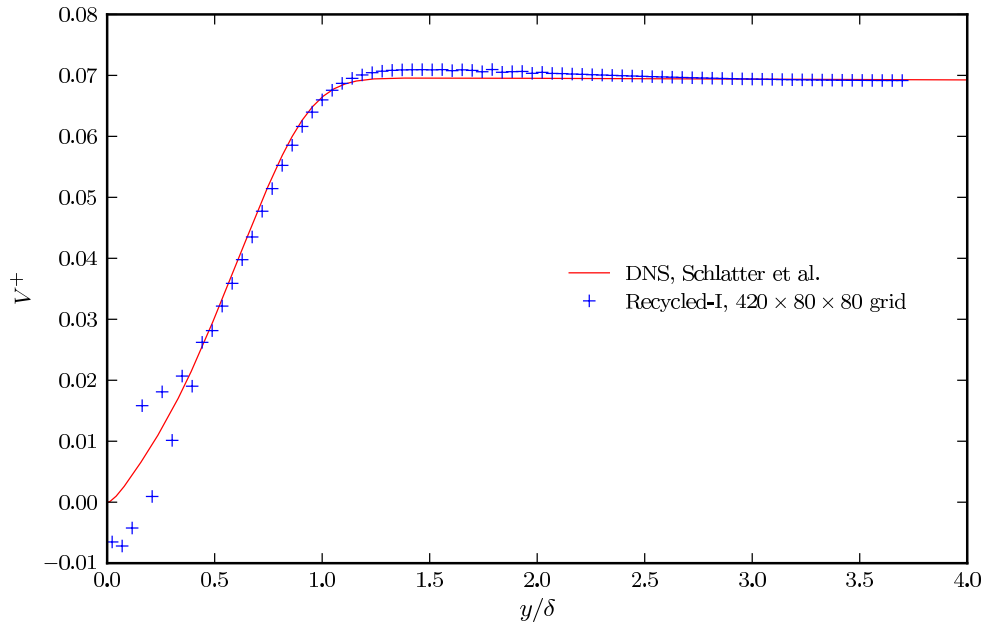


Figure 5.3: V^+ Mean velocity as a function of y/δ , on a $420 \times 80 \times 80$ grid

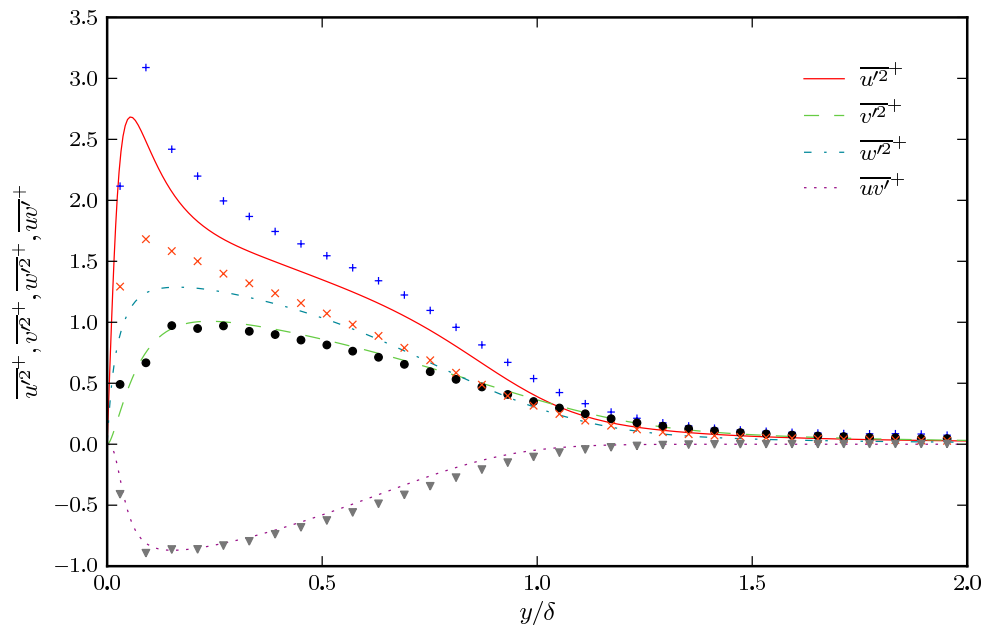


Figure 5.4: Reynolds stresses as a function of y/δ . The lines are from DNS data by Schlatter and Örlü.

5.3 Pressure Gradient and Outer Mean-Velocities

The following subsection will analyse the pressure gradient and the mean velocity components on the top of the computational domain for the simulations made using the inflow procedure by Lund et al. The general idea behind this analysis is to verify that the simulation ran conforms to zero-pressure gradient flow conditions, where the mean velocity in streamwise direction should be constant, and equal to U_∞ , and where the mean velocity in wall-normal direction should follow a certain decay. The pressure gradient and mean quantities were averaged in spanwise direction, and averaged in time over 1400 inertial timescales δ/U_∞ .

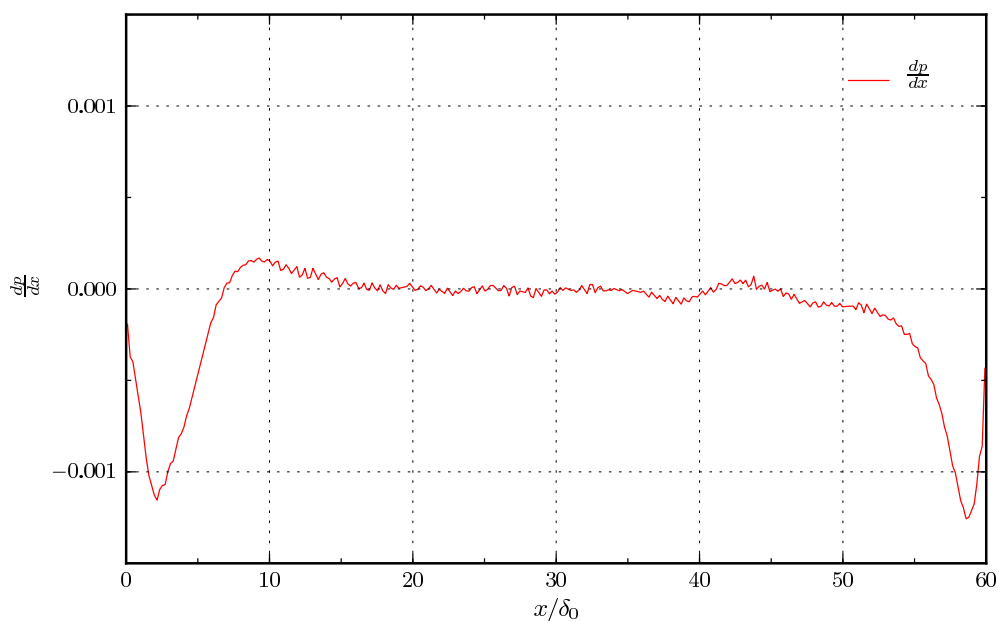


Figure 5.5: Evolution of streamwise pressure gradient $\frac{dp}{dx}$

From the pressure gradient plot shown in figure 5.5, one can notice two pressure gradient drops in the inflow and outflow regions of the computational domain, where the pressure gradient departs from a fluctuating average around zero, to small negative pressure gradient values of around $\frac{dp}{dx} = -0.001$. The pressure gradient change at the inflow of the domain can be linked to the adaptation region of the flow. Interestingly, the pressure gradient seems to stabilize back around zero after a development length of $8\delta_0$, which is the adaptation length Lund et al. (1998) observed when using this type of inflow. The pressure gradient change at the end of the computational domain is caused by an adaptation of the flow to the numerical outflow boundary, of Neumann type, which creates an abrupt truncation of the vortices leaving the domain. It is legitimate at this point to ask oneself in how far a better outflow condition would help increasing the useful length of the computational domain. Using a convective boundary condition, Simens et al. (2009) report losing the last 1.5 exit boundary layer thicknesses of the domain to outflow influences, which is about half the length lost here with a simple Neumann boundary condition. Combined with the fact that the influence of the pressure gradient is probably negligible, the gain seemed minimal, so the Neumann boundary condition on the outflow was kept. Other

solutions tried to decrease the effects of the outflow boundary on the numerical results will be further discussed in section 5.5, when comparing the shape factor and skin friction evolutions.

Figures 5.6 and 5.7 display the evolution in streamwise and wall-normal mean velocity at the top of the computational domain, going downstream. The empirical wall-normal mean velocity evolution shown in figure 5.7 is based on data from an external code for the boundary-layer equations, and is only used to have a qualitative comparison of what the decay in wall-normal velocity should look like.

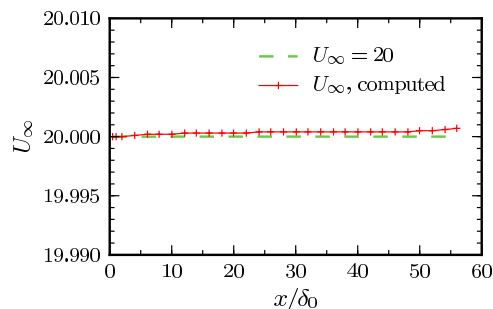


Figure 5.6: Evolution of streamwise mean velocity U_∞

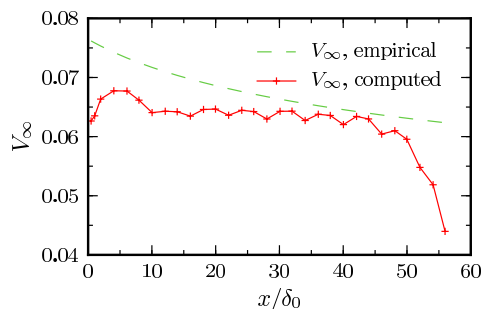


Figure 5.7: Evolution of wall-normal mean velocity V_∞

From figure 5.6, it is clear that the mean velocity U_∞ can be considered constant, a good indication that no significant streamwise acceleration is present in the computational domain. On the other hand, the wall-normal mean velocity evolution, as shown in figure 5.7, is clearly not matching the theoretical evolution. This mismatch highlights one of the most important unsolved challenges encountered when applying Lund's recycling procedure to the computation of a zero pressure-gradient boundary layer. It proved difficult to match both the zero pressure-gradient boundary condition, without flow acceleration in streamwise direction, and the correct wall-normal mean velocity. This is probably due to the proximity of the upper-boundary with the boundary layer being computed, which imposes stringent requirements on the numerical boundary condition to accurately reproduce physical effects which would normally take place beyond the edge of the computational domain. Unfortunately, various attempts at improving on the upper boundary condition, mostly focusing on applying suction on the top of the domain, proved unsuccessful. They either led to numerical instabilities, for example when trying to impose a prescribed V_∞ with a fixed pressure, or proved generally ineffective, as when imposing both U_∞ and V_∞ on the top boundary, while allowing the pressure to change. It was therefore chosen to impose a Dirichlet type boundary condition on the pressure, and a Neumann type boundary condition on velocity for the upper boundary, ensuring the flow did not accelerate in streamwise direction, at the cost of having a mismatch in the mean wall-normal velocity.

It may appear that the mismatch obtained in wall-normal velocity due to the current choice of boundary conditions is trivial, as the wall-normal mean velocity V^+ is 3 orders of magnitude smaller than the mean flow velocity U_∞^+ . However V^+ is thought to have a significant influence on the turbulent solution as it evolves downstream in the domain. This solution discrepancy will be further discussed in the next section.

Another unresolved issue which can be conceptually highlighted by figure 5.7 is that equation (4.10) imposes the exterior mean velocity extracted at the sampling plane as inflow condition, without accounting for streamwise decay in V_∞ . This problem could be simply resolved by scaling the entire mean profile at the inlet until the exterior velocity matches a certain value. However,

no accurate estimation of V_∞ as a function of boundary layer thickness was found, making such a rescaling difficult. Indeed, different models were implemented, and were found to produce more inaccurate results than when just leaving the boundary condition how it originally was.

5.4 Revisiting Means and Reynolds Stresses

A closer look at figures 5.1 to 5.4 would show that the y coordinates are non-dimensionalized by the local boundary layer thickness, yielding so called outer-coordinates. In terms of non-dimensionalization of turbulent boundary layer flows, two straightforward choices are possible. One can either choose to compare data using the inner-coordinates introduced in equation (2.11), which allows to compare small-scale or viscous-related phenomena, or choose to use outer-coordinates, as in the figures above, to compare flow effects influenced by larger scales. The choice of outer-coordinate scaling made here-above is logical in the context of zero pressure-gradient boundary layer computations, due to the form of self-similarity which then emerges for certain flow quantities. It has the disadvantage, however, of masking slight mismatches appearing as the flows evolves going downstream. The switch will now be made to inner-coordinates to discuss the mismatches in question.

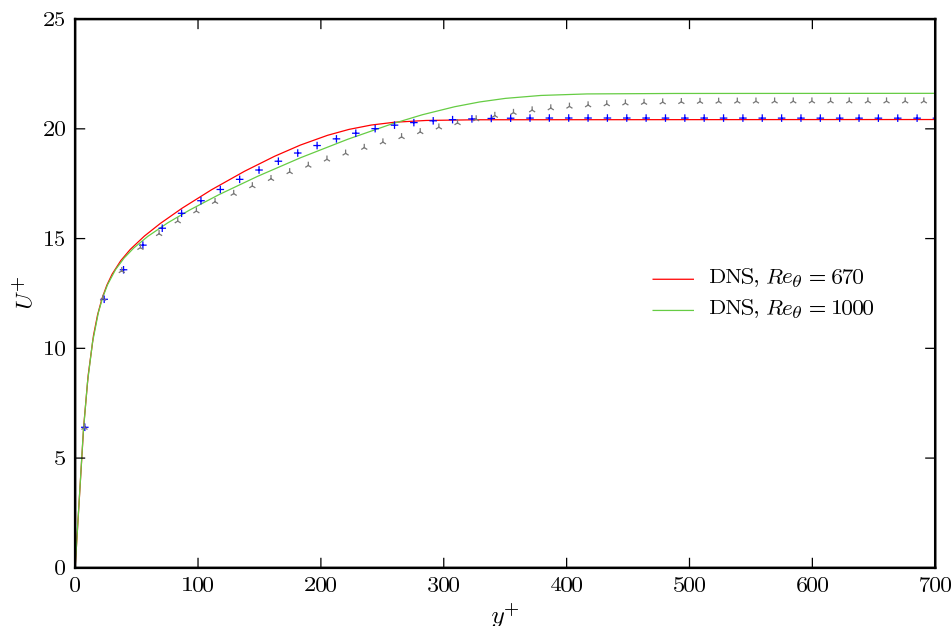


Figure 5.8: Mean streamwise velocity at two sampling stations $Re_\theta = 670$ and $Re_\theta = 1000$, in y^+ coordinates

Comparing the $Re_\theta = 670$ averages in figures 5.8 and 5.1, it can be seen that although the mean profile seems like a very good match with DNS in y/δ coordinates, the same profile in y^+ coordinates suffers from a slight velocity defect in the upper part of the boundary layer. It would be legitimate to think that the mismatch is only due to an error made in estimating the viscous velocity u_τ with the Clauser plot technique, but the non-dimensional U^+ mean velocity shows a

very good intercept of the DNS data in the freestream part of the flow, proving the right viscous velocity was estimated. This indicates that the mismatch observed is due to a mismatch in the flow properties.

Shifting to the $Re_\theta = 1000$ data in y^+ coordinates, it can be seen that the velocity defect on the top part of the boundary layer is much more pronounced. This time, the intercept of the non-dimensional mean velocity U^+ in the freestream region shows that viscous velocity u_τ was slightly overpredicted, which will also affect the y^+ coordinate scaling. Nonetheless, the slight overprediction in u_τ is not sufficient to explain the large velocity defect observed in the upper part of the boundary layer, between $y^+ = 150$ and $y^+ = 400$. Such a defect is a clear indication that the solution is diverging from DNS results going downstream.

This divergence effect can also be found in the Reynolds stresses, as shown in figure 5.9. Once more, the match at $Re_\theta = 670$ is excellent, and comparable to the Reynolds stress $\overline{v'^2}^+$ match in figure 5.4. And identically, an important mismatch can be seen at $Re_\theta = 1000$ in the upper part of the boundary layer. Similar mismatches were noticed in all the Reynolds stresses.

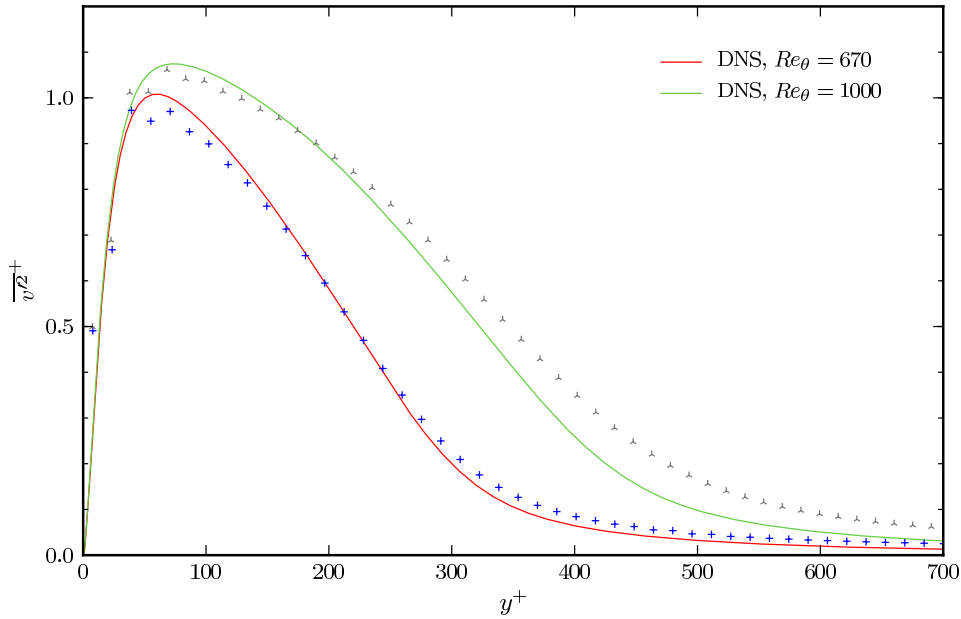


Figure 5.9: $\overline{v'^2}^+$ at two sampling stations $Re_\theta = 670$ and $Re_\theta = 1000$, in y^+ coordinates

From both figures presented in this section can be observed that the computed solution diverges from DNS results going downstream. As the match with DNS at the sampling station of $Re_\theta = 670$ is excellent, it can be concluded that the mismatch is not a result of inflow modeling errors. The differences can also not be attributed to under-resolution, as, once more, the upstream results were a good match to DNS, and because the relative resolution in the boundary increases going downstream. It was therefore concluded that the solution divergence observed was probably caused by the influence of the artificial top boundary condition, which was not defined accurately enough to supply a physical wall-normal mean to the domain going downstream. Such an effect would become more important as the ratio between domain height

and by boundary layer thickness decreases as the solution evolves downstream. This can be illustrated by the plot of the wall-normal mean velocity from the sample station at $Re_\theta = 1000$, shown in figure 5.10, where the non-dimensional wall-normal mean velocity was shown to be overpredicted. This observation, combined with an overprediction in u_τ at higher Reynolds number, implies that the dimensional wall-normal mean velocity is at least 10% larger than what it should be to accurately simulate a flat plate flow.

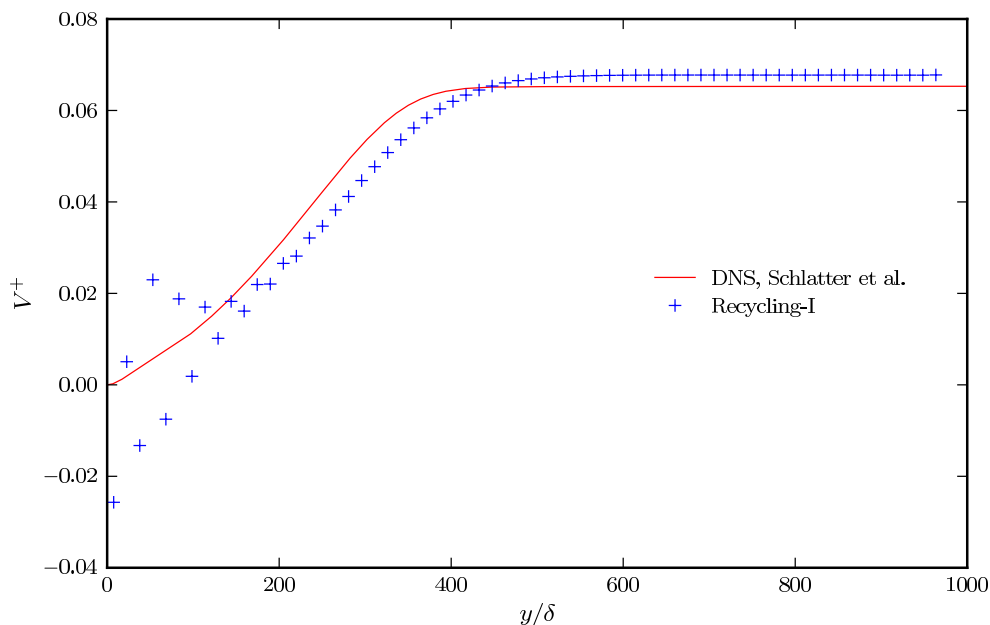


Figure 5.10: V^+ Mean velocity as a function of y/δ

To try to substantiate this conclusion that the mismatch observed is due to the influence of the top boundary condition, a new simulation was run on a domain twice as high as the baseline domain, keeping the same grid stretching. Such a domain should have had the effect of decreasing the influence of a poorly defined top boundary condition on the computed solution. Unfortunately, the results obtained could not support the postulate claim that the mismatches were due to the top artificial boundary condition, as the mismatch with DNS was only increased at $Re_\theta = 1000$ compared to the solution on the baseline domain. In fact, the wall-normal mean on the top part of the boundary was found to be worse than that on the baseline domain, as illustrated in figure 5.11. Since a placing of the outer-boundary far enough away should eliminate this source of error, this result indicates that the solution is still quite sensitive to the approximations on the upper artificial boundary.

Thus, it is believed that an artificial boundary condition representing a more physical condition for the top of the current computational domain will largely remedy to the solution mismatches observed in this section. It is unfortunate that the attempts at implementing such a boundary condition were unsuccessful, as mentioned in section 5.3.

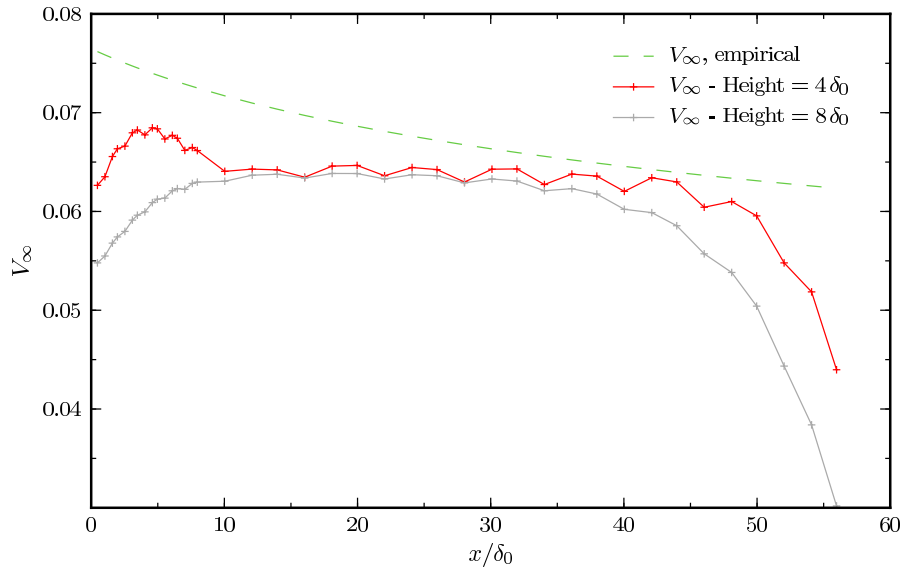


Figure 5.11: Evolution of wall-normal mean velocity V_∞ for two domains of different height

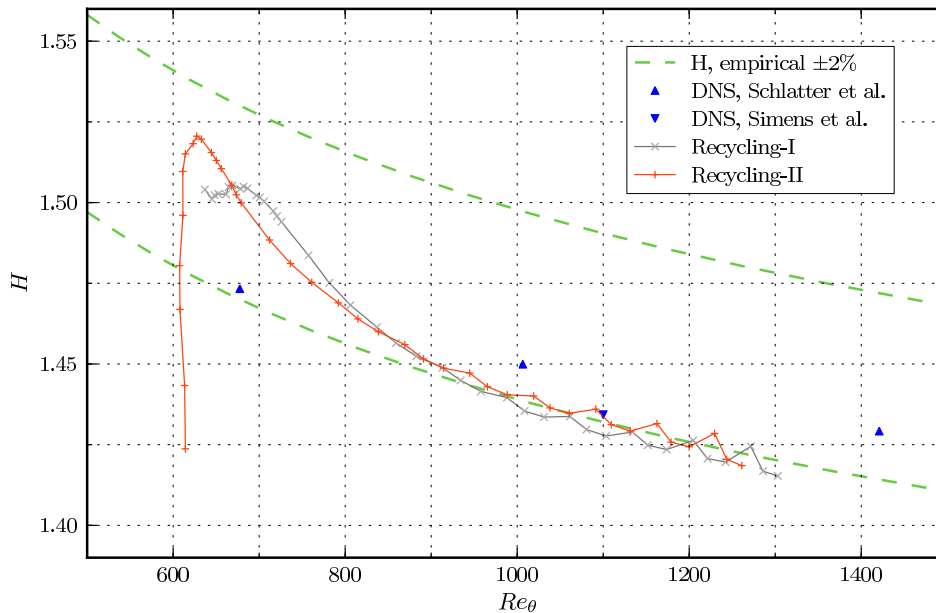
5.5 Adaptation Lengths

Using the shape factor and skin friction coefficient evolution, the adaptation length of the inflows by Lund et al. and Spalart et al. will be estimated. The comparison procedure outlined in subsection 5.1.1 will be used.

Figures 5.12 and 5.13 show the evolution of shape factor $H = \delta^*/\theta$ and skin friction coefficient $c_f = 2(u_\tau/U_\infty)^2$ as a function of Re_θ . Figure 5.12 also includes an empirical shape factor fit, based on experimental data, and taken from Monkewitz et al. (2007), together with DNS data points from Schlatter and Örlü (2010) and Simens et al. (2009). It is important to underline that this empirical formula was derived using medium to high Reynolds number experiments, and therefore solely serves as a qualitative approximation of the shape factor evolution. The empirical fit was plotted with a $\pm 2\%$ tolerance. Similarly, figure 5.13 plots the recomputed friction coefficients estimated using the Clauser plot technique, together with DNS data points, and with an empirical friction coefficient fit by Smits et al. (1983). This fit, based on a power law, estimates the friction coefficient as $c_f = 0.024 Re_\theta^{-1/4}$, and is plotted in figure 5.13 with a $\pm 5\%$ tolerance. It was shown by Schlatter and Örlü to be a surprisingly accurate fit to low Reynolds-number DNS friction coefficients.

Although both shape factors show a very different evolution in the first 100 Re_θ of the computational domain, they tend to following a similar evolution after around $Re_\theta = 860$, and arguably also the same evolution as DNS from the same point onwards. This corresponds to an adaptation length of $x/\delta_0 = 18$ for the method by Lund et al. and an adaptation length of $x/\delta_0 = 22$ for the method by Spalart et al., base on shape factor.

Turning to figure 5.13, a much smoother and comparable evolution of the friction coefficient


 Figure 5.12: Shape factor evolution as a function of Re_θ

as a function of Reynolds number is shown for both inflow methods. A clear jump in skin friction can be observed at around $Re_\theta = 700$ for the method by Lund et al., after which it arguably more or less follows the DNS evolution. A closer inspection of the data averages places the jump at $x/\delta_0 = 6.5$. The skin friction of the method by Spalart et al. also show a clear inflection point at $Re_\theta = 670$, after which it follows an evolution similar to the method by Lund et al. The Reynolds number at the inflection point corresponds to an adaptation length $x/\delta_0 = 8$. Contrary to the shape factor adaptation lengths, the adaptation lengths determined from the skin friction are comparable to that determined by the authors of the original inflow methods.

It should be noted that both figure 5.12 and 5.13 show oscillations in their value at higher Reynolds numbers, going downstream. This is caused by the influence of the numerical outflow, of Neumann type, which creates an abrupt truncation of the vortices leaving the domain. To try to remedy to this problem, both an advective and a convective type of outflow boundary conditions were tested, and proved effective in reducing the oscillations at the outlet, at the cost of creating oscillations at the inlet. The original Neumann boundary condition was therefore kept.

5.6 A Summary of the Sensitivity of the Results to the Domain and Grid

From the baseline $60\delta_0 \times 4\delta_0 \times 8\delta_0$ domain with uniform $320 \times 64 \times 64$ mesh, several different domains were tested:

- A $60\delta_0 \times 4\delta_0 \times 16\delta_0$ domain with uniform $320 \times 64 \times 128$ mesh, doubling the domain width

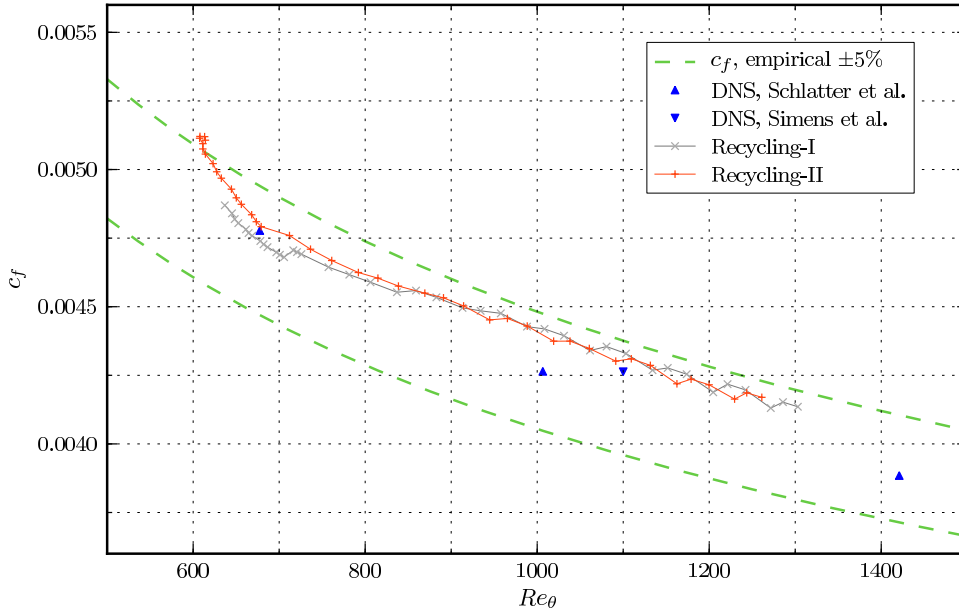


Figure 5.13: Skin friction coefficient evolution as a function of Re_θ

while keeping the grid spacing constant, to test whether the domain was large enough. No changes were noticed in mean velocities, Reynolds stresses, shape factor or skin friction coefficient evolution.

- A $60 \delta_0 \times 84 \delta_0 \times 8 \delta_0$ domain with uniform $320 \times 128 \times 64$ mesh, doubling the domain height and keeping the grid spacing constant, to test what the effect of increasing the distance between the upper-boundary and the solution would be. Although it was expected that the results would improve, it was found that the mean velocity averages and Reynolds stresses were actually slightly worse than those obtained on the baseline domain.
- A $60 \delta_0 \times 4 \delta_0 \times 8 \delta_0$ domain with uniform $400 \times 80 \times 80$ mesh, keeping the domain constant while uniformly increasing the grid resolution. It was found that the $\overline{u'^2}^+$ and $\overline{w'^2}^+$ were a slightly better match to DNS than the baseline domain, mainly through a small decrease of their overprediction near the wall. The mean velocities and other Reynolds stress were found to be only marginally more accurate. It was noticed, however, that the shape factor curve was shifted upward, and was more accurately following the DNS results. Similarly, the skin friction coefficient curve was shifted downwards, closer to the DNS results. To illustrate those effects, a plot of the $\overline{u'^2}^+$ stress and shape factor evolution are shown in figures 5.14 and 5.15.
- A $60 \delta_0 \times 4 \delta_0 \times 8 \delta_0$ domain with a very lightly stretched $320 \times 64 \times 64$ mesh, to assess the effect of grid stretching on the solution. The grid stretching was hyperbolic, chosen such that the largest cell on top of the domain was twice the size of the small cell next to wall. The results were unexpected, as all quantities were a much worse match to DNS than the baseline domain. The wall-normal mean velocity V was largely underpredicted, and a

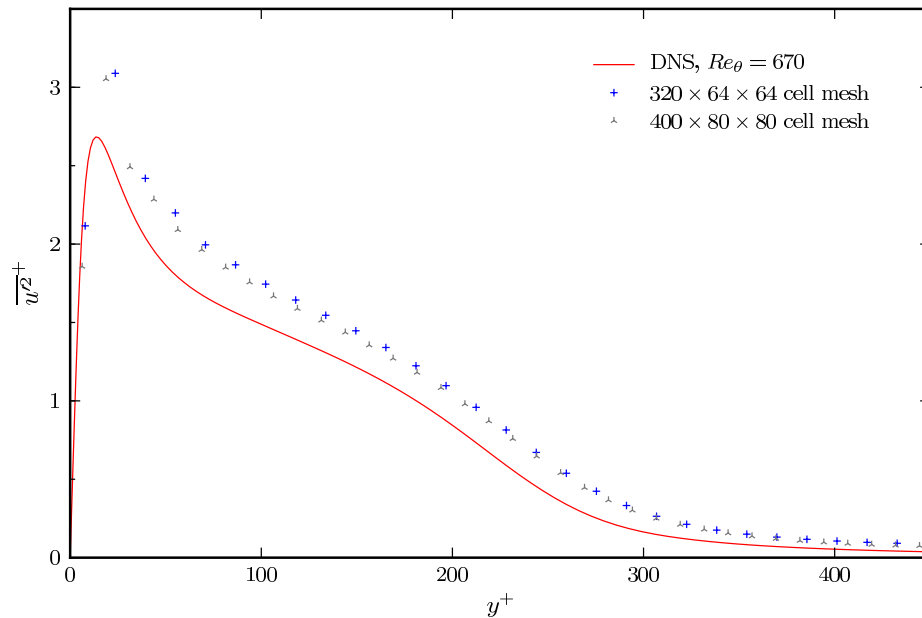


Figure 5.14: $\overline{u'^2}^+$ stress on two domains with different uniform mesh resolution

velocity defect appeared in the streamwise mean velocity. Similarly, the Reynolds stresses were underpredicted and more smeared out in wall-normal direction, a good indication of numerical diffusion. To illustrate those effects, a plot of the wall-normal mean velocity and skin-friction coefficient evolution are shown in figures 5.16 and 5.17.

- Finally, a $60 \delta_0 \times 4 \delta_0 \times 8 \delta_0$ domain was used, and three test cases were compared with either a doubling of resolution in wall-normal, or in streamwise, or in spanwise direction, keeping the grid uniform. This was done to assess the sensitivity of the solution to cell aspect-ratio. The results were once more unexpected, with variations up to 20% in Reynolds stresses, and again, a noticeable smearing-out in wall-normal direction. This effect is illustrated for the $\overline{w'^2}^+$ Reynold stress in figure 5.18, for a sampling station at $Re_\theta = 1000$.

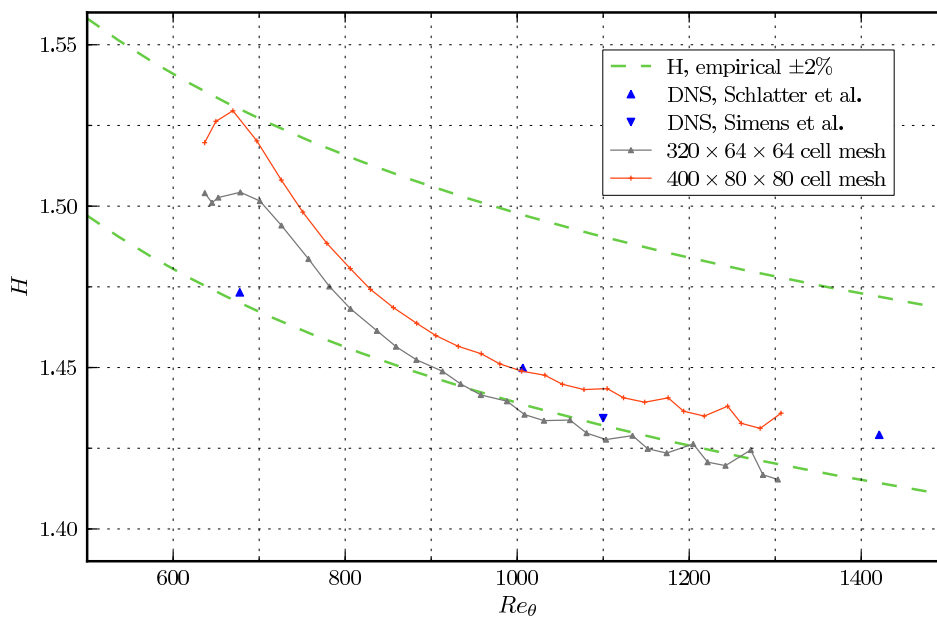


Figure 5.15: Shape factor evolution on two domains with different uniform mesh resolution

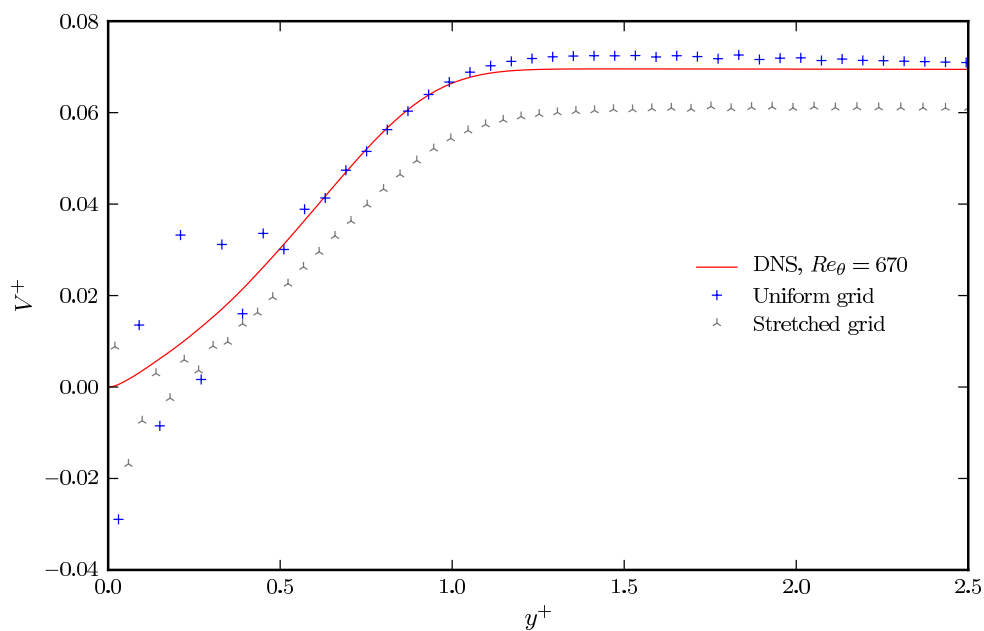


Figure 5.16: Wall-normal mean velocity, without and with grid stretching

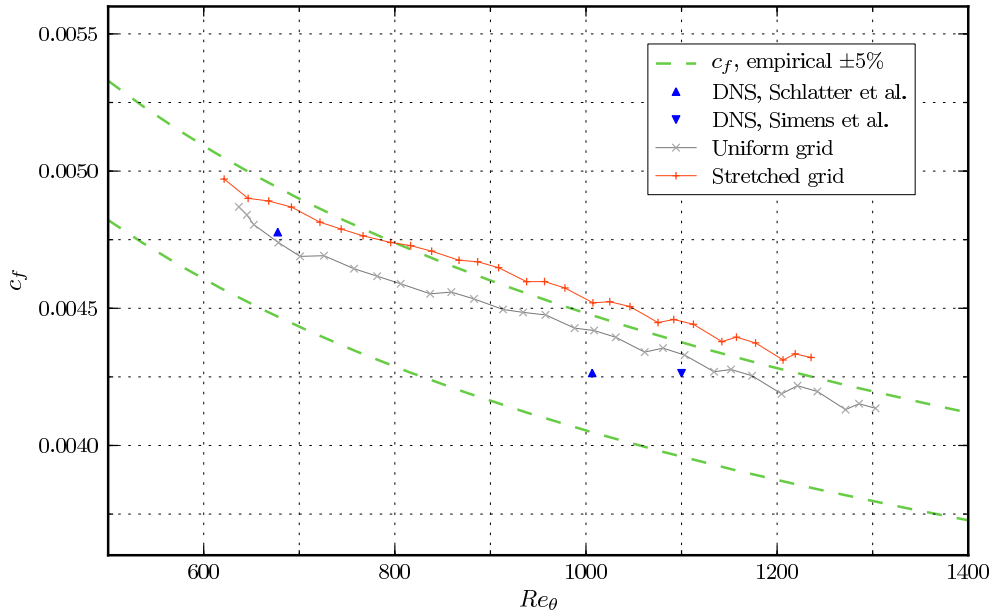


Figure 5.17: Shape factor evolution on two domains, without and with grid stretching

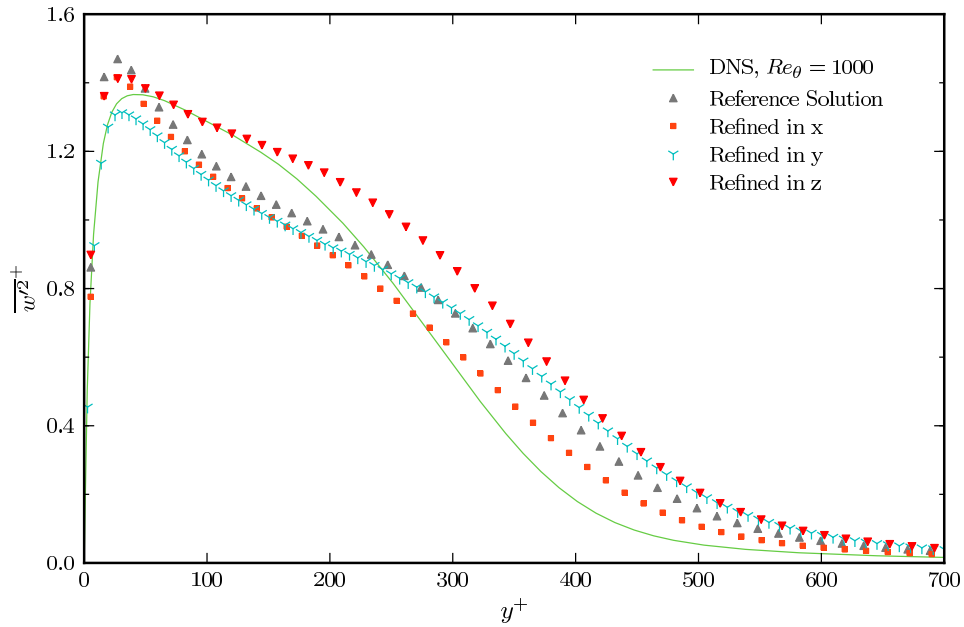


Figure 5.18: Sensitivity to cell aspect ratio

5.7 Placement of the Recycling Plane

In this section, the effect of placing the recycling planes at the alternate locations used by the original researchers will be presented. In their original flat plate computations, Lund et al. (1998) placed their recycling plane at $x = 8 \delta_0$, while Spalart et al. (2006) placed their recycling plane at $x = 5 \delta_0$. As the means and Reynolds stresses were very similar to those already presented in this chapter, they will not be reproduced here, for compactness. The shape factor and skin friction evolution, did, however, show different evolutions to those shown in the previous section. They can be seen in figures 5.19 and 5.20 respectively.

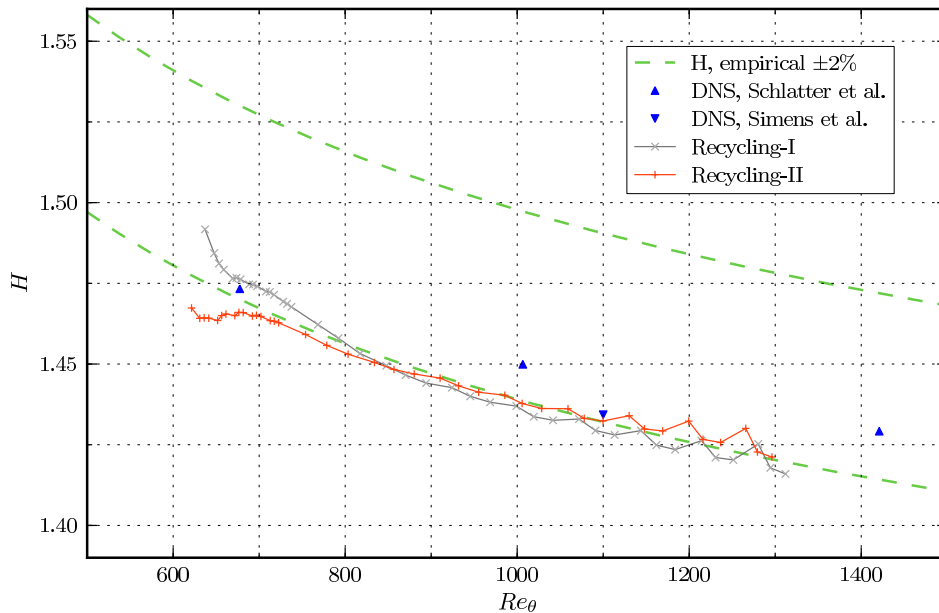
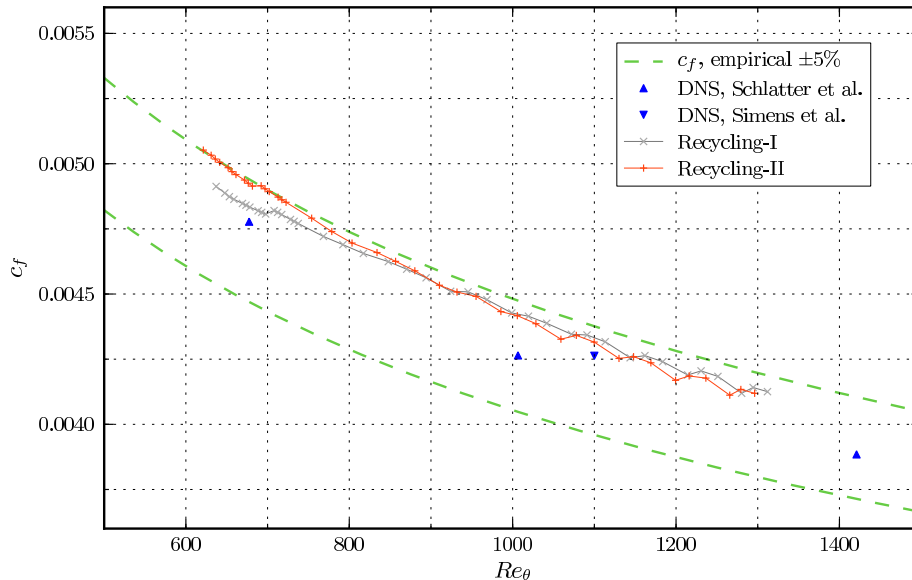


Figure 5.19: Shape factor evolution as a function of Re_θ

As can be seen from the shape factor plot, both shape factor are now much flatter, and follow the evolution of the DNS shape factor much more closely. Therefore, both adaptation lengths are much shorter. The method by Spalart et al. follows the DNS evolution from $Re_\theta = 700$ onwards, corresponding to an adaptation length $x/\delta_0 = 6$. Similarly, the method by Lund et al. follows DNS evolution from $Re_\theta = 800$ onwards, yielding an adaptation length $x/\delta_0 = 12$.

The plots of the skin friction coefficient evolution, although being straighter than their counterparts of the previous section, show very similar adaptation lengths, so will new adaptation lengths will not be re-estimated here.

The interesting observation brought by the plots in this section is that placing the recycling plane close to the inflow, in the part most susceptible to creating high correlation in the flow, seems to produce a more usable solution, due to the shorter adaptation lengths, and more “physical” shape factor and skin friction evolution. However, such observations are more likely to be created by fortuitous mutually canceling effects. In fact, Simens et al. (2009) warn that placing the recycling plane in the first $x/\theta_0 = 60$ would create artificial periodicity in the flow, which can be detected even in instantaneous velocity maps. As the recycling plane for the method

Figure 5.20: Skin friction evolution as a function of Re_θ

by Spalart et al. was placed at $x/\theta_0 = 40$ in the current case being discussed, such effects should be expected. It cannot be stressed enough that solution periodicity should be avoided at all costs, since it will lead to unphysical forcing of the solution, and unphysical results. Simens et al. determined that the eddies in the current type of flows would probably stay coherent for 200 to 300 θ_0 , which implies that recycling plane should be put beyond this coherence region.

5.8 On The Need Of Determining The Correlation Length

The observations made at the end of the previous section motivate the need for a proper correlation length determination when using the recycling and rescaling type of inflows, to ensure the recycling plane is placed beyond the correlation length of the inflow to avoid unphysical forcing and artificial periodicity. The capability of such inflows to create highly periodic flows should not be underestimated. Nikitin (2007) showed that a periodicity with less than 1% deviation could be maintained for more than 70 pipe radii when rescaling information from a periodic domain to a pipe flow.

Unfortunately, no convincing correlation length determination was obtained for the current inflow study due to a lack of time. Early correlation plots of unfiltered data proved inconclusive. Therefore, a proper correlation length determination would have to be done to confirm that the recycling plane was, indeed, put beyond the coherence length of the inflow. Very detailed guidelines for such a study are outlined in the paper by Simens et al. (2009), and extra information on coherence in turbulent flows can be found in Marusic and Heuer (2007). It should be mentioned that such a study is not a trivial one to do, and, that when doing such as study, one should not forget that the eddies in the flow correlate with local y/δ , as this is often overlooked when determining correlation lengths of spatially evolving boundary layers.

Inflow Generation Comparison

In this section, the more general precursor, random inflow and random forced methods will be compared to the baseline results obtained with recycling. Specifically, the following types of inflows will be considered: an inflow using the recycling and rescaling method by Lund et al., an inflow using the outer-coordinate recycling method by Spalart et al., a precursor-like method using channel-flow data rescaled according to the method by Lund et al., a random inflow method using the approach described in chapter 4.4, and a random inflow method using the approach described in chapter 4.4 augmented with the forcing plane method by Spille-Kohoff and Kaltenbach.

6.1 Inflow Comparison and Numerical Setup

The comparison procedure to assess the performance of the various inflows is similar to that outlined in subsection 5.1.1 for the baseline study, and will not be repeated here. It should be mentioned that only the shape factor and skin friction coefficient evolution plots will now be used as comparison tools.

The same numerical setup was used for all test cases, and is identical to that described in subsection 5.1.2. Some extra parameters will be added here for completeness. The channel flow simulation for the precursor method was run with a 64^3 mesh on a $12\delta_0 \times 4\delta_0 \times 8\delta_0$ domain, with the same viscosity $\nu = 0.001937\text{ m}^2/\text{s}$, ensuring the grid resolution was identical to that of the flat plate, at similar physical flow conditions. Periodic boundary conditions were used in spanwise and streamwise direction, and the flow was driven by a source term $dp/dx = 1$, added to the Navier-Stokes equations.

When running the forcing method by Spille-Kohoff and Kaltenbach (2001), 4 forcing planes were used at locations $x/\delta_0 = 0.6, 1.3, 2.6$ and 5.2 , with an averaging window of $T_{\text{avg}} = 2\delta/U_\infty$, together with weight factors $\alpha = 75$ and $\beta = 0$.

Readers interested in reproducing the results presented in the current chapter can find the exact solver and domain settings used for the current inflow study in appendix 8.

6.2 Results

Figures 6.1 and 6.2 show the evolution of shape factor $H = \delta^*/\theta$ and skin friction coefficient $c_f = 2(u_\tau/U_\infty)^2$ as a function of Re_θ , with the first sampling points located at a distance $x/\delta_0 = 2$ from the inflow. Both figures also include the empirical shape factor and skin coefficient fits described in section 5.5.

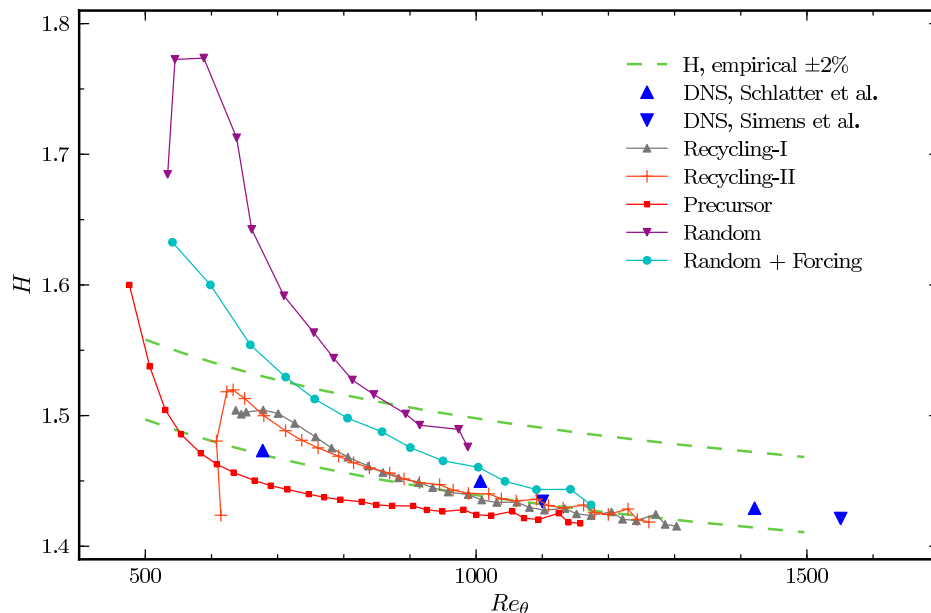


Figure 6.1: Shape factor H evolution as a function of Re_θ

As presented in chapter 5, the recycling method of Lund et al. and that by Spalart et al. show very similar shape factor evolution in figure 6.1, although the Reynolds number at the first sampling station of the recycling method of Spalart appears to be slightly lower than the expected value of $Re_\theta = 620$. Nonetheless, both methods show a reliable shape factor growth. The effect of the forcing method by Spille-Kohoff and Kaltenbach on the random inflow is also clearly visible. Compared to the inflow without forcing, the random inflow with forcing planes displays a much more realistic evolution of the shape factor. Interestingly, despite underpredicting the absolute shape factor when compared to the recycling method by Lund et al., the precursor method seems to result in a shape factor following the correct growth trend.

Similar trends can be observed in the evolution of the skin friction, as shown in figure 6.2. The recycling methods by Lund et al. and Spalart et al. produce very similar results, although it can be argued that recycling method by Spalart et al. needs a slightly longer adaptation length before following the same evolution trend as the recycling method by Lund et al. For the random inflow, once again, the effects of the forcing planes are substantial, that with forcing planes having

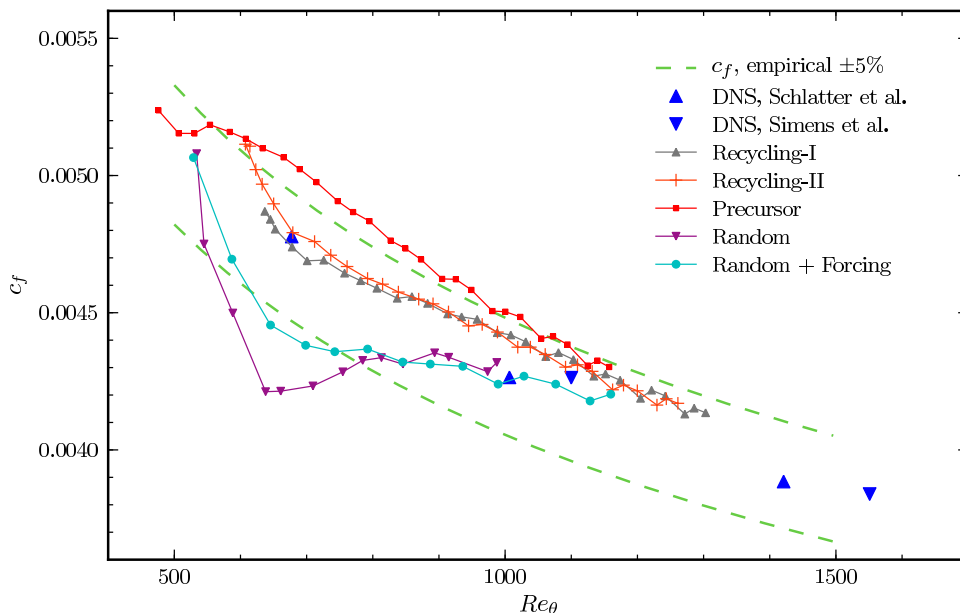


Figure 6.2: Friction coefficient c_f as a function of Re_θ

a more realistic skin friction evolution than the unforced random inflow. It is interesting to notice that after adaptation, the skin-friction coefficient evolution of the random inflow with forcing is almost parallel to that of the recycling type of inflows. And finally, the precursor method correctly simulates a decreasing skin friction as a function of increasing Reynolds number, albeit with an over-estimation of the skin-friction.

From figures 6.1 and 6.2, a qualitative adaptation length can be determined, following the definition introduced in subsection 5.1.1. The adaptation lengths of the recycling inflow methods by Lund et al. and Spalart et al. were previously determined in chapter 5 to be equal to $x/\delta_0 = 18$ and $x/\delta_0 = 22$ respectively.

From the shape factor plot of the random inflow, no true adaptation length can be determined, as with the current domain length no part of the evolution reaches a point where it follows shape factor evolution of DNS. From the current evolution, it could be expected, however, that the random inflow would converge towards DNS evolution, given enough adaptation length. Switching to the random inflow with forcing, it can be argued that its shape factor evolution follows DNS from $Re_\theta = 900$ onwards, corresponding to an adaptation length of $x/\delta_0 = 30$. The shape factor evolution of the precursor method shows a similar evolution to DNS relatively rapidly, at around $Re_\theta = 700$. This corresponds to an adaptation length of $x/\delta_0 = 18$, which is similar to the adaptation length determined for the method by Lund et al. (1998), based on shape factor.

When analysing the skin friction coefficient evolutions, it is once more difficult to determine an adaptation length for the purely random inflow, as it does not yet follow the DNS evolution. The random inflow with forcing planes, on the contrary, rapidly shows a stable evolution, from $Re_\theta = 600$ onwards. This corresponds to an adaptation length of $x/\delta_0 = 8$. The adaptation length of the precursor method is also slightly difficult to determine as it does not follow a

slightly curved decay which a correct evolution should have. However, the evolution of the skin friction seems to follow a smooth trend from $Re_\theta = 550$ onwards, which would correspond to an adaptation length of $x/\delta_0 = 8$.

Choosing the longest of the two adaptation lengths for every test case, it can be determined that the precursor method has the shortest adaptation length, on par with that from Lund et al., at $x/\delta_0 = 18$, followed by the random inflow with forcing which has an adaptation length of $x/\delta_0 = 30$.

It is interesting to notice that, although the shape factor of the random inflow with forcing planes needed a relatively long adaptation length, the skin friction coefficient followed a physical evolution relatively rapidly, especially when compared to the purely random inflow.

6.2.1 Turbulence Evolution

In this section, a qualitative comparison of turbulence evolution within the computational domain will be made, by visualising planes of instantaneous velocity magnitude extracted at different streamwise locations. 4 planes were extracted per domain, at locations $x/\delta_0 = 0, 10, 20$ and 30 . The results from the method by Spalart et al. (2006) are omitted here, as they were similar to the method by Lund et al. (1998).

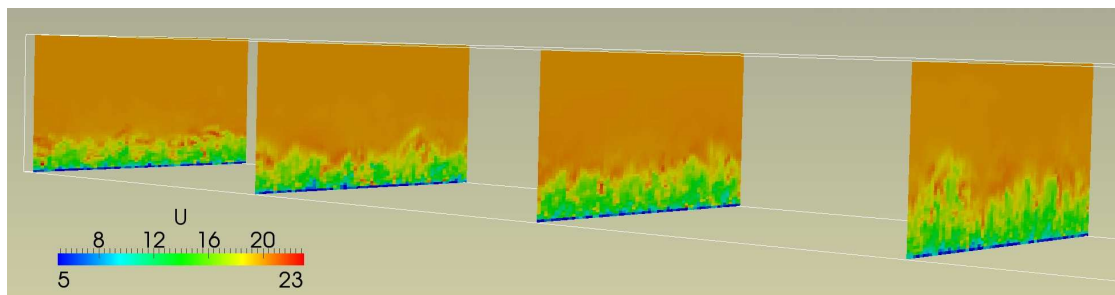


Figure 6.3: Streamwise turbulence evolution, Lund et al.

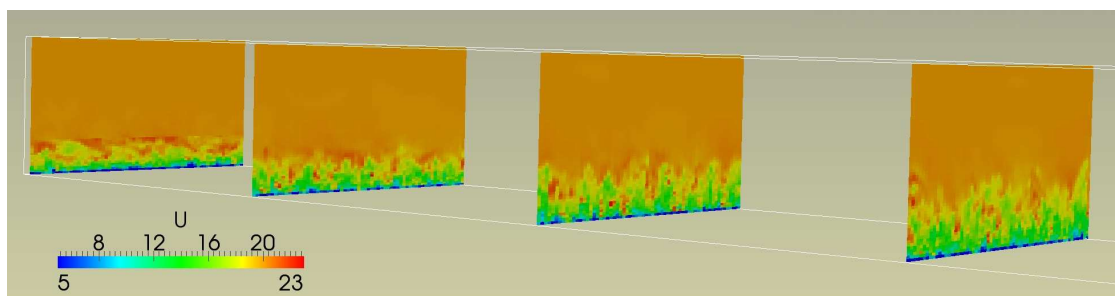


Figure 6.4: Streamwise turbulence evolution, precursor-like method

Comparing the precursor-like method to the baseline inflow by Lund et al., one can unmistakably recognize the truncation of the channel-flow boundary layer in figure 6.4, at $y = \delta_0$. Clearly, the structure of the channel-flow boundary layer is different to that from the flat-plate, as the perturbations do not, on average, decrease back to zero towards the boundary-layer edge.

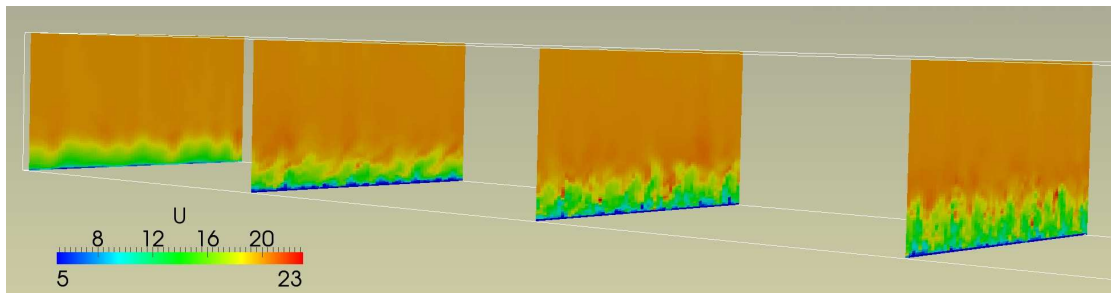


Figure 6.5: Streamwise turbulence evolution, random inflow without forcing planes

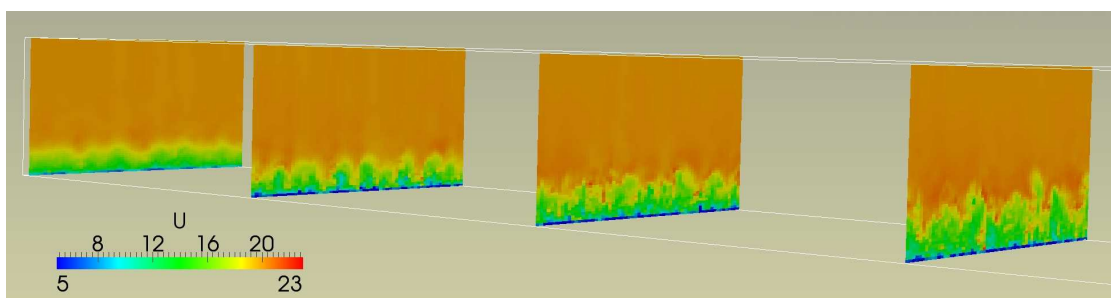


Figure 6.6: Streamwise turbulence evolution, random inflow with forcing planes

This explains the extensive patches of high velocity, in red, in the upper part of the boundary-layer. Nonetheless, the turbulence seems to be similar in chaotic content and intensity variation as that from the baseline solution. This illustrates once more the quality and usability of the precursor-like inflow method.

Evaluating the streamwise evolution of the random-inflow method without forcing planes, show in figure 6.5, one can see that the frequency limit imposed on the method may have been slightly conservative, as little “chaos” is observable at the inflow compared to the baseline inflow. Nonetheless, the turbulence seems to adapt reasonably quickly, as the chaotic content in the third plane already seems quite physical. A slight sideways bias can be observed in the second plane, which is due to the random inflow implementation. This bias was observed in every run of the random inflow, and might be due to the solver trying to impose a divergence-free condition on in the inlet.

The effect of the forcing planes on the random-inflow method case are also apparent, as can be seen in figure 6.6. The sideways bias has been removed, to be replaced by a more chaotic and turbulence-like boundary layer. It should be noted that there are few differences visible visually between the two random inflows in the last two planes.

Comparing both random inflows to the baseline inflow by Lund et al., it seems that in the last two planes of the random inflow methods the turbulence does not quite approach the chaotic intensity that can be seen in baseline results. This might be remedied by including higher frequency content at the inflow.

To further illustrate the differences between the various inflows, their Reynolds stresses at a specific downstream extraction plane are also plotted. The plane location chosen was at $x/\delta_0 = 16$, corresponding to the inflection point in skin-friction coefficient evolution of the random inflow. In figure 6.2, this corresponds to the point at $Re_\theta = 630$. The Reynolds stresses

can be seen in figures 6.7 to 6.10.

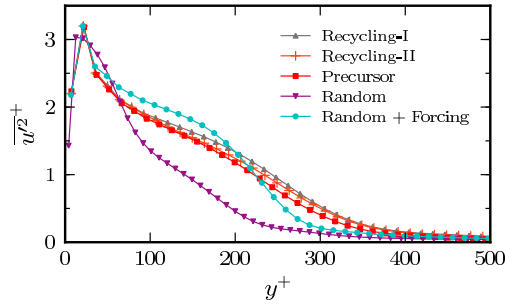


Figure 6.7: $\overline{u'^2}^+$ Reynolds stresses, at $x/\delta_0 = 16$

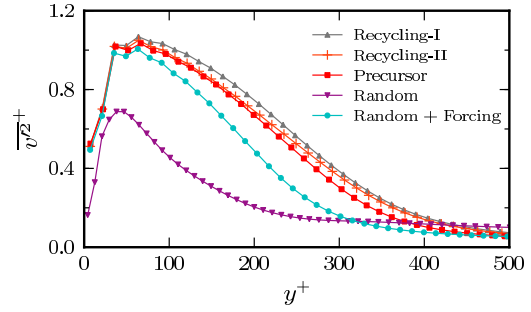


Figure 6.8: $\overline{v'^2}^+$ Reynolds stresses, at $x/\delta_0 = 16$

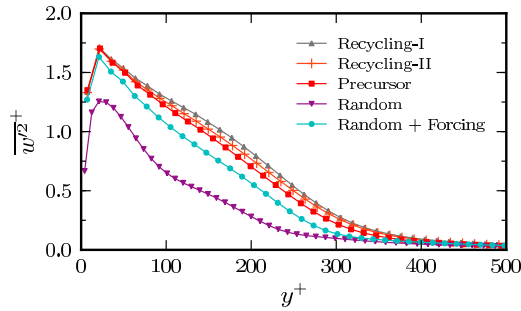


Figure 6.9: $\overline{w'^2}^+$ Reynolds stresses, at $x/\delta_0 = 16$

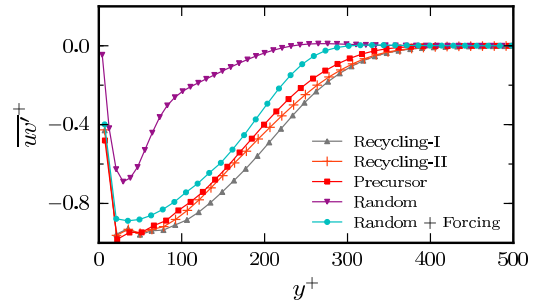
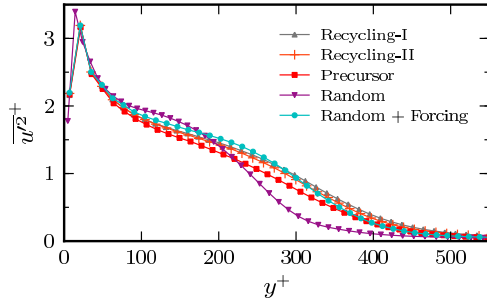
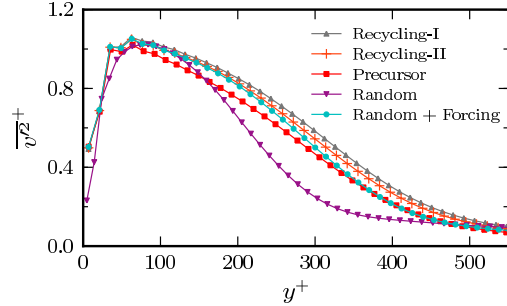
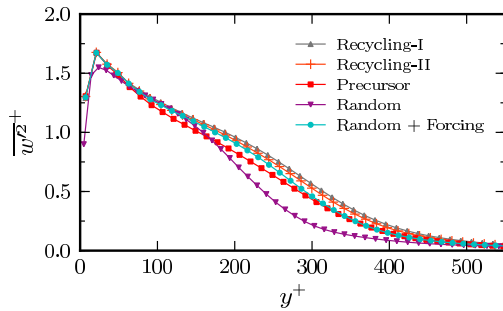
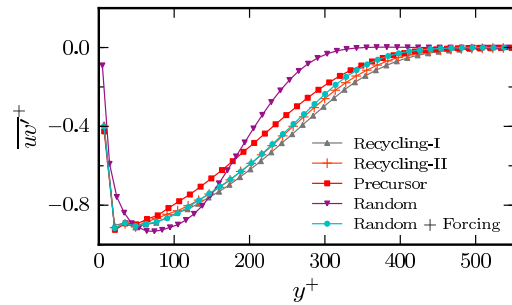


Figure 6.10: $\overline{uv'^2}^+$ Reynolds stresses, at $x/\delta_0 = 16$

The Reynolds stress plots concur with what was illustrated in the shape factor and skin-friction evolution plots, as well as the qualitative streamwise extraction planes, namely the quality of the precursor-like simulation, and the effect of the forcing planes on the random-inflow solution. Indeed, the Reynolds stress of the precursor method shows to be similar to that of the recycling type of inflows, albeit very slightly underpredicted. In contrast, the Reynolds stresses of the random inflow appear to be largely underpredicted, although showing the correct trend. However, the effect of the forcing method by Spille-Kohoff and Kaltenbach is clearly visible on the Reynolds stresses, as they are much closer to the reference solution. It is important to notice that the best Reynolds stress match by the random inflow method with forcing is obtained for the $\overline{uv'^2}^+$ stresses, which is consistent with the implementation of the forcing method, as it is based on a correction term calculated using the difference of the computed $\overline{uv'^2}^+$ with a target stress.

The Reynolds stresses of an extraction plane further downstream located at $x/\delta_0 = 32$, are shown in figures 6.11 to 6.14, to illustrate the streamwise evolutions of the different inflows.

Figure 6.11: $\overline{u'^2}^+$ Reynolds stresses, at $x/\delta_0 = 32$ Figure 6.12: $\overline{v'^2}^+$ Reynolds stresses, at $x/\delta_0 = 32$ Figure 6.13: $\overline{w'^2}^+$ Reynolds stresses, at $x/\delta_0 = 32$ Figure 6.14: $\overline{uv'^2}^+$ Reynolds stresses, at $x/\delta_0 = 32$

From those plots can be seen that the Reynolds stresses of the recycled type inflows, the precursor method and the random inflow with forcing planes are now very similar. It is also encouraging to note that the random inflow solution is converging towards the baseline solution from the inflow by Lund et al., which confirms the convergence that was suspected by the shape factor and skin friction evolution plots.

6.2.2 Practical Remarks on the Forcing Method by Spille-Kohoff and Kaltenbach (2001)

There are a few points worth mentioning when applying the forcing method by Spille-Kohoff and Kaltenbach to a flow problem.

First of all, it should be realised that the force term added to the Navier-Stokes equation does not have the correct physical units. By setting $\beta = 0$ in equation (4.21), the force term can be determined to have dimensions $\frac{m^3}{s^3}$, whereas, in incompressible flows, the force term should have dimensions $\frac{m}{s^2}$. This illustrates that the relations relating the error in Reynolds stress to the forcing term are purely empirical, and can perhaps be improved by trying to link the forcing terms to more physical quantities from the flow.

Another major deficiency of the original method by Spille-Kohoff and Kaltenbach is that

when determining the amplitude of the forcing term

$$r(y, t) = \alpha e(y, t) + \beta \int_0^t e(y, t') dt',$$

the integral multiplied by the β coefficient is supposed to act as a form of “memory” and filter, avoiding high frequency changes between time steps. However, such an approach implies that the error term $e(y, t)$ also becomes negative, to avoid an error accumulation through the integral term. In the current study, the integral term only increased over time, leading to an unbounded amplitude for the forcing term, and subsequent solution divergence. So ideally, a new type of filter should be implemented to avoid high frequency changes in the forcing terms.

Yet another disadvantage of the forcing method is that the α and β coefficients have to be adjusted by trial and error until a reasonable solution is obtained, which is unpractical. Similarly, the number of forcing planes, and their location, is also test-case dependant, and also has to be adjusted by trial and error.

Nonetheless, the current forcing method shows very promising results with a very simple implementation based on the \overline{uv}^+ Reynolds stresses, applying forcing terms in the wall-normal direction. It could probably be made more effective by including comparisons with other Reynolds stress components. A preliminary study by the current author showed that including forcing in streamwise direction, with the current determination of the forcing terms, also proved effective.

6.2.3 Comparison Conclusions

The results shown in the previous section confirm that both the recycling procedure by Lund et al. (1998) and that by Spalart et al. (2006) performed well in the context of equilibrium turbulent flows. The boundary-layer flows obtained from those two recycling methods both showed a correct shape factor and friction coefficient evolution, within 5% of DNS results.

Moreover, the forcing method by Spille-Kohoff and Kaltenbach (2001) proved to be a useful tool to improve upon the quality of random inflows. The change in shape factor and friction coefficient as a function of Reynolds number compared to the original random inflow was shown to be significant. The boundary-layer properties of the random inflow with forcing planes are acceptable, and could be improved further by tweaking the method by Spille-Kohoff and Kaltenbach. Therefore, the random inflow with forcing planes might be considered a valid inflow alternative when more challenging flow conditions render the rescaling procedure by impractical to apply.

The precursor method was found to under predict the boundary layer shape factor and over predict its skin friction coefficient, although doing so with approximately the correct rate of change. In light of the effectiveness of the forcing method by Spille-Kohoff and Kaltenbach, it might be useful to combine forcing planes with the channel flow precursor method to improve on its deficiencies. Similarly the random inflow with forcing planes, it could also be used to simulate more challenging flow conditions, albeit at the increased cost of having to run a secondary channel-flow simulation.

Conclusions and Recommendations

7.1 Conclusions

The goal of the current master thesis is to provide an objective comparison of recent inflow modeling techniques applicable to the simulation of flow control devices in turbulent, wall-bounded flows, in a coarse Large-Eddy Simulation framework. Of particular interest is the effectiveness of general techniques such as random inflow and precursor simulation relative to recycling methods, which are known to be reliable. Five types of inflow conditions were tested: the recycling and rescaling method by Lund et al., the simplified recycling method by Spalart et al., a precursor-like method using the method by Lund et al. to rescale data extracted from a channel-flow simulation, a random inflow method without forcing planes and a random inflow augmented with the forcing plane method by Spille-Kohoff and Kaltenbach.

These were applied to the simulation of the canonical zero-pressure gradient turbulent boundary layer, and compared to the highest quality existing low Reynolds-number DNS data.

The most consistent results were obtained using the recycling type of inflow by Lund et al. (1998) and by Spalart et al. (2006), which showed to have an adaptation length of $x/\delta_0 = 18$ and $x/\delta_0 = 22$ respectively. These suffered from slow convergence of the shape factor as the flow evolved downstream.

However, this work was also oriented towards the testing of inflow methods which are independent of the flow conditions within the domain, as these can also be applied to the simulation of more demanding types of flows, where no equilibrium turbulence region exists. The precursor-like method showed a very promising adaptation length of $x/\delta_0 = 18$, albeit with an underprediction of the shape factor and an overprediction of the skin friction evolution.

The random inflow method with forcing planes was also shown to be competitive, although this was poorly reflected by the long adaptation length of $x/\delta_0 = 30$, which was also due to a slow convergence of the shape factor evolution. In contrast, the skin friction adaptation was similar

to that of the recycling methods, albeit slightly shifted downwards. The random inflow has the added advantage over the precursor method to be easily usable in coupling with a RANS solver, as it can use the Reynolds stresses from the RANS turbulence model as input for the inflow.

As expected, the random inflow without forcing planes was found to be uncompetitive, as its shape factor and skin friction evolution did not approach that of DNS with the current domain size tested.

Using the recycling inflow method of Lund et al. (1998) as baseline result, it was also shown that the solution within the computational domain was subtly influenced by the top artificial boundary condition, which appeared not to be physical enough to ensure a proper wall-normal mean was achieved in the domain. This indicates that specialised treatments are also required for this artificial boundary.

7.2 Recommendations

The random inflow method combined with the forcing method by Spille-Kohoff and Kaltenbach (2001) showed very promising results when applied to the computation of a zero pressure-gradient turbulent boundary layer. However, as highlighted in section 6.2.2, the method by Spille-Kohoff and Kaltenbach suffered from a few drawbacks which should be further investigated. Similarly, a better definition of the “memory” term used in the amplitude determination should be developed, to avoid possible high frequency temporal oscillations.

Nonetheless, the promising results obtained by using only a wall-normal forcing term based on the \overline{uv}^+ stress give good hopes that further developing the method, to include a streamwise component for the forcing term and perhaps a correction term based on other components of the Reynolds stress, would yield even better results. The effect of allowing a higher frequency content in the random inflow signal should be investigated, to determine if it could improve the random inflow effectiveness by decreasing its adaptation length. This should be investigated in a follow-up study.

In light of its effect on the random inflow, the forcing method by Spille-Kohoff and Kaltenbach (2001) could also be applied to the precursor method, to investigate whether it would be effective in decreasing its adaptation length. In addition, if more research was to be done in the framework of zero pressure gradient flat-plate boundary layers, a better definition of the upper artificial boundary condition would have to be developed, to ensure the correct wall-normal mean velocity evolution is simulated.

And finally, although not mentioned in the text, the use of OpenFOAM for carrying out this research proved to be a major impediment. The modifications required to carry out this work placed the author in a position where there was limited support available from mentors of the Aerodynamics group. In addition, many behaviours observed during the current study remain unexplained, even by lead developers of OpenFOAM. It is strongly recommended that continued use of OpenFOAM within the faculty be accompanied by a significant allocation of staff and resources to its support and development, so that students are not drawn into detailed implementation problems which have little connection with the research topic at hand.

References

- Batten, P., U. Goldberg, and S. Chakravarthy (2004). Interfacing Statistical Turbulence Closures With Large-Eddy Simulation: Boundary Conditions For Large-Eddy Simulation. *AIAA Journal* 42(3), 485–492.
- Bernard, P. S. and J. M. Wallace (2002). *Turbulent Flow: Analysis, Measurement, and Prediction*. John Wiley & Sons Inc.
- Chauhan, K. A., P. A. Monkewitz, and H. M. Nagib (2009). Criteria for assessing experiments in zero pressure gradient boundary layers. *Fluid Dynamics Research* 41, 021404.
- Colonus, T. (2004). Modeling Artificial Boundary Conditions for Compressible Flow. *Annu. Rev. Fluid Mech.* 36, 315–345.
- Davidson, P. (2004). *Turbulence: an Introduction for Scientists and Engineers*. Oxford University Press.
- de Villiers, E. (2006). *The Potential of Large Eddy Simulation for the Modelling of Wall Bounded Flows*. Ph. D. thesis, Imperial College.
- DeGraaff, D. B. and J. K. Eaton (2000). Reynolds-number scaling of the flat-plate turbulent boundary layer. *Journal of Fluid Mechanics* 422(1), 319–346.
- Druault, P., J. F. Largeau, F. Coiffet, J. Delville, J. P. Bonnet, and S. Lardeau (2005). Numerical Investigations of Turbulent Inflow Condition Generation for LES. *Journal of Fluids Engineering* 127(5), 945–948.
- Ferziger, J. and M. Perić (2002). *Computational Methods For Fluid Dynamics*. Springer Berlin.
- Fureby, C., A. Gosman, G. Tabor, H. Weller, N. Sandham, and M. Wolfshtein (1997). Large Eddy Simulation of Turbulent Channel Flows. In *Symposium on Turbulent Shear Flows, 11 th, Grenoble, France*, pp. 28–13.
- Germano, M. (1986). A proposal for a redefinition of the turbulent stresses in the filtered navier–stokes equations. *Physics of Fluids* 29, 2323–2324.
- Germano, M., U. Piomelli, P. Moin, and W. H. Cabot (1991). A dynamic subgrid-scale eddy viscosity model. *Physics of fluids. A, Fluid dynamics* 3(7), 1760–1765.

- Ghosal, S., T. S. Lund, P. Moin, and K. Akselvoll (1995). A dynamic localization model for large-eddy simulation of turbulent flows. *Journal of Fluid Mechanics* 286, 229–255.
- Horiuti, K. (1985). Large Eddy Simulation of Turbulent Channel Flow by One-Equation Modeling. *J. Phys. Soc. Japan* 54(8), 2855–2865.
- Hughes, T. J., L. Mazzei, and K. E. Jansen (2000). Large Eddy Simulation and the variational multiscale method. *Computing and Visualization in Science* 3(1), 47–59.
- Keating, A., U. Piomelli, E. Balaras, and H.-J. Kaltenbach (2004). A priori and a posteriori tests of inflow conditions for large-eddy simulation. *Physics of Fluids* 16, 4696–4712.
- Kim, J., P. Moin, and R. Moser (1987). Turbulence statistics in fully developed channel flow at low Reynolds number. *Journal of Fluid Mechanics* 177, 133–166.
- Kolmogorov, A. N. (1941a). Energy Dissipation in Locally Isotropic Turbulence. *Doklady Akad. Nauk. SSSR* 32(1), 19–21.
- Kolmogorov, A. N. (1941b). The Local Structure of Turbulence in Incompressible Viscous Fluid for Very Large Reynolds Numbers. *Dokl. Akad. Nauk. SSSR* 30, 301–341.
- Lee, S., S. K. Lele, and P. Moin (1992). Simulation of spatially evolving turbulence and the applicability of Taylor’s hypothesis in compressible flow. *Physics of Fluids A: Fluid Dynamics* 4, 1521–1530.
- Lilly, D. (1967). The representation of small-scale turbulence in numerical simulation experiments. In *Proceedings of the IBM Scientific Computing Symposium on Environmental Sciences*, pp. 195.
- Lilly, D. (1992). A proposed modification of the Germano subgrid-scale closure method. *Physics of Fluids A: Fluid Dynamics* 4(3), 633–635.
- Lund, T. S., X. Wu, and K. D. Squires (1998). Generation of Turbulent Inflow Data for Spatially-Developing Boundary Layer Simulations. *Journal of Computational Physics* 140(2), 233–258.
- Marusic, I. (2001). On the role of large-scale structures in wall turbulence. *Physics of Fluids* 13, 735–743.
- Marusic, I. and W. D. C. Heuer (2007). Reynolds Number Invariance of the Structure Inclination Angle in Wall Turbulence. *Physical review letters* 99(11), 114504.
- Monkewitz, P. A., K. A. Chauhan, and H. M. Nagib (2007). Self-consistent high-reynolds-number asymptotics for zero-pressure-gradient turbulent boundary layers. *Physics of Fluids* 19, 115101.
- Moran, J. (1984). *An Introduction to Theoretical and Computational Aerodynamics*. John Wiley & Sons.
- Moser, R. D. and P. Moin (1987). The effects of curvature in wall-bounded turbulent flows. *Journal of fluid mechanics* 175, 479–510.
- Nikitin, N. (2007). Spatial periodicity of spatially evolving turbulent flow caused by inflow boundary condition. *Physics of Fluids* 19(9), 091703–091703.
- Pamiès, M., P. Weiss, E. Garnier, S. Deck, and P. Sagaut (2009). Generation of synthetic turbulent inflow data for large eddy simulation of spatially evolving wall-bounded flows. *Physics of Fluids* 21, 045103.
- Patel, V. C. and M. R. Head (1969). Some observations on skin friction and velocity profiles in fully developed pipe and channel flows. *Journal of Fluid Mechanics* 38(01), 181–201.

-
- Piomelli, U. and J. Liu (1995). Large-eddy simulation of rotating channel flows using a localized dynamic model. *Physics of Fluids* 7, 839–848.
- Pope, S. B. (2000). *Turbulent Flows*. Cambridge University Press.
- Sagaut, P., S. Deck, and M. Terracol (2006). *Multiscale and Multiresolution Approaches in Turbulence*. Imperial College Press.
- Sagaut, P., E. Garnier, E. Tromeur, L. Larchevêque, and E. Labourasse (2004). Turbulent Inflow Conditions for Large-Eddy Simulation of Compressible Wall-Bounded Flows. *AIAA Journal* 42(3), 469–477.
- Sagaut, P. and C. Méneveau (2006). *Large Eddy Simulation for Incompressible Flows: An Introduction*. Springer Verlag.
- Schlatter, P. and R. Örlü (2010). Assessment of direct numerical simulation data of turbulent boundary layers. *Journal of Fluid Mechanics* 659(1), 116–126.
- Schlüter, J., H. Pitsch, and P. Moin (2004). Large Eddy Simulation Inflow Conditions for Coupling with Reynolds-Averaged Flow Solvers. *AIAA journal* 42(3), 478–484.
- Simens, M. P., J. Jiménez, S. Hoyas, and Y. Mizuno (2009). A high-resolution code for turbulent boundary layers. *Journal of Computational Physics* 228(11), 4218–4231.
- Smits, A., N. Matheson, and P. Joubert (1983). Low-reynolds-number turbulent boundary layers in zero and favorable pressure gradients. *Journal of ship research* 27(3), 147–157.
- Spalart, P., M. Strelets, and A. Travin (2006). Direct numerical simulation of large-eddy-break-up devices in a boundary layer. *International Journal of Heat and Fluid Flow* 27(5), 902–910.
- Spalart, P. R. (1988). Direct simulation of a turbulent boundary layer up to $Re_\theta = 1410$. *Journal of fluid mechanics* 187, 61–98.
- Spalart, P. R. and A. Leonard (1985). Direct numerical simulation of equilibrium turbulent boundary layers. In *IN: Symposium on Turbulent Shear Flows, 5th, Ithaca, NY, August 7-9, 1985, Proceedings (A86-30201 13-34)*. University Park, PA, Pennsylvania State University, 1985, p. 9.35-9.40.
- Spalding, D. (1961). A single formula for the law of the wall. *Journal of Applied Mechanics* 28, 455–457.
- Spille-Kohoff, A. and H.-J. Kaltenbach (2001). Generation of turbulent inflow data with a prescribed shear-stress profile.
- Spyropoulos, E. T. and G. A. Blaisdell (1998). Large-Eddy Simulation of a Spatially Evolving Supersonic Turbulent Boundary-Layer Flow. *AIAA journal* 36(11), 1983–1990.
- Wei, T., R. Schmidt, and P. McMurtry (2005). Comment on the Clauser chart method for determining the friction velocity. *Experiments in Fluids* 38(5), 695–699.
- White, F. M. (2006). *Viscous Fluid Flow, Third Edition*. McGraw-Hill, New York.

OpenFOAM Settings

8.1 Domain Used

A domain size of $60 \delta_0 \times 4 \delta_0 \times 8 \delta_0$ was used, in streamwise, wall-normal and spanwise direction respectively, as illustrated in figure 8.1. The domain was meshed with a uniform grid, with $320 \times 64 \times 64$ cells, resulting in very low aspect ratio cells, of relative size $3 \times 1 \times 2$.

8.2 Numerical Setup

A free stream velocity of $U_\infty = 20 \text{ m/s}$ was chosen, together with a viscosity of $\nu = 0.001937 \text{ m}^2/\text{s}$ and an inflow boundary layer thickness $\delta_0 = 0.5 \text{ m}$. The recycling plane of the recycled methods was placed at $48 \delta_0$ from the inflow.

The incompressible, unsteady, turbulent PISO solver was used, with 4 PISO corrector steps, and with a time step of 0.0008 seconds yielding a maximum Courant number of 0.3. The homogeneousDynSmagorinsky turbulent model was used, corresponding to the dynamic Smagorinsky model with domain averaging of C_s values, together with the cubeRootVol filter.

A central discretization scheme (Gauss linear) was chosen for the computation of the gradient and divergence terms, except for the turbulent quantities which were discretized with a limited central discretization scheme (Gauss linearLimited 1). The time marching was done using a second-order implicit backward Euler scheme (backward in OpenFOAM). The Geometric Algebraic MultiGrid (GAMG) linear solver with Gauss-Sidel smoothing was used to solve the pressure equation, to a tolerance of 10^{-8} , and with a relative tolerance (relTol) between iterations of 0. The Preconditioned Bi-Conjugate Gradient (PBiCG) linear solver with Diagonal Incomplete LU (DILU) preconditioner was used for the other equations, to a tolerance of 10^{-7} , and once more with a relative tolerance (relTol) between iterations of 0.

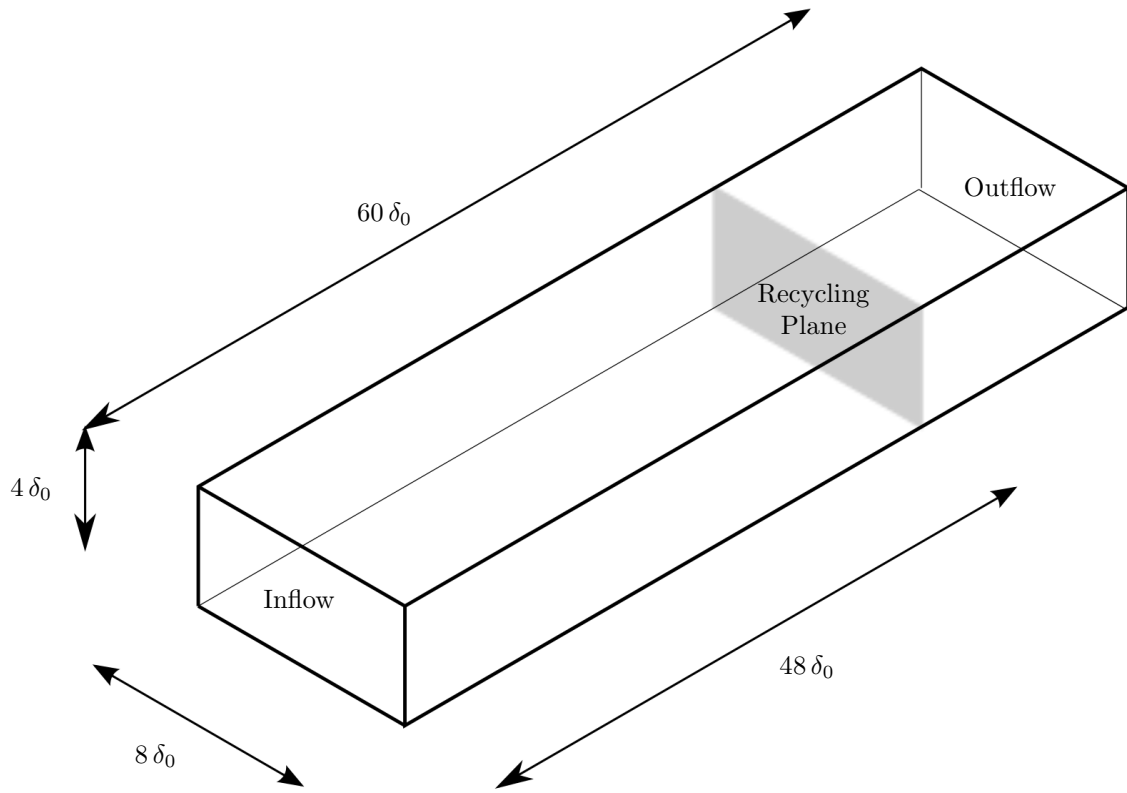


Figure 8.1: Domain used for inflow comparison

Table 8.1: Flow settings

	Settings
U_∞	20 [m/s]
ν	0.001937 [m ² /s]
δ_0	0.5 [m]

Table 8.2: Solver Settings

	Settings
Turbulent Solver	Piso
Corrector Steps	4
nonOrthogonalCorrectors	0
Time Step	0.0008 [s]
Max Courant	0.3

8.3 Validation

To validate the different SGS models implemented in OpenFOAM, a channel flow simulation was run on a $6 \times 2 \times 4$ domain, with a 64^3 grid resolution. A short summary of the results will be

Table 8.3: SGS Model Settings

	Settings
SGS model	homogeneousDynSmagorinsky
Δ	cubeRootVol
filter	simple

Table 8.4: Linear Solvers Settings

	Settings
variable solver	p, pFinal GAMG
smoother	GaussSidel
tolerance	10^{-8}
relTol	0
variable solver	U, k, B PBiCG
preconditionner	DILU
tolerance	10^{-7}
relTol	0

made here after. The plots of the mean velocity, $\overline{u'^2}^+$, $\overline{v'^2}^+$ and $\overline{w'^2}^+$ Reynolds stress can be found in figures 8.2 to 8.5.

As can be seen from figures 8.2 to 8.5, the domain averaged Smagorinsky (homogeneous-DynSmagorinsky) model performs best, followed by the local dynamic one equation model (loc-DynOneEq) and the domain averaged one equation model (homogeneousDynOneEq). Strangely, the local dynamic model seems to overpredict the mean velocity.

The effect of grid stretching was also investigated with the channel flow, using a uniform 100^3 grid, and a stretched 100^3 grid, where the smallest cell next to the wall was 10 times smaller than the largest cell in the middle. The results can be seen here-after. The $\overline{v'^2}^+$ and $\overline{w'^2}^+$ Reynolds stresses were not found to display an other trend than the $\overline{u'^2}^+$, so were left out.

As can be seen from figures 8.6 and 8.7, grid stretching tends to slightly overpredict the mean velocity, while not significantly increasing the Reynolds stress accuracy.

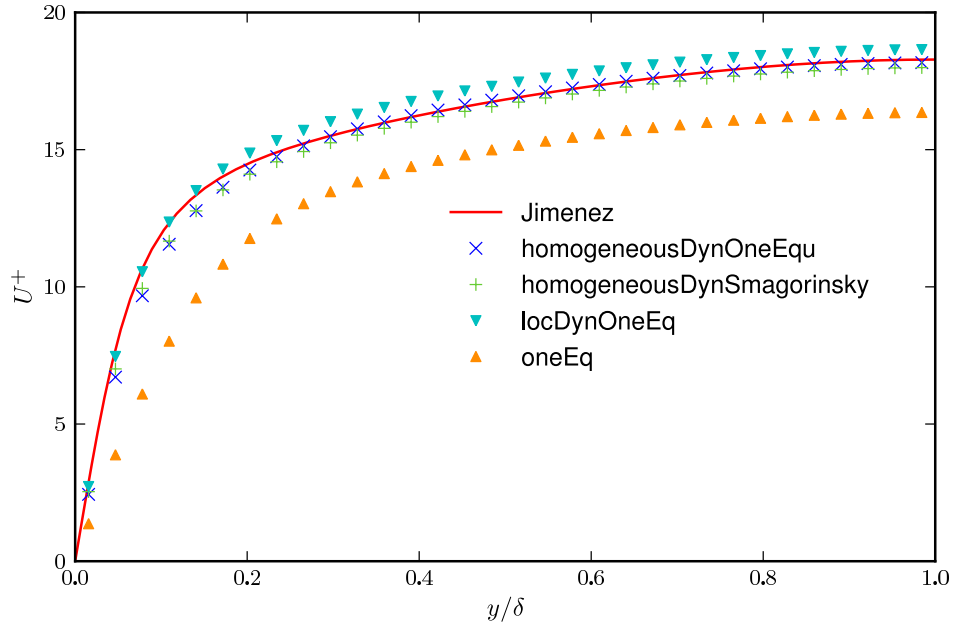


Figure 8.2: Channel-flow mean capture, for various SGS models

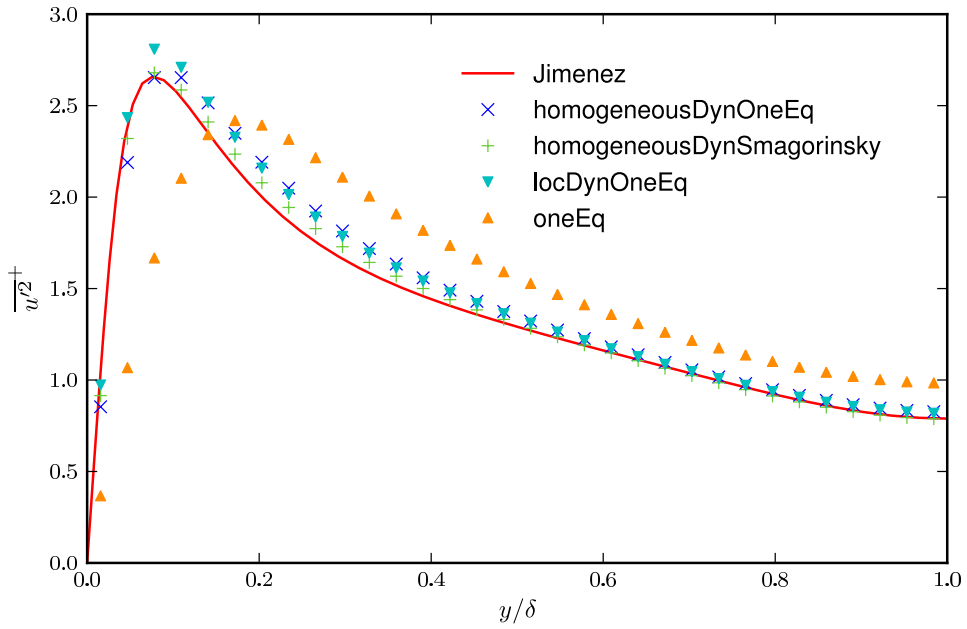
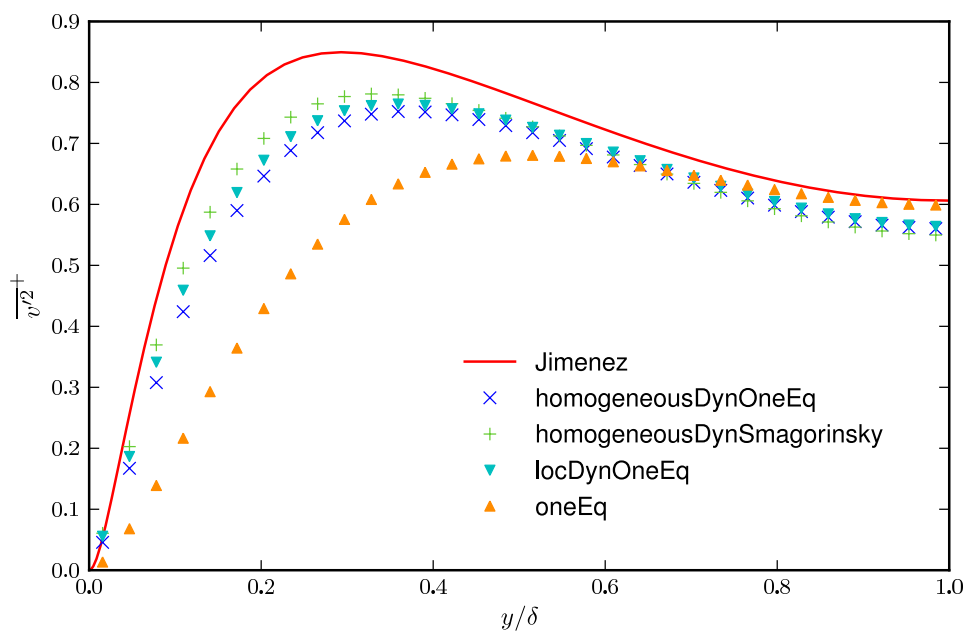
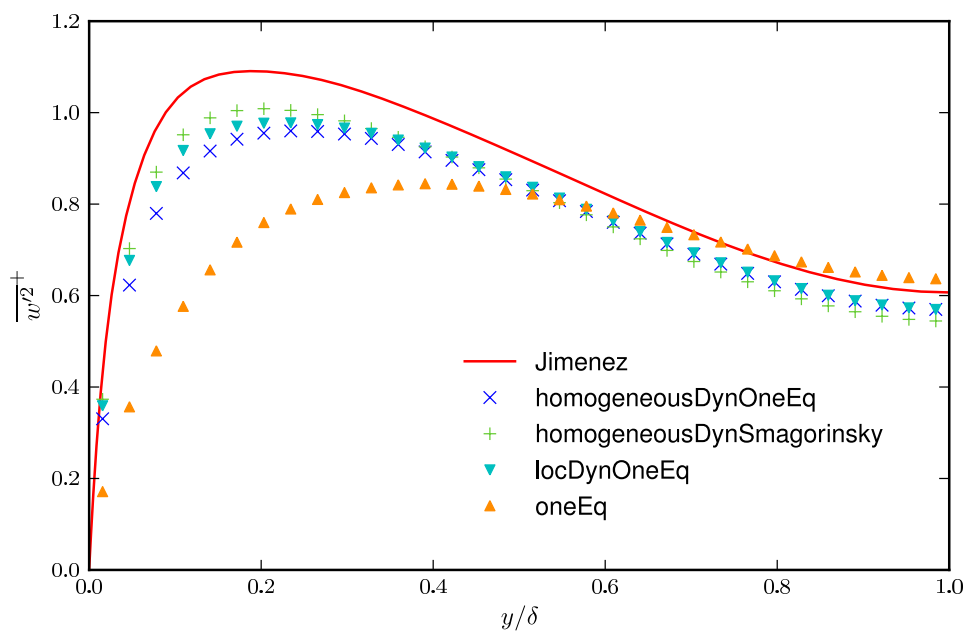


Figure 8.3: Channel-flow $\overline{u'^2}^+$ capture, for various SGS models

Figure 8.4: Channel-flow $\overline{v'^2}^+$ capture, for various SGS modelsFigure 8.5: Channel-flow $\overline{w'^2}^+$ capture, for various SGS models

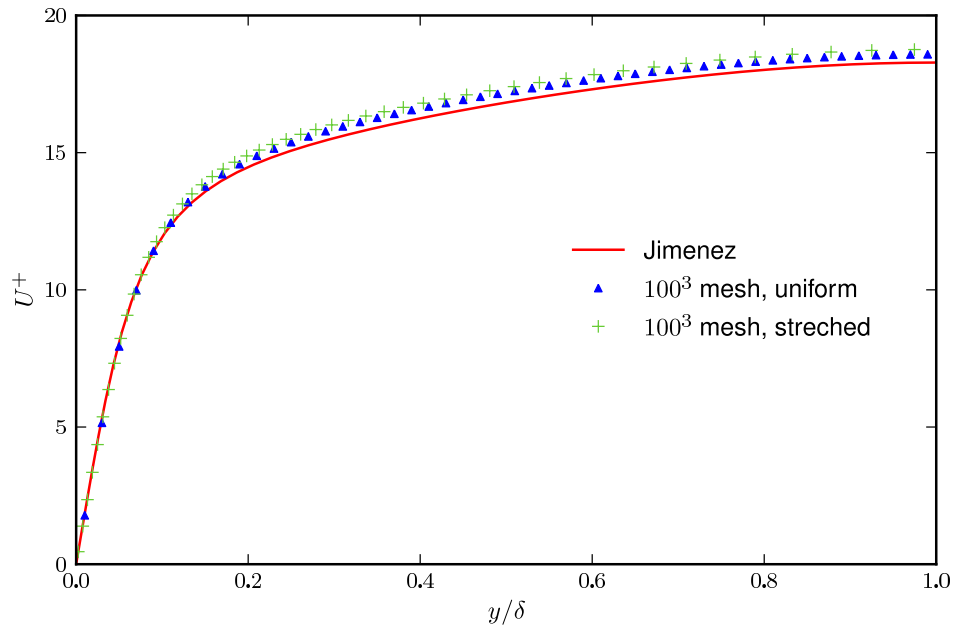


Figure 8.6: Channel-flow mean capture, uniform and stretched 100^3 grid

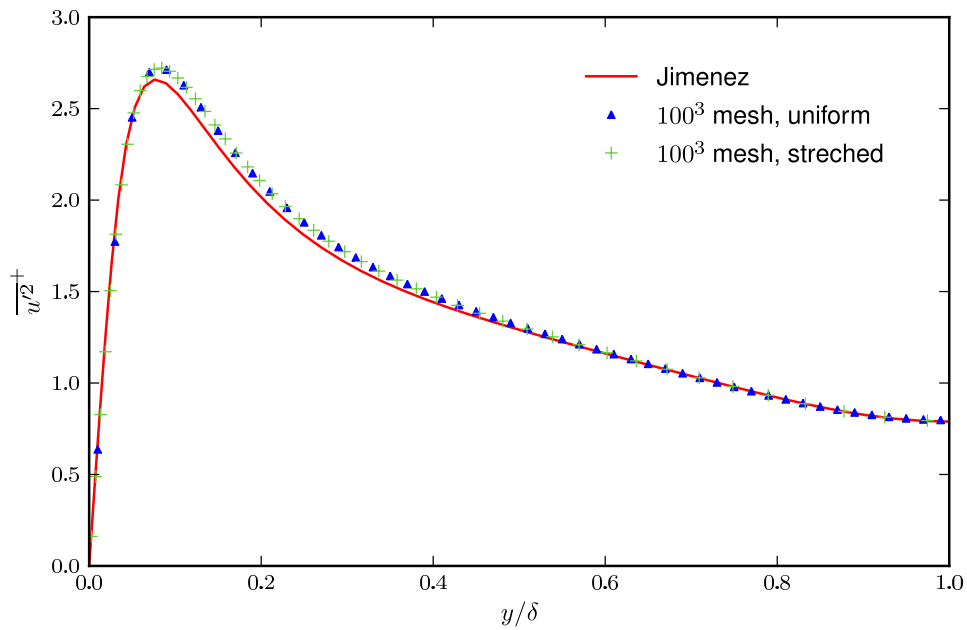


Figure 8.7: Channel-flow $\overline{u'^2}^+$ capture, uniform and stretched 100^3 grid